TU Delft

Master Thesis

Ultra High Sensitivity Microwave Kinetic Inductance Detectors

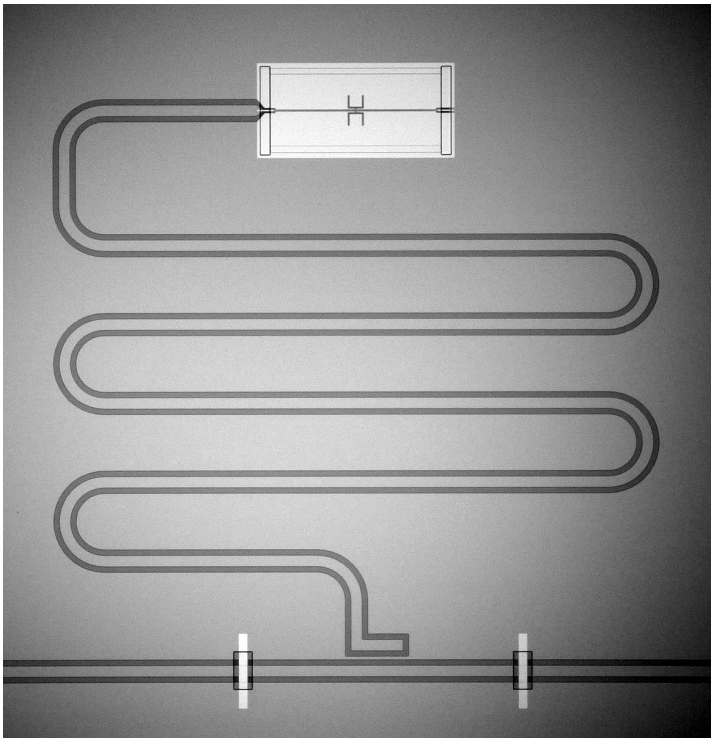

Author:
Stefan Verheul

July 8, 2019

Ultra High Sensitivity Microwave Kinetic Inductance Detectors

by

Stefan Verheul

in partial fulfillment of the requirements for the degree of
Master of Science
at Delft University of Technology

Student number:	4037855	
Project duration:	March 12, 2018 – August 9, 2019	
Thesis committee:	Dr. ir. J. J. A. Baselmans,	Delft University of Technology, SRON Netherlands Institute for Space Research, Utrecht, *supervisor*
	Dr. A. Endo,	Delft University of Technology, 2nd *examiner*
	Dr. G. A. Steele,	Delft University of Technology, 3rd *examiner*

An electronic version of this thesis is available at `http://repository.tudelft.nl/`.

TU Delft

SRON
Netherlands Institute for Space Research

Abstract

Microwave Kinetic Inductance Detectors (MKIDs) are extremely sensitive radiation detectors based on superconducting resonators that can be combined in large arrays on a single readout line within a limited frequency bandwidth. This makes MKIDs ideal detectors for the ultimate far-infrared observatory: a future space-based 4 K cooled telescope with its performance solely limited by the low universe background radiation. However, to reach these detector requirements, state-of-the-art MKIDs still need a factor 10 improvement in device sensitivity. In this work, the MKID sensitivity is improved by reducing the aluminium volume that absorbs pair-breaking radiation into quasiparticle excitations, while making sure all radiation is still absorbed. Furthermore, a key requirement is sufficient reduction of excess noise as to keep the device intrinsically limited by thermally driven random fluctuations in the number of quasiparticles in absence of radiation, or Generation-Recombination (G-R) noise. To this end, a model is developed that describes the noise contributions as function of device geometry, readout power, material properties and radiation power. Subsequently, a realistic MKID design is presented and tested that reduces excess noise and maximises the sensitivity, expressed as Noise Equivalent Power (NEP). At high temperatures $T > 270$ mK, good overall agreement is found between the measured noise spectra and the model. At low temperature $T = 120$ mK, the measurement results give an optical $NEP = 2.4 \times 10^{-19}\,\mathrm{W}/\sqrt{\mathrm{Hz}}$, similar to current state-of-the-art MKIDs. The NEP is not as low as expected due to short quasiparticle lifetimes, an unexpected decrease in the G-R noise level and a very high excess noise attributed to Two-Level Systems (TLS) noise that starts to dominate the already low G-R noise spectrum at low temperatures. Possibly, the quick quasiparticle lifetime saturation and noise level drop are caused by a strong readout power effect, as the readout power is known to create excess quasiparticles and to cause a strongly non-thermal electron energy distribution in the aluminium strip of the MKID. However, the exact microscopic details of these effects are unknown and not studied in this project. A straightforward way to improve device performance and study the readout power effect in more detail is a reduction of the high TLS noise levels, which is possibly fabrication related. This would allow an unobstructed view of the G-R noise spectrum at low temperatures, thereby allowing both a study of the readout power effect on the quasiparticle system, and ultimately achieving the factor 10 improvement in NEP needed reach the detector requirements for the ultimate space-based far-infrared observatory.

Contents

Chapter 1

Introduction

Far-infrared astronomy concerns the observation of the sky visible within the bandwidth of far-infrared (FIR), or sub-mm, radiation, loosely defined here as corresponding to frequencies between $0.3 - 10$ THz, or wavelenghts between 1 mm and 30 µm. The past two decades, technological advancements and an increasing number of FIR observatories have made the previously unexplored sub-millimeter universe accessible [1]. This range of wavelengths makes it possible to unveil astronomical phenomena which are invisible in all other parts of the electromagnetic spectrum. Namely, the observation of planet and star formations mostly hidden within cold dusty clouds, many spectral characteristics of molecular and atomic gases including water and organic molecules and the observation of distant, highly red-shifted galaxies [2].

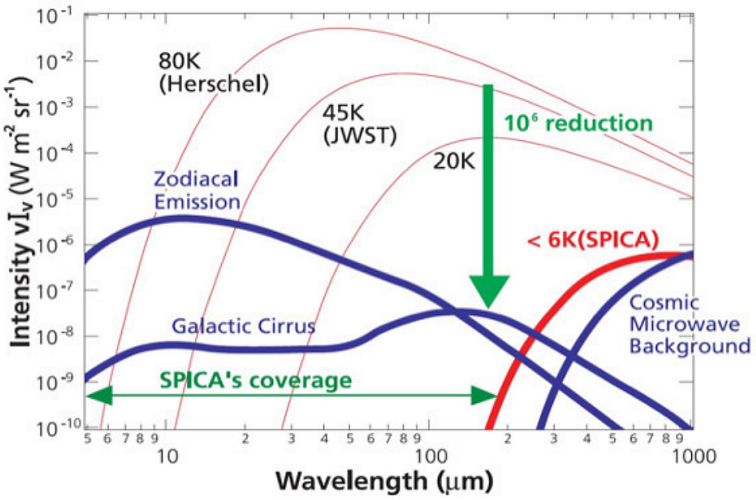

Figure 1.1 – Radiant power per unit area per steradian versus wavelength. The astrophysical background contributions (zodiacal emission, galactic cirrus and CMB) are compared with several telescope backgrounds at different temperatures. The total astrophysical background around 200 µm is six orders of magnitude lower than the Herschel telescope at 80 K. Picture from Farrah *et al* [1].

Since water vapor blocks most of the FIR radiation, all ground-based observatories are located at high and dry sites. A good example is the ALMA interferometer, the largest FIR observatory on the planet, consisting of 66 telescopes combined into a single receiver [3]. It is located in the Atacama desert at 5200m altitude and observes only at frequency windows not fully blocked by the atmosphere. Space-based observatories like Herschel circumvent the problem of an opaque atmosphere, thereby in principle accessing the full FIR spectrum. However, as Herschel was operated at 80 K, the thermal radiation from the telescope itself still dominates the the flux falling on the detectors, as is shown in figure 1.1.

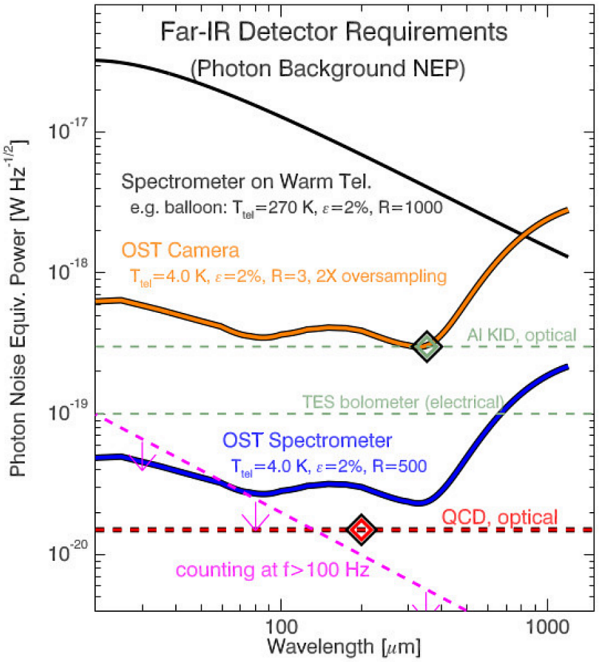

Figure 1.2 – Sensitivity requirements for far-infrared background limited detector at different resolutions along with current sensitivities of different detector technologies. The NEP for the Aluminium Kinetic Inductance Detector (Al KID) is still a factor 10 higher than the OST Spectrometer requirements. Picture from Farrah *et al* [1].

By cooling a space-based telescope to temperatures of a few Kelvin, thermal emission in the FIR band can be dramatically reduced to a point where the performance is only limited by astrophysical backgrounds. This is very clear from the red line in 1.1, which shows the flux on the detector for the 6 K telescope of the SPICA mission, which is being considered now. This also sets the sensitivity requirements for a background limited detector, because we need a more sensitive detector when the background power falling on it is reduced [4]. Since the power on the detector scales with the intensity divided by the spectral resolution, $R = \nu/\Delta\nu$, it can be seen from Fig. 1.1 that the power reduces strongly with increasing resolution and a colder telescope. The detector sensitivity requirement for the Origins Space Telescope (OST), a future space-based 4 K cooled far-infrared observatory, is shown in figure 1.2. The red line shows the NEP for a low resolution camera, the bottom blue line for a $R = 500$ spectrometer instrument. The latter corresponds to a $NEP = 2 \times 10^{-20}\,\mathrm{W}/\sqrt{\mathrm{Hz}}$. Since the state-of-the-art KIDs have a $NEP = 3 \times 10^{-19}\,\mathrm{W}/\sqrt{\mathrm{Hz}}$ [5], a factor 10 improvement in device sensitivity is still needed to meet the ultimate FIR detector requirements.

1.1 Kinetic Inductance Detectors

MKIDs, an acronym for Microwave Kinetic Inductance Detectors, are extremely sensitive radiation detectors, and introduced by Day *et al.* in 2003 [6]. MKIDs exploit the fact that the energy gap of a superconductor is of the order of $\sim$ meV, which corresponds to a frequency of ~ 100 GHz. Additionally, electronic noise is suppressed exponentially at low temperatures of $T < T_\mathrm{c}$ K, with T_c the critical temperature. The combination of these facts makes a superconductor ideal to detect radiation at FIR frequencies. MKIDs are in essence very high Q resonators operating at GHz frequencies. Many MKIDs can be designed to occupy a limited frequency bandwidth, of the order of 1000 MKIDs GHz^{-1} are possible [5]. This allows the construction of large arrays, based upon a readout system that combines many MKID resonators on a single readout line and a single piece of readout electronics. So, MKIDs combine a high sensitivity and the capability to make large detector arrays. This makes them ideal for future and present far-infrared instruments for astronomy.

The operation principle of a KID is schematically depicted in Fig. 1.3. Incident photons with sufficient

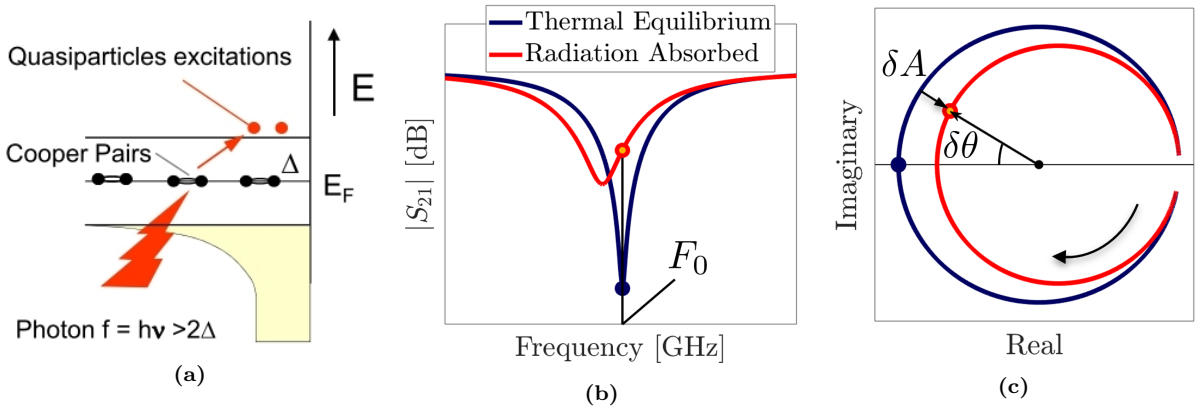

Figure 1.3 – Illustration of the working principle of a KID. **(a)** Energy diagram of a superconductor in which a photon with energy $h\nu > 2\Delta$ breaks a Cooper pair into two quasiparticle excitations. Picture from [7]. **(b)** Shifted and broadened microwave transmission $|S_{21}|$ of a resonator as a function of frequency upon radiation absorption (red line) compared to its transmission in thermal equilibrium (blue line). **(c)** The same data as in **b**, plotted in the complex plane for the real and imaginary parts of S_{21}, where the blue arrow indicates increasing frequency. By tracking either dA or dθ using F_0 as readout signal, the radiation absorption can be measured.

energy $h\nu > 2\Delta$, where 2Δ is the superconductor energy gap, are able to break Cooper pairs into quasiparticle excitations. Cooper pairs, bound together by an attractive phonon-mediated electron interaction, have a pair binding energy of $2\Delta \approx 3.53 k_B T_c$. An aluminium superconductor with a critical temperature T_c =1.2 K therefore has an energy gap of 0.18 meV. Since $E = h\nu$, photons with a frequency in excess of 90 GHz are able to break Cooper pairs. Upon radiation absorption, the number of quasiparticles increases and thereby affects the kinetic inductance and the surface impedance of the resonator. Consequently, this lowers the resonant frequency and causes a reduction in the intrinsic quality factor of the resonator. Hence, absorbed radiation results in a downward frequency shift and a broadened, shallower of the resonance dip due to the lower quality factor.

In order to actually read out the changes in resonant characteristics, the superconductor is coupled to transmission line which feeds the resonator a single frequency, F_0, the unperturbed resonant frequency of the KID in thermal equilibrium, indicated by the blue dot in figure 1.3b. In an experiment one measures the complex transmission of this signal at F_0 through the transmission line. Upon radiation detection, the absolute value of the transmitted signal $|S_{21}|$ at F_0 is increased, as indicated by the red dot. When plotted in the complex plane, it is evident that radiation detection results in a response in both amplitude (dA) and phase (dθ). This is displayed in figure 1.3c, which shows a frequency sweep of the complex transmission, which traces out a circle, hereafter referred to as the resonance circle.

The resonance circle is used as a frame of reference to read-out the MKIDs resulting in an amplitude response (dA) and a phase response (dθ).

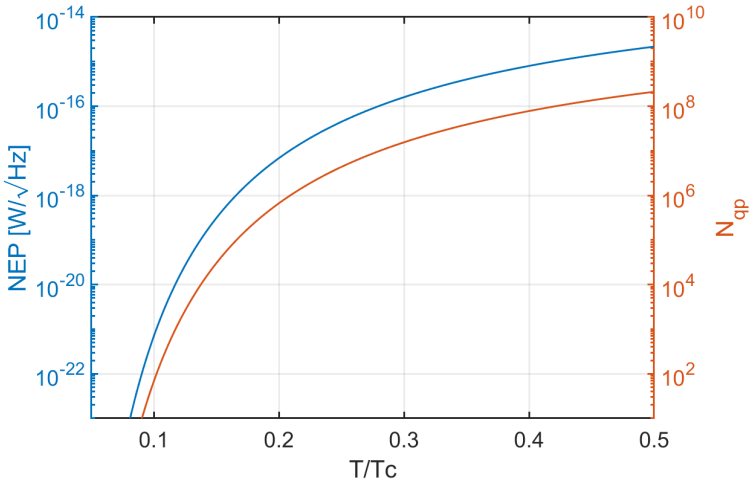

Figure 1.4 – NEP_{GR} and N_{qp}, the quasiparticle number, as a function of temperature. Aluminium strip with a critical temperature T_{c} =1.29 K, thickness $d = 50$ nm, linewidth $S = 2$ µm and length $l = 8$ mm.

1.2 Intrinsic Limit: Generation-Recombination Noise

MKIDs are designed to measure changes in quasiparticle density induced by pair-breaking radiation. However, not all quasiparticles are created by absorption of photons. In thermal equilibrium, that is, without any incident radiation, the number of quasiparticles fluctuates around an average value. The origin of these fluctuations is a thermally driven random process of quasiparticle generation and recombination into Cooper pairs, or G-R noise for short. Therefore, thermal quasiparticle number fluctuations are an intrinsic noise source of a KID.
This imposes a lower limit on the device sensitivity, which is expressed as the *noise-equivalent power* (NEP) and is defined as the power that gives a signal-to-noise ratio (SNR) of 1 in an integration time of 0.5 sec. The NEP due to generation-recombination, intrinsic to the detector, is given by

$$NEP_{\mathrm{GR}} = \frac{2\Delta}{\eta_{\mathrm{pb}}}\sqrt{\frac{N_{\mathrm{qp}}}{\tau_{\mathrm{qp}}}}\,. \tag{1.2.1}$$

Here Δ is the superconductor energy gap, η_{pb} the pair-breaking efficiency factor, τ_{qp} is the quasiparticle recombination time and N_{qp} the number of quasiparticles in thermal equilibrium.

Since it also holds that $N_{\mathrm{qp}} \propto 1/\tau_{\mathrm{qp}}$, $\mathrm{NEP}_{\mathrm{GR}} \propto N_{\mathrm{qp}}$. Figure 1.4 shows the temperature dependence of NEP_{GR} and N_{qp} for a superconducting aluminium strip with $V = 800\,\mu\mathrm{m}^3$. It shows that the NEP is expected to exponentially decrease with decreasing temperature and be lower than $10^{-20}\,\mathrm{W}/\sqrt{\mathrm{Hz}}$ at $T < T_{\mathrm{c}}/10$. This is a consequence of the fact that in a superconductor the quasiparticle density decreases exponentially with temperature.

Therefore, reducing N_{qp}, by either lowering the temperature or reducing the device volume are two obvious methods to improve the device performance.

1.2.1 Measuring Intrinsic Limits

The response of an MKID to changes in quasiparticle number can be observed using amplitude and phase readout, as indicated in figure 1.3c. This also allows measuring G-R noise: Fluctuations in quasiparticle number can be measured by measuring the noise of the MKID phase and amplitude signal at thermal equilibrium. The fluctuations are identified by their spectral characteristics, for which one uses the noise power spectral density (PSD). The PSD gives the noise power per unit of bandwidth as a function of frequency. An example is given in figure 1.5, which shows data reproduced from Visser *et al*[8] where the MKID amplitude noise PSD is determined by quasiparticle fluctuations. The PSD of the phase noise due to

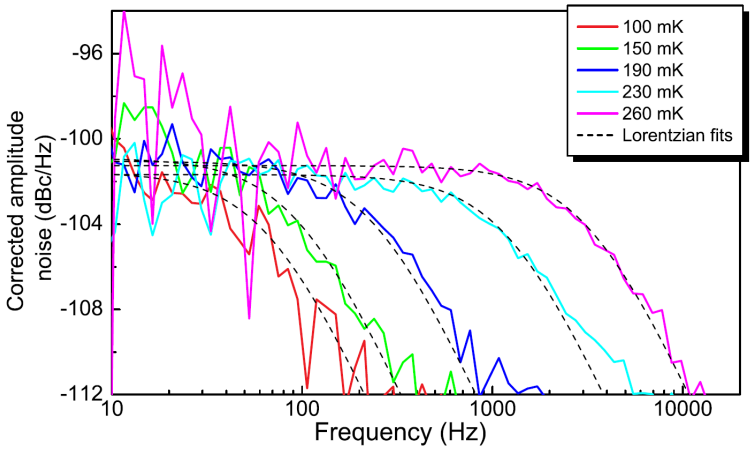

Figure 1.5 – PSD signature of the resonator amplitude fluctuations as a function of frequency, for 5 different chip temperatures. The roll-off shifts to higher frequencies for increasing temperatures while the noise level is temperature independent. Picture from [8].

quasiparticle fluctuations is given by

$$S_\theta(\omega) = \frac{4N_{\rm qp}\tau_{\rm qp}}{1+(2\pi f\tau_{\rm qp})^2}\left(\frac{{\rm d}\theta}{{\rm d}N_{\rm qp}}\right)^2, \tag{1.2.2}$$

where f is the modulation frequency and ${\rm d}\theta/{\rm d}N_{\rm qp}$ the phase response to a change in quasiparticle number. The first term, $4N_{\rm qp}\tau_{\rm qp}$, gives the noise level in number fluctuations and the second term converts number fluctuations to the MKID phase noise. The expression for amplitude noise is similar. The PSD of a G-R noise limited device shows two characteristics:

1. The noise level is constant, *independent* of temperature. Since $N_{\rm qp} \sim 1/\tau_{\rm qp}$, the product $N_{\rm qp}\tau_{\rm qp}$ in eq. 1.2.2 remains constant under a change of temperature.

2. The spectrum shows a roll-off at a frequency reciprocal to the recombination time. The roll-off frequency, $\omega = 1/\tau_{\rm qp}$, depends on temperature since $\tau_{\rm qp}$ decreases for increasing temperatures. This can be seen in figure 1.5, in which the PSD shows a roll-off at higher frequencies as the chip temperature is increased.

Hence, the shape of the spectrum contains information about the physical processes in the system. The recombination time $\tau_{\rm qp}$ can be derived from a fit to the roll-off. Subsequently, given the response $({\rm d}\theta/{\rm d}N_{\rm qp})$ and the recombination time, the quasiparticle number can be inferred from the constant noise level. Furthermore, the $NEP_{\rm GR}$ can be calculated using Eq. 1.2.1, using Δ obtained from a measurement of the $T_{\rm c}$ and a calculation of $\eta_{\rm pb}$.

1.2.2 The Readout Power Creates Excess Quasiparticles

Although the readout frequencies ($4-8$ GHz) are well below the gap energy (~ 90 GHz for aluminium), the readout power has been shown to produce excess quasiparticles nonetheless [9]. In figure 1.6, the number of quasiparticles is shown as a function of the device temperature. The saturation of $N_{\rm qp}$ around 160 mK, and thereby the deviation from the theoretical thermal quasiparticle number, indicates the presence of excess quasiparticles. The number of excess quasiparticles is experimentally proven to be dependent on the readout power and attributed to a process of multiple photon absorption [10]. Increasing the readout power ($P_{\rm read}$) causes an apparent increase in quasiparticle density and a subsequent decrease in lifetime as shown in figure 1.7. Clearly, reducing $P_{\rm read}$ increases $\tau_{\rm qp}$ and decreases $n_{\rm qp}$. Therefore, referring back to Eq. 1.2.1, a lower NEP could be obtained by decreasing the readout power. However, excess noise sources make it impossible to reduce $P_{\rm read}$ indefinitely. While the G-R noise signal remains unchanged by $P_{\rm read}$, external noise sources

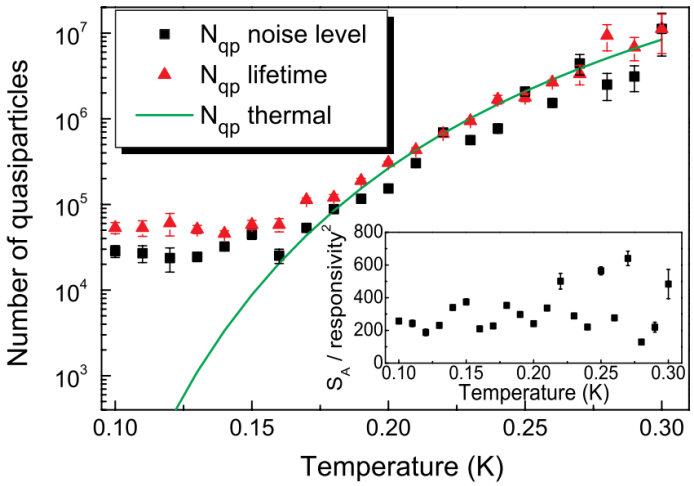

Figure 1.6 – Number of quasiparticles as a function of temperature as determined by the measured quasiparticle lifetimes and the noise level, together with the theoretical exponential decrease when lowering the temperature. At around 160 mK, the quasiparticle number saturates.

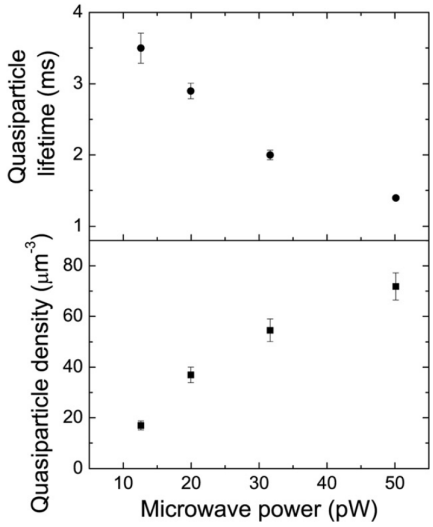

Figure 1.7 – Weighted averages of 100-150 mK measurement values of the quasiparticle density and and lifetime as a function of readout power. Increasing microwave power comes with a rise in the quasiparticle density and a lifetime reduction [9]. At the lowest microwave power, with $\tau_{\mathrm{qp}} = 3.5\,\mathrm{ms}$, Visser *et al.* obtained an $NEP = 2 \times 10^{-19}\,\mathrm{W}\sqrt{\mathrm{Hz}}$.

do increase. Figure 1.8 shows the noise PSD of existing measurement data for several readout powers with the black curve, corresponding to the highest readout power, showing a G-R noise limited spectrum as indicated by the flat noise level and the spectrum roll-off. For lower readout powers, the total noise spectrum becomes dominated by several noise sources apart from G-R noise, which will be treated in detail in Chapter 2.

Hence, the readout power is constrained from both sides. Reducing P_{read} leads to a low NEP, however, excess noise imposes a limit in the reduction of the readout power and thereby the NEP.

1.3 Route towards a low NEP detector

So, what are possible routes towards low NEP detectors? Two possibilities are considered in this section, with a motivation of their feasibility. First and foremost, the active volume could be reduced. As previously stated in section 1.2, the NEP_{GR} is dependent on the absolute number of quasiparticles N_{qp}, not the density. Hence, if it is assumed that the quasiparticle density and recombination time stay the same, a volume reduction means that $N_{\mathrm{qp}} = n_{\mathrm{qp}}V$ is reduced, and thereby the NEP. A significantly lower NEP would thus be achievable if the active volume of the resonator is reduced. In doing so, however, the radiation

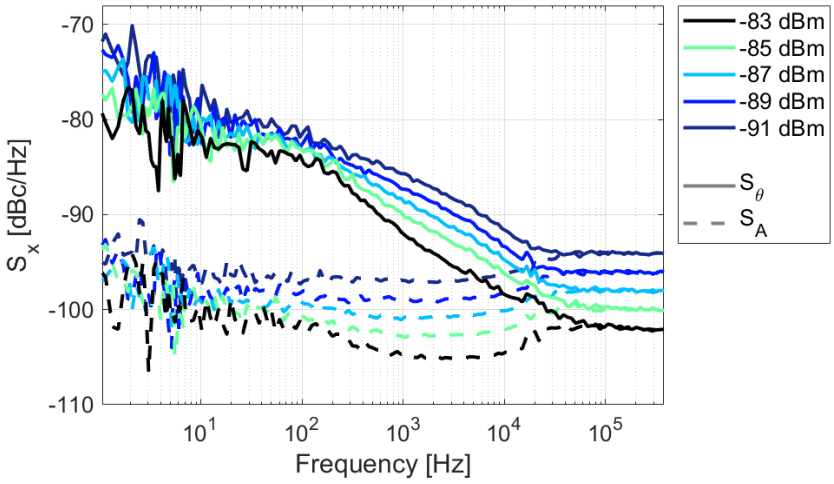

Figure 1.8 – Example of the noise PSD of existing measurement data for various readout powers, shown for both amplitude (*dashed lines*) and phase (*solid lines*) noise. At the highest readout power, $P_{\mathrm{read}} = -83$ dBm, G-R noise is visible by the spectrum roll-off. For lower readout powers, excess noise starts to dominate the spectrum.

should still be completely absorbed in the volume, which is the subject of Chapter 3.
Second, the readout power, P_{read} could be reduced as this has been shown to reduce the number of excess quasiparticles, increase their lifetime and thereby lowering the NEP. However, excess noise hinders the reduction of P_{read} (Fig. 1.8).

In conclusion, the goal of this project is to achieve low Noise Equivalent Power of an MKID detector. That is, to reach the sensitivity requirements for a future space-based 4 K observatory. This will be achieved by reducing the active volume of the resonator, at the same time ensuring that all radiation is absorbed.

Chapter 2

Theory

2.1 Superconductivity: Quasiparticles and Cooper Pairs

Superconductors are normal metals at high temperatures, but transit to a superconducting state below a certain critical temperature T_c, typically of a few Kelvin. When cooled down below T_c, the electrical resistivity of a superconductor shows an abrupt drop to zero which means that the electric current can flow indefinitely. As a consequence, the superconductor acts as a perfect diamagnet, excluding magnetic fields by screening currents located in a thin but finite layer at the surface. As the fields penetrate the material, they decay exponentially over a characteristic lengthscale denoted by the penetration depth, λ. In contrast to superconductors, normal metals show no transition to a state of zero dc resistivity. Instead, as the temperature is lowered, they converge to a finite residual resistivity, the value of which results from impurities and structural defects in the material [11]. Most relevant for this report is the appearance of an energy gap around the Fermi energy in the superconducting state, an explanation of which is provided by BCS theory [12], describing the microscopic details of superconductivity.

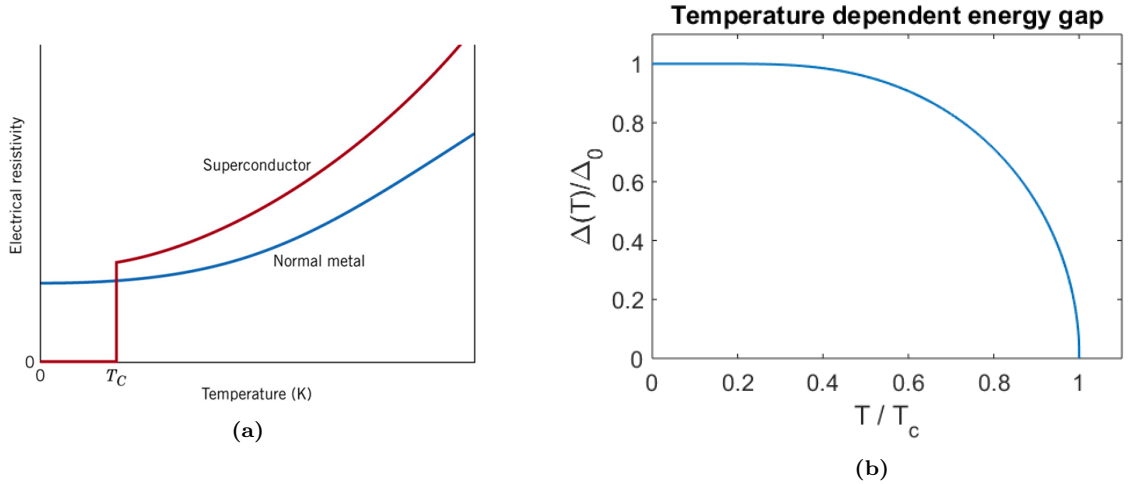

Figure 2.1 – **(a)** Electrical resistivity, ρ, of the superconductor drops to zero at $T = T_c$ whereas a normal conductor shows a finite resistivity up to $T = 0\,\mathrm{K}$. Electrical resistivity is the inverse of conductivity, $\rho = \sigma^{-1}$. **(b)** Temperature dependent energy gap $\Delta(T)$ of a superconductor up to T_c, in units normalized to the energy gap at $T = 0$, Δ_0, and the critical temperature T_c. As $T \ll T_c$, the energy gap $\Delta(T)$ approaches Δ_0. A derivation of $\Delta(T)$ can be found in for example [13].

A qualitative description of the microscopic origin of superconductivity is as follows: At $T < T_c$, pairs of electrons can form a bound state, so called Cooper pairs. The attractive interaction between two electrons required to from a Cooper pair cannot originate from electrons alone since the (screened) Coulomb interaction

is always repulsive. It results from interactions with lattice vibrations, or phonons. As an electron moves through the lattice, it leaves a region of enhanced positive charge behind due to the heavier and therefore slower moving ions constituting the lattice. In turn, the enhanced ion density attracts another electron, thereby mediating a net attractive electron-electron interaction. If this electron attraction exceeds the screened Coulomb repulsion, conduction electrons with opposite spin and momenta will pair up, forming so called Cooper pairs [14]. A direct result is the superconductor energy gap of 2Δ around the Fermi energy in the single particle density of states, which can be interpreted as the binding energy of the Cooper pairs. BCS theory provides a mathematical description for the collective Cooper pair formation into a new, superconducting ground state. Furthermore, the energy gap at $T = 0$ is related to the critical temperature T_c as $2\Delta_0 \simeq 3.53\, k_B T_c$ [12].

The detection mechanism of MKIDs relies on radiation absorption in a superconducting thin film. For photon energies $E > 2\Delta$, Cooper pairs can be broken into quasiparticle excitations. This process is only possible for frequencies exceeding $\omega = 2\Delta/\hbar$ For an aluminium superconductor with $T_c = 1.2\,\mathrm{K}$ this corresponds to photons in excess of 90 GHz.

2.1.1 Quasiparticle Density and Recombination Time

In a superconductor in thermal equilibrium, the number of quasiparticles fluctuates around an average value. This number fluctuation is called generation-recombination noise, in short G-R noise. The density of thermally excited quasiparticles in a superconductor is proportional to the product of the superconductor density of states, $N_s(\epsilon) = \frac{\epsilon}{\sqrt{\epsilon^2-\Delta^2}}$, and the Fermi-Dirac distribution, $f(\epsilon) = 1/[\exp(\epsilon/k_B T) + 1]$[15]. Most relevant is that the quasiparticle density n_{qp} is exponentially low for $k_B T \ll \Delta$. The quasiparticle density is given by

$$n_{qp} = 4N_0 \int_{\Delta}^{\infty} N_s(\epsilon) f(\epsilon) \mathrm{d}\epsilon\,, \tag{2.1.1}$$

$$\simeq 2N_0 \sqrt{2\pi k_B T \Delta}\, \exp\left(\frac{-\Delta}{k_B T}\right), \tag{2.1.2}$$

in which ϵ is the energy relative to the Fermi energy E_F, k_B the Boltzmann constant, Δ the energy gap, T the temperature and N_0 is the single spin density of electron states at the Fermi level. For aluminium, $N_0 = 1.72 \times 10^{10}\,\mu\mathrm{m}^{-3}\mathrm{eV}^{-1}$ [16]. Quasiparticle number fluctuations are random and can be described by Poisson statistics. Hence, the standard deviation is $\mathrm{SD}(n_{qp}) \propto \sqrt{n_{qp}}$. Therefore, to minimise fluctuations in the number of thermally excited quasiparticles, MKIDs are operated at low temperatures ($T \ll T_c$) where n_{qp} is exponentially small.

The recombination time indicates how long quasiparticle excitations exist on average before they recombine with another quasiparticle to form a Cooper pair, emitting a phonon in the process. This recombination time is inversely proportional to n_{qp} and accordingly exponentially increased when lowering the temperature [17]. The single particle recombination time, for $T \ll T_c$, in thermal equilibrium is

$$\tau_{qp} = \frac{\tau_0}{\sqrt{\pi}} \left(\frac{k_B T_c}{2\Delta}\right)^{5/2} \sqrt{\frac{T_c}{T}} \exp\left(\frac{\Delta}{k_B T}\right) \tag{2.1.3}$$

$$= \frac{\tau_0}{n_{qp}} \frac{N_0 (k_B T_c)^3}{2\Delta^2}\,, \qquad \text{(combined with Eq. 2.2)} \tag{2.1.4}$$

in which τ_0 is material dependent electron-phonon interaction time. Note that the observed recombination time, which is for 2 particles, is twice shorter, i.e. $\tau_{qp}/2$.

For the electron-phonon interaction time, Kaplan *et al.* obtained a theoretical result of 438 ns [17] and Visser *et al.* experimentally obtained 458 ns [18], where the latter should be multiplied by 2 to compare with the theory.

2.2 Complex Conductivity

Although superconductors show no DC resistance below their critical temperature, there is a non-zero surface impedance due to alternating (AC) currents.

At microwave frequencies, the surface impedance is dominated by an inductive contribution due to the inertia of the Cooper pairs which oscillate to the electric field, the kinetic inductance. Since MKIDs are superconducting microwave resonators, a description of its electrodynamic response is crucial. This section discusses the complex conductivity of a superconductor at low temperatures $T < T_c$, its frequency dependency and its response to a change in quasiparticle density[1]. This forms the basis of the response in the experimentally attainable resonator observables $\mathrm{d}A$, $\mathrm{d}\theta$, which are discussed further on in section 2.3.1.

For the superconductors described in this report, the electrodynamic response is given by the Mattis-Bardeen theory. It describes the response of the superconductor to a high frequency electric field, which depends on the Cooper pair and quasiparticle density.

In general, the classical Ohm's law is not valid as the current density $\mathbf{J}(\mathbf{r})$ is related to the varying electric field $\mathbf{E}(\mathbf{r}')$ in the surrounding region. The size of this region is set by an effective coherence length, ξ_{eff}, a characteristic lengthscale similar to the electron mean free path ℓ_e in normal conductors [20]. However, for two limiting cases, the so-called dirty limit and the extreme anomalous limit (as further explained below), the relation $\mathbf{J} = \sigma\mathbf{E}$ still holds and the conductivity σ can then be concisely expressed in a real and complex part,

$$\sigma = \sigma_1 - i\sigma_2 \,. \tag{2.2.1}$$

The real part of the complex conductivity (σ_1) is due to quasiparticle excitations in the superconductor and is dissipative. Furthermore, for low frequencies and temperatures ($k_B T, \hbar\omega \ll 2\Delta$) this term is small since n_{qp} is exponentially low in this regime. The imaginary part of the conductivity (σ_2) is due to the inertia of the Cooper pairs, resulting in a kinetic inductance.

2.2.1 Characteristic Lengthscales

Whether or not one of the limits holds depends on the relative size of three characteristic lengthscales of a superconducting material, the electron mean free path ℓ_e, the coherence length $\xi_0 = \hbar v_F/\pi\Delta_0$, with v_F the Fermi velocity, and penetration depth λ. The extreme anomalous limit holds when the coherence length is much larger than the London penetration depth $\lambda_L = \sqrt{\frac{m}{\mu_0 n e^2}}$ with m the electron mass, n the conduction electron density and e the electron charge [16]. In the case of bulk aluminium, with $v_F = 2.03 \times 10^6\,\mathrm{m/s}$, the coherence length $\xi_0 = 2200\,\mathrm{nm}$ and the London penetration depth $\lambda_L = 12\,\mathrm{nm}$. Thus $\xi_0 \gg \lambda_L$, which implies the extreme anomalous limit.

However, for the MKIDs described in this report, a thin-film aluminium layer is used, for which the dirty limit holds. The dirty limit occurs when both the penetration depth and coherence length are much larger than the mean free path ($\xi_0, \lambda \gg \ell_e$). To justify this, an overview is given of the lengthscales and their typical values. Namely, a thin-film aluminium superconductor of thickness $d = 40\,\mathrm{nm}$ with a normal state resistivity $\rho_n = 1.52\,\mu\Omega\,\mathrm{cm}$ operated at low temperatures $T \ll T_c$, $T = 120\,\mathrm{mK}$.

ℓ_e: The electron mean free path is short for a high metal impurity and related to resistivity via $1/\rho_n = \frac{2}{3} N_0 e^2 v_F \ell_e$ with $N_0 = 1.72 \times 10^{10}\,\mu\mathrm{m}^{-3}\mathrm{eV}^{-1}$ the aluminium single spin density of states at the Fermi level and v_F the Fermi velocity as before [20]. This gives $\ell_e \simeq 18\,\mathrm{nm}$.

ξ_0: The coherence length can be interpreted as the size of a Cooper pair and Δ_0 is the gap energy at zero temperature [12, 21]. The effective coherence length mentioned earlier is defined as $\xi_{\text{eff}} = 1/\xi_0 + 1/\ell_e$ and since $\xi_0 \gg \ell_e$, this becomes $\xi_{\text{eff}} \simeq \ell_e$.

λ: The penetration depth for the case $\xi_{\text{eff}} \ll \lambda$ is given by $\lambda = \lambda_L\sqrt{1 + \xi_0/\ell_e}$ [22] in which λ_L is the London penetration depth. Furthermore, for perpendicular magnetic fields on a thin-film superconductor, the penetration depth is modified from the bulk value and given by the Pearl length [23] $\lambda_P \approx \lambda^2/d \simeq 476\,\mathrm{nm}$, thus $\ell_e \ll \lambda_P$. Hence, $\ell_e \ll \xi_0$ and $\ell_e \ll \lambda_P$ and the dirty limit condition is satisfied.

[1] Equivalent expressions in terms of the surface impedance Z_s can be found in [19]

The Mattis-Bardeen expressions for the complex conductivity, valid in both the dirty limit and the extreme anomalous limit are given by the integrals [12]

$$\frac{\sigma_1}{\sigma_\mathrm{n}} = \frac{2}{\hbar\omega}\int_{\Delta}^{\infty} \mathrm{d}\epsilon\,[f(\epsilon) - f(\epsilon+\hbar\omega)]\frac{(\epsilon^2+\Delta^2+\hbar\omega\epsilon)}{\sqrt{\epsilon^2-\Delta^2}\,\sqrt{(\epsilon+\hbar\omega)^2-\Delta^2}} + \frac{1}{\hbar\omega}\int_{\min(\Delta-\hbar\omega,-\Delta)}^{-\Delta} \mathrm{d}\epsilon\,[1-2f(\epsilon+\hbar\omega)]\frac{(\epsilon^2+\Delta^2+\hbar\omega\epsilon)}{\sqrt{\epsilon^2-\Delta^2}\,\sqrt{(\epsilon+\hbar\omega)^2-\Delta^2}}\,, \tag{2.2.2}$$

$$\frac{\sigma_2}{\sigma_\mathrm{n}} = \frac{1}{\hbar\omega}\int_{\max(\Delta-\hbar\omega),-\Delta}^{\Delta} \mathrm{d}\epsilon\,[1-2f(\epsilon+\hbar\omega)]\frac{(\epsilon^2+\Delta^2+\hbar\omega\epsilon)}{\sqrt{\Delta^2-\epsilon^2}\,\sqrt{(\epsilon+\hbar\omega)^2-\Delta^2}}\,, \tag{2.2.3}$$

with $\Delta = \Delta(T)$ the temperature dependent energy gap, which equals Δ_0 for low temperatures (see Fig. 2.1b). The first integral in σ_1 describes the electrodynamic response of quasiparticles scattered from energies ϵ to $\epsilon+\hbar\omega$, i.e. the acceleration of the quasiparticles themselves. The second term in σ_1 only contributes when $\hbar\omega > 2\Delta$ because it accounts for pair-breaking photons and describes Cooper pairs broken into quasiparticles. The integral in σ_2 accounts for the available Cooper pairs where the energy is absorbed in the Cooper pair system. Hence, the lower limit is $-\Delta$ when $\hbar\omega > 2\Delta$. Figure 2.2 shows a calculation of σ_1 and σ_2 as a

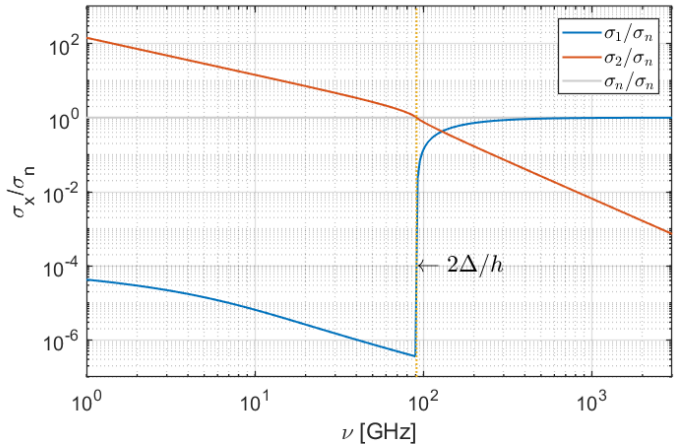

Figure 2.2 – Complex conductivity normalised to the normal conductivity σ_n as function of frequency $\nu = \omega/2\pi$ in GHz with a critical temperature corresponding to that of aluminium, $T_\mathrm{c} = 1.24$, at a temperature $T = T_\mathrm{c}/8$. The real part, σ_1, increases drastically when passing the gap frequency at $\nu_\mathrm{gap} = 2\Delta/h = 90\,\mathrm{GHz}$ as indicated by the dotted yellow line. At high frequencies, $\nu \gg \nu_\mathrm{gap}$, the conductivity approaches the normal state conductivity σ_n, indicated by the gray line.

function of frequency for an aluminium superconductor with $T_\mathrm{c} = 1.24\,\mathrm{K}$ and $T = T_\mathrm{c}/8$. This illustrates the working principle of an MKID. Radiation at frequencies well above the gap frequency $\omega_\mathrm{rad} \gg \omega_\mathrm{gap}$ is absorbed by breaking Cooper pairs into quasiparticles. Because at these frequencies, σ approaches the normal state conductivity (σ_n). At frequencies $\omega \ll \omega_\mathrm{gap}$, $\sigma_1 \ll \sigma_2$ i.e. the material is virtually loss-free, where the exact values of σ_1 and σ_2 depend on the amount of radiation absorbed, the temperature and the frequency.

For $T \ll T_\mathrm{c}$ and microwave frequencies below the gap frequency $\omega \ll 2\Delta/\hbar$, the real and complex parts of the conductivity can be expressed in the following simpler form:

$$\frac{\sigma_1}{\sigma_\mathrm{n}} = \frac{4\Delta}{\hbar\omega}\exp\left(\frac{-\Delta}{k_\mathrm{B}T}\right)\sinh\left(\frac{\hbar\omega}{2k_\mathrm{B}T}\right)K_0\left(\frac{\hbar\omega}{2k_\mathrm{B}T}\right), \tag{2.2.4}$$

$$\frac{\sigma_2}{\sigma_\mathrm{n}} = \frac{\pi\Delta}{\hbar\omega}\left[1 - 2\exp\left(\frac{-\Delta}{k_\mathrm{B}T}\right)\exp\left(\frac{-\hbar\omega}{2k_\mathrm{B}T}\right)I_0\left(\frac{\hbar\omega}{2k_\mathrm{B}T}\right)\right], \tag{2.2.5}$$

where σ_n is the normal state conductivity, Δ the superconductor energy gap at $T = 0\,\mathrm{K}$ and $I_0(x)$ and $K_0(x)$ are modified Bessel functions of the first and second kind. In Fig. 2.3, the conductivity is plotted together

with the full expressions, indicating that Eqs. 2.2.4, 2.2.5 agree well over the frequency range where the MKID response to changes in quasiparticle density is evaluated.

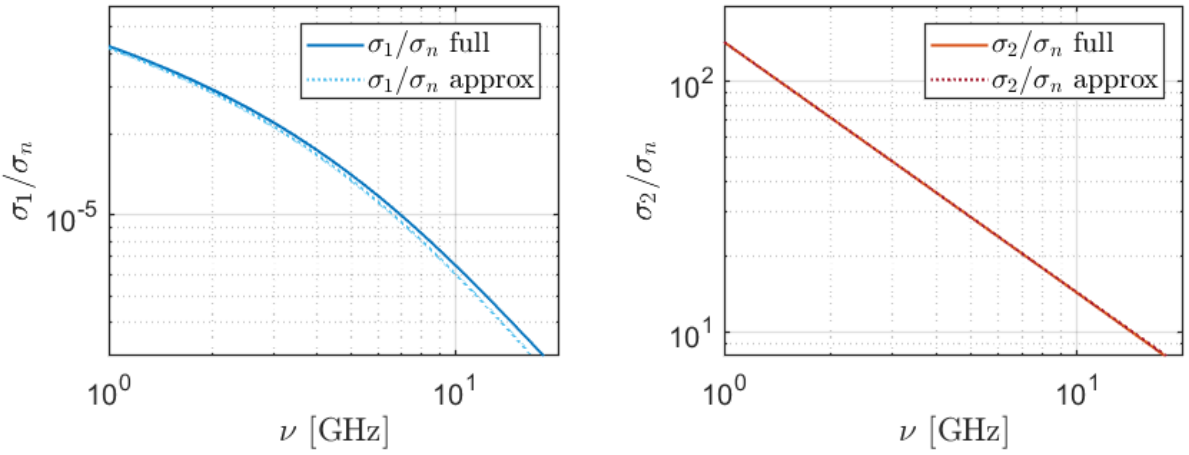

(a) **(b)**

Figure 2.3 – Comparison of the complex conductivity approximations (Eq. 2.2.4, 2.2.5) with the full integrals (Eqs. 2.2.2, 2.2.3) over the MKID resonance frequency range 1–10 GHz, with $\hbar\omega \ll 2\Delta$, $T = T_c/8$ and $\nu = \omega/2\pi$ as in Fig.2.2.

2.2.2 Conductivity Response to Quasiparticle Density Change

The change in complex conductivity due to a change in quasiparticle density can be obtained by combining the expressions for the complex conductivity (Eqs. 2.2.4, 2.2.5), with the expression for quasiparticle density (Eq. 2.1.2). For $T \ll T_c$ and $\omega \ll 2\Delta/\hbar$, the conductivity response to a change in quasiparticle density is

$$\begin{aligned} \frac{\mathrm{d}\sigma_1}{\mathrm{d}n_{qp}} &= \sigma_n \frac{1}{N_0\hbar\omega}\sqrt{\frac{2\Delta_0}{\pi k_B T}}\sinh\left(\frac{\hbar\omega}{2k_B T}\right)K_0\left(\frac{\hbar\omega}{2k_B T}\right), \\ \frac{\mathrm{d}\sigma_2}{\mathrm{d}n_{qp}} &= \sigma_n \frac{-\pi}{2N_0\hbar\omega}\left[1 + 2\sqrt{\frac{2\Delta_0}{\pi k_B T}}\exp\left(\frac{-\hbar\omega}{2k_B T}\right)I_0\left(\frac{\hbar\omega}{2k_B T}\right)\right]. \end{aligned} \tag{2.2.6}$$

To measure these changes in σ_1 and σ_2, the superconducting material is made part of a resonant circuit. Since $\sigma_1 \ll \sigma_2$ at low T and $\omega < \omega_{gap}$, a superconducting resonator can have a very high quality factor, enabling a powerful tool to measure very small changes in the complex conductivity. For this we need a model of the superconducting resonator, as to express the resonator behaviour change in quasiparticle density.

2.3 Superconducting Coplanar Waveguide Resonators

Before describing the response of an MKID to a changes in quasiparticle density, a detailed description of the superconducting resonator is needed. Therefore, this section provides model equations for a superconducting Coplanar Waveguide (CPW) resonator, which is the basic structure of an MKID.

A CPW is a commonly used waveguide geometry [16] that consists of a single metal layer on top of a substrate and is therefore easy to fabricate. The central line of width S is separated from the surrounding groundplanes by a distance W on either side, as shown in Fig. 2.4. A quarterwave resonator ($\lambda/4$) can be constructed from a CPW by combining an open end on one side and a shorted end on the other, thereby invoking a ($\lambda/4$) resonance condition. Consequently, the current in the resonator peaks at the shorted end while the voltage peaks at the open end. The open end of the resonator is capacitively coupled to the readout

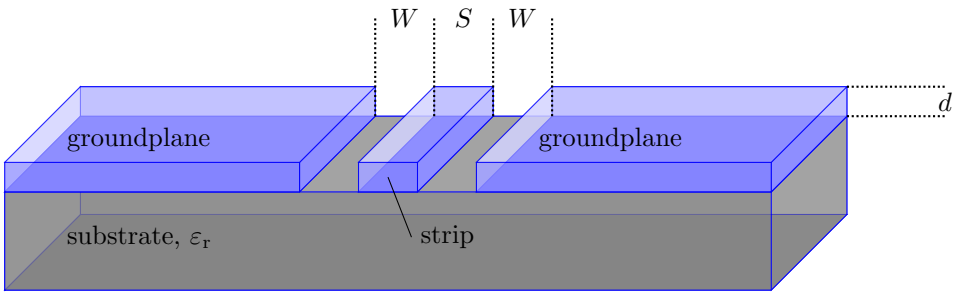

Figure 2.4 – Cross section of the CPW geometry on top of a substrate with relative permittivity ε_r. The groundplane is separated a distance W from the central strip of width S. The groundplane and stripline have a thickness d

line, which feeds the microwave signal. The resonance frequency is determined by the resonator length l_{res}, inductance L_l and capacitance C_l per unit length and is given by

$$F_0 = \frac{1}{4l_{res}\sqrt{L_l C_l}}, \tag{2.3.1}$$

in which the factor 4 appears because the wavelength of a quarterwave resonator is four times its length, $\lambda = 4l_{res}$. The geometric contributions of L_l and C_l for a CPW are not related to superconductivity but

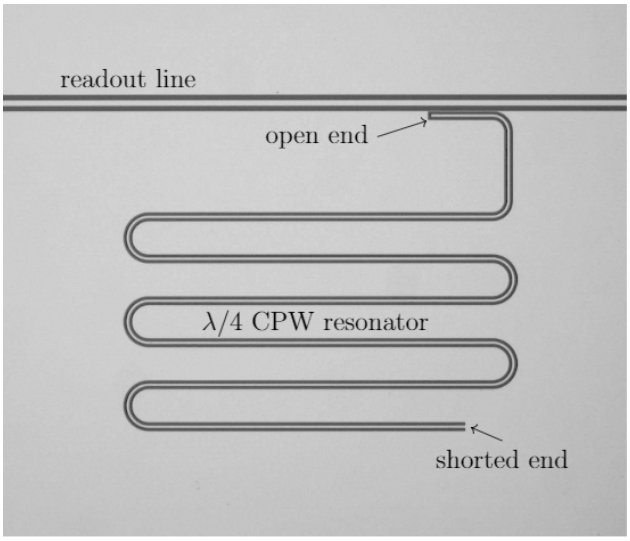

Figure 2.5 – Illustration of a quarterwave CPW resonator. The open end is capacitively coupled to the readout line while the other end is shorted to the groundplane, to impose a $\lambda/4$ resonance condition. The CPW resonator is meandered due to its length, typically 4-6 mm for a few GHz.

dependent on the CPW geometry and can be found in for instance Pozar [24]. For a CPW with line width S and slot width W, the capacitance per unit length is [25]

$$C_l = 4\varepsilon_0\varepsilon_{eff}\frac{K(k)}{K(k')}, \tag{2.3.2}$$

with k and k' defined as

$$k = \frac{S}{S+2W} \quad \text{and} \quad k'^2 = 1 - k^2$$

and K the complete elliptic integral of the first kind, ε_0 the vacuum permittivity and ε_{eff} the effective dielectric constant for the CPW geometry. Since the electric field is situated half in vacuum and half in the substrate, the effective dielectric constant is taken to be approximately

$$\varepsilon_{eff} \simeq \frac{(1+\varepsilon_{r,subs})}{2}. \tag{2.3.3}$$

with $\varepsilon_{\mathrm{r,subs}}$ the relative permittivity of the substrate. The inductance also has a contribution arising from the CPW geometry:

$$L_{\mathrm{g,l}} = \frac{\mu_0}{4}\frac{K(k')}{K(k)}\,, \tag{2.3.4}$$

in which μ_0 is the vacuum permeability and K, k and k' remain the same. Importantly, for a superconductor, the kinetic inductance contributes an extra term, $L_{\mathrm{k,l}}$, to the total inductance: $L_{\mathrm{l}} = L_{\mathrm{g,l}} + L_{\mathrm{k,l}}$. The kinetic inductance is obtained from complex conductivity by rewriting the expressions for the surface impedance. For a superconducting film in the dirty limit, the surface impedance is [22],

$$Z_{\mathrm{s}} = \sqrt{\frac{i\mu_0\omega}{\sigma_1 - i\sigma_2}}\coth\Big(\frac{d}{\lambda}\sqrt{1 + i\frac{\sigma_1}{\sigma_2}}\Big)\,, \tag{2.3.5}$$

with penetration depth λ and microwave frequency ω. In terms of sheet resistance R_{s} [$\Omega/\square$] and sheet kinetic inductance L_{s} [H/$\square$].

$$Z_{\mathrm{s}} = R_{\mathrm{s}} + i\omega L_{\mathrm{s}}\,, \tag{2.3.6}$$

The sheet kinetic inductance at $hF, k_{\mathrm{B}}T \ll 2\Delta$ can be well approximated by [26]

$$L_{\mathrm{s}} \simeq \frac{\hbar R_{\mathrm{s}}}{\pi\Delta} \tag{2.3.7}$$

Now, the kinetic inductance *per unit length* is obtained from the sheet value through a factor g depending on the geometry of the device, $L_{\mathrm{k,l}} = gL_{\mathrm{s}}$. The geometric contributions of the central line and ground plane are [25]

$$g_{\mathrm{c}} = \frac{1}{4S(1-k^2)K^2(k)}\Big[\pi + \ln\Big(\frac{4\pi S}{d_{\mathrm{c}}}\Big) - k\ln\Big(\frac{1+k}{1-k}\Big)\Big] \tag{2.3.8}$$

$$g_{\mathrm{gp}} = \frac{k}{4S(1-k^2)K^2(k)}\Big[\pi + \ln\Big(\frac{4\pi(S+2W)}{d_{\mathrm{gp}}}\Big) - \frac{1}{k}\ln\Big(\frac{1+k}{1-k}\Big)\Big] \tag{2.3.9}$$

with central line and groundplane layer thickness $d_{\mathrm{c}}, d_{\mathrm{gp}}$, respectively. The geometry factors are valid for a thin-film CPW with $d < S/20$ and $k < 0.8$. Wrapped together the total inductance per unit length for a superconducting CPW with equal layer thickness for the groundplane and central line is

$$L_{\mathrm{l}} = L_{\mathrm{g,l}} + L_{\mathrm{k,l}} = L_{\mathrm{g,l}} + (g_{\mathrm{c}} + g_{\mathrm{gp}})L_{\mathrm{s}}. \tag{2.3.10}$$

With the above equations in hand, the resonator frequency, kinetic inductance and CPW impedance $Z_{\mathrm{l}} = \sqrt{C_{\mathrm{l}}/L_{\mathrm{l}}}$ can be straightforwardly calculated.

Additionally, the kinetic inductance fraction of the transmission line can be formulated,

$$\alpha_{\mathrm{k}} = \frac{L_{\mathrm{k,l}}}{L_{\mathrm{g,l}} + L_{\mathrm{k,l}}}\,, \tag{2.3.11}$$

which quantifies the fraction of kinetic inductance over the total inductance and will be used to express the resonator observables in the next section. By combining Eqs. 2.3.1, 2.3.2, 2.3.4, 2.3.10, the kinetic inductance fraction can be used to express the resonator frequency in terms of the resonator length, its effective dielectric constant and kinetic inductance:

$$F_0 = \frac{c}{4\ell_{\mathrm{res}}}\sqrt{\frac{1-\alpha_{\mathrm{k}}}{\varepsilon_{\mathrm{eff}}}}\,, \tag{2.3.12}$$

with c is the speed of light.

The quality factor of a resonator specifies the frequency selectivity of the resonator and is generally defined as $Q = \omega E_{\mathrm{stored}}/P_{\mathrm{loss}}$, the ratio of stored energy over energy loss per cycle. Alternatively, $Q = F_0/\Delta F$ with ΔF the width of the resonance. Two quality factors are distinguished: Q_{i} due to the internal losses in the resonator and Q_{c} due to the capacitive coupling to the feedline. The internal quality factor is given by [27]

$$Q_{\mathrm{i}} = \frac{1}{\alpha_{\mathrm{k}}}\frac{\omega L_{\mathrm{s}}}{R_{\mathrm{s}}} = \frac{2}{\alpha_{\mathrm{k}}\beta}\frac{\sigma_2}{\sigma_1}\,, \tag{2.3.13}$$

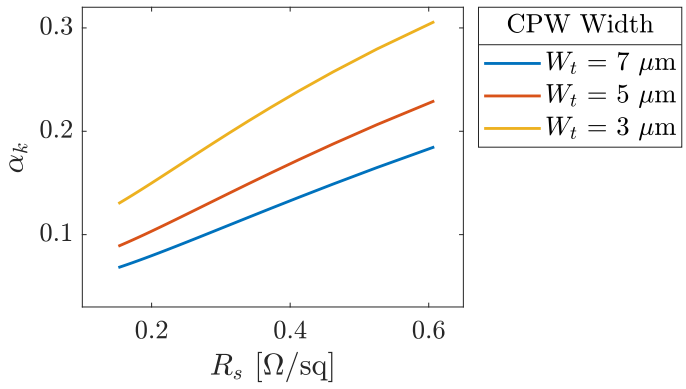

Figure 2.6 – Kinetic inductance fraction α_k of a $\lambda/4$ resonator such as shown in Fig. 2.5 as a function of sheet resistance R_s for various CPW widths. It is clear from the graph that smaller CPW widths and higher sheet resistances increase α_k. The resonator has length $l = 5\,\text{mm}$, with the blue line corresponding to $S = 2\,\mu\text{m}$, $W = 3\,\mu\text{m}$ which are changed proportionally for decreasing total CPW width. Layer thickness $d = 100\,\text{nm}$ and the resistivity is set to $\rho = R_s d = 1.52\,\mu\Omega\text{cm}$.

where the factor β is a parameter dependent on film thickness and penetration depth. For thin films ($d < \lambda$), $\beta \simeq 2$ [27]. Based on Fig. 2.2, the internal quality factor $Q_i \sim 10^7$. Combined, the internal and coupling quality factor give the loaded quality factor

$$\frac{1}{Q} = \frac{1}{Q_c} + \frac{1}{Q_i}\,. \tag{2.3.14}$$

To multiplex many resonators on a single feedline within a limited total bandwidth, high quality factors are necessary as to avoid frequency overlap. Typical values for the MKIDs in this report are $Q_i \gg Q_c \sim 10^5$ and therefore $Q \simeq Q_c$. This leads to resonator bandwidths in the order of 60 kHz for a resonator frequency of 6 GHz, an example of which is shown in Fig.2.7.

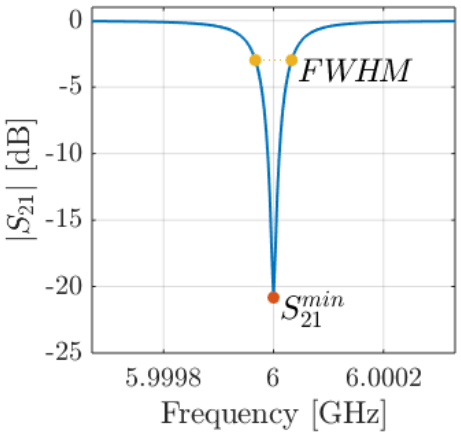

Figure 2.7 – Absolute transmission $|S_{21}|$ through the feedline as a function of microwave frequency for a quarterwave resonator with $F_0 = 6\,\text{GHz}, Q_i = 1 \times 10^6$ and $Q_c = 1 \times 10^5$. The Full Width Half Maximum *FWHM* indicates the bandwidth, $F_0/Q = 66\,\text{kHz}$. The transmission is only attenuated in a narrow bandwidth around F_0, which allows multiplexing many resonators on a single feedline.

In an experiment, the resonance frequency and quality factors are obtained by first measuring the transmission S_{21} over a frequency sweep, locating the transmission dips S_{21}^{min} and a subsequent parameter fit of

$$S_{21}^{\text{min}} = \frac{Q}{Q_i} \tag{2.3.15}$$

and

$$S_{21} = \frac{S_{21}^{\text{min}} + i2Q\frac{\delta F}{F_0}}{1 + i2Q\frac{\delta F}{F_0}}\,. \tag{2.3.16}$$

In summary, a description is given of superconducting coplanar waveguides focussing on the (kinetic) inductance contribution, the resonance frequency and quality factors. The complex transmission S_{21} is expressed in terms of the KID quality factors. This allows for an easy determination of the Q-factors and F_0 by performing a frequency sweep and a fit to the resonance dip as seen in the absolute transmission. Combined with the expressions for complex conductivity, it is finally possible to express the change in resonator observables to a change in quasiparticle density.

2.3.1 Response in Resonator Observables

This section describes the response in resonator observables upon a change in quasiparticle density, ($\mathrm{d}A/\mathrm{d}N_{\mathrm{qp}}$ and $\mathrm{d}\theta/\mathrm{d}N_{\mathrm{qp}}$). The resonator behaviour is characterised by its frequency and quality factor. Variations of the complex conductivity show up as alterations in frequency and quality factor. In practice, this is read out as a response in phase and amplitude. Based on the expressions for frequency and quality factor given in the previous section, the response of both ω_0 and Q_{i} upon a change in complex conductivity can be derived through the surface inductance L_{s}. Since $\omega_0 \propto 1/\sqrt{L_{\mathrm{l}}C_{\mathrm{l}}}$, the relative frequency change is related to the surface inductance as $\delta\omega_0/\omega = -\frac{1}{2}\alpha_{\mathrm{k}}\delta L_{\mathrm{s}}/L_{\mathrm{s}}$. The kinetic inductance fraction α_{k} is included to account for the fact that ω_0 depends on the total inductance while only the kinetic inductance is changed. Furthermore, $\delta L_{\mathrm{s}}/L_{\mathrm{s}} \propto -\frac{1}{2}\beta\,\delta\sigma_2/\sigma_2$, by which the resonance frequency change due to a change in complex conductivity can be expressed as

$$\frac{\delta\omega_0}{\omega_0} = \frac{\alpha_{\mathrm{k}}\beta}{4}\frac{\delta\sigma_2}{\sigma_2} \tag{2.3.17}$$

where $\delta\omega_0 = \omega - \omega_0$ is the frequency shift. By similar arguments [22], the response of the internal quality factor is

$$\delta\big(\frac{1}{Q_{\mathrm{i}}}\big) = \frac{\alpha_{\mathrm{k}}\beta}{2}\frac{\delta\sigma_1}{\sigma_2} \tag{2.3.18}$$

As shown in 2.8a, the complex transmission S_{21} traces out a resonance circle. The response of the resonator is read out using the center of this resonance circle as reference, based on which the amplitude and phase change of the signal are defined. The response in resonator observables, amplitude A and phase θ, to a change in N_{qp} is given by [16]:

$$\frac{\mathrm{d}A}{\mathrm{d}N_{\mathrm{qp}}} = -\frac{\alpha_{\mathrm{k}}\beta Q}{V|\sigma|}\frac{\mathrm{d}\sigma_1}{\mathrm{d}n_{\mathrm{qp}}} \tag{2.3.19}$$

$$\frac{\mathrm{d}\theta}{\mathrm{d}N_{\mathrm{qp}}} = -\frac{\alpha_{\mathrm{k}}\beta Q}{V|\sigma|}\frac{\mathrm{d}\sigma_2}{\mathrm{d}n_{\mathrm{qp}}} \tag{2.3.20}$$

where V is the resonator volume and Q the loaded quality factor. The quality factor is assumed to be constant as it is limited by the coupling quality factor, $Q_{\mathrm{c}} \ll Q_{\mathrm{i}}$. The above equations state the response in resonator observables upon variations in the complex conductivity due to a change in quasiparticle density. The frequency is affected by σ_2, the inductive term due to Cooper pairs, which is observed as a response in the phase. The dissipative term σ_1 due to quasiparticles affects the quality factor and is read out as a response in amplitude.

From the prefactors in both equations it is clear that a high response is obtained by a high quality factor, high kinetic inductance fraction and low volumes.

2.4 Noise

This section reviews several noise sources present in an MKID. They can be categorised by being either fundamental, i.e. related to quasiparticle physics, or being an excess noise source, which can be eliminated or reduced by a good design. Generation Recombination noise and photon noise are fundamental noise sources due to quasiparticle fluctuations and photon fluctuations, respectively. TLS noise and amplifier noise are excess noise sources. Throughout this section, the contributions to the NEP (section 2.4.5) are clarified as well.

2.4.1 Fundamental Noise: Generation Recombination Noise

Generation-Recombination noise, or G-R noise in short, is an intrinsic noise source of the detector and caused by thermally driven fluctuations in the number of quasiparticles of a device in thermal equilibrium. It arises from a random process of quasiparticle generation and recombination into Cooper pairs. Hence, the variance equals N_{qp}. The power spectral density of fluctuations in the resonator phase due to G-R noise is

$$S_{\theta,\mathrm{GR}}(f) = \frac{4N_{\mathrm{qp}}\tau_{\mathrm{qp}}}{1+(2\pi f\tau_{\mathrm{qp}})^2}\left(\frac{\mathrm{d}\theta}{\mathrm{d}N_{\mathrm{qp}}}\right)^2, \tag{2.4.1}$$

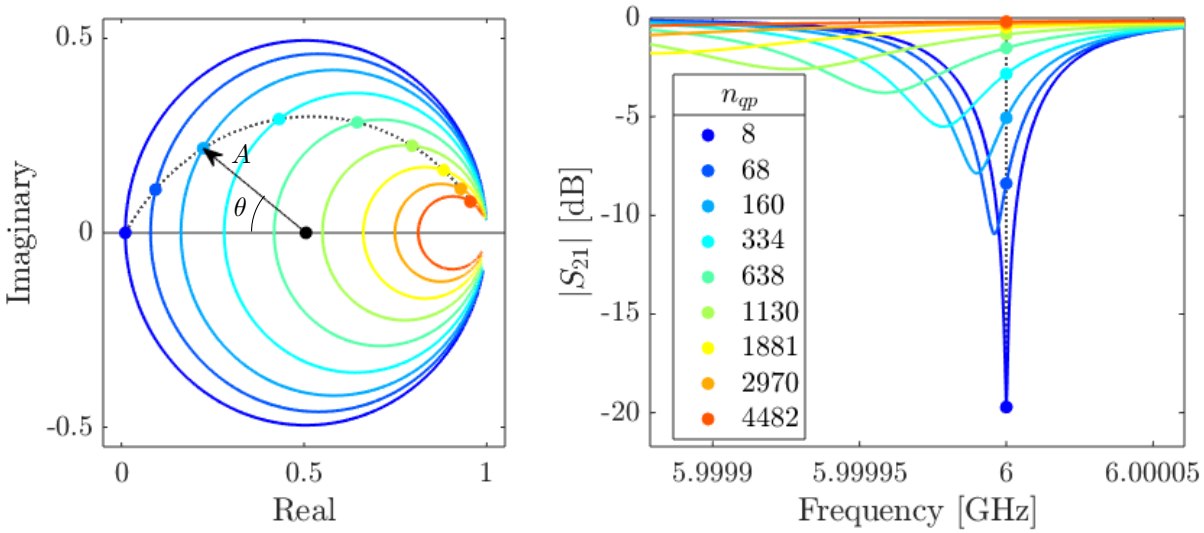

Figure 2.8 – Resonance circle and magnitude of the complex transmission S_{21} for increasing quasiparticle densities. The change in resonance frequency and quality factor due to the quasiparticle density increase as shown in **(b)** are read out using a phase and amplitude response with respect to the center of the resonance circle as in **(a)** using a single readout tone at the unperturbed resonance frequency of the KID.

in which f is the frequency of the spectrum. As mentioned in section 1.2.1, two spectral characteristics indicate a G-R noise limited system. First, a temperature independent noise level set by the product $N_{\mathrm{qp}}\tau_{\mathrm{qp}}$ in the nominator ($N_{\mathrm{qp}} \propto 1/\tau_{\mathrm{qp}}$), assuming a constant phase response. Second, a temperature dependent roll-off of the spectrum imposed by the characteristic timescale of the system, the recombination time $\tau_{\mathrm{qp}}(n_{\mathrm{qp}})$ [17]. If G-R noise is visible in an experimentally obtained PSD, both τ_{qp} and N_{qp} can be inferred from a fit to the roll-off and the constant noise level, respectively, using an independent measurement of $\mathrm{d}\theta/\mathrm{d}N_{\mathrm{qp}}$, which is normally determined using a measurement of the response of the MKID to changes in the bath temperature and using Eq.2.1.2 to convert temperature into quasiparticle density. Consequently, it allows for a determination of the G-R noise limited sensitivity,

$$NEP_{\mathrm{GR}} = \frac{2\Delta}{\eta_{\mathrm{pb}}}\sqrt{\frac{N_{\mathrm{qp}}}{\tau_{\mathrm{qp}}}}, \tag{2.4.2}$$

where η_{pb} is a pair-breaking efficiency factor which is clarified at the end of this section. it is possible to reduce the NEP_{GR}, by decreasing the temperature and/or decreasing the resonator volume, which becomes clear by realising once again that $1/\tau_{\mathrm{qp}} \propto N_{\mathrm{qp}} \propto \exp(-\Delta/k_{\mathrm{B}}T)$, thus $NEP_{\mathrm{GR}} \propto N_{\mathrm{qp}}$. Assuming a constant quasiparticle density in thermal equilibrium, a volume reduction lowers $N_{\mathrm{qp}} = n_{\mathrm{qp}}V$ and thereby the NEP_{GR}.

Pair-breaking efficiency

The pair-breaking efficiency factor states the fraction of a single photon energy ($h\nu_{\mathrm{rad}}$) that ends up as quasiparticles with energy $E \sim \Delta$ [28]. The efficiency η_{pb} is smaller than unity because radiation is not solely absorbed by breaking Cooper pairs but part of the energy is lost as heat, or phonon loss. Guruswamy *et al* [29] calculated η_{pb} for superconducting thin-films of different materials and pair-breaking photons, including the presence of a sub-gap microwave signal such as used to probe MKIDs. For the MKIDs in this report, an aluminium superconductor with $h\nu_{\mathrm{gap}} \sim 16\Delta$ and $\tau_{\mathrm{l}}/\tau_0^{\phi} \sim .5$ [5] (phonon escape time τ_{l} and phonon lifetime τ_0^{ϕ}), the pair-breaking efficiency is $\eta_{\mathrm{pb}} = 0.4$.

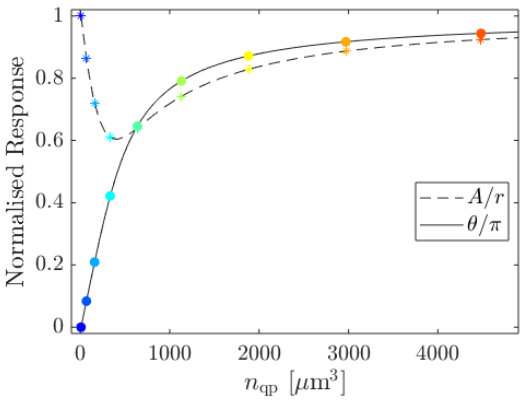

Figure 2.9 – Normalised amplitude and phase response as function of quasiparticle density. The amplitude is normalised to the radius r of the resonance circle. The phase response linearly increases for small n_{qp} and is overall higher than the amplitude response.

2.4.2 Fundamental Noise: Photon Noise

Photon noise is caused by random fluctuations in the arrival rate of the photons. Because the radiation falling on the detector is basically a stream of photons, the random arrival rate constitutes an intrinsic noise source. Since an MKID is sensitive to quasiparticles, the radiation power is converted to a resultant number of created quasiparticles, which is given by

$$N_{qp} = \frac{\eta_{pb}\eta_{opt}\tau_{qp}P_{rad}}{\Delta}\,. \tag{2.4.3}$$

Incident photons couple to the MKID with an efficiency η_{opt}, the optical efficiency, after which the photon is absorbed by creating quasiparticles with an efficiency η_{pb}, the pair-breaking efficiency. As such, both efficiencies affect the response of the device to pair-breaking photons. The PSD of the phase noise due to fluctuations in photon arrival rate is

$$S_{\theta,P}(f) = \frac{2P_{rad}\hbar\nu(1+mO_\nu)}{1+(2\pi f\tau_{qp})^2}\left(\frac{d\theta}{dP_{rad}}\right)^2 \tag{2.4.4}$$

With $m \simeq 0.1$ the total coupling between source and detector and O_ν the occupation number per mode, expressed as $O_\nu = (\exp(h\nu/k_BT_{BB})-1)^{-1}$ [30]. For photon energies $h\nu > k_BT_{BB}$, the mode occupation term is small $O_\nu \ll 1$, as is the case for the MKIDs discussed in this report, with $\nu = 1.54\,\text{THz}$ and $T \simeq T_c/10$.

In this description of the photon noise, the G-R noise was omitted but adds a term to the total noise as well. Now, the NEP contribution of both photon noise and G-R noise can be expressed in terms of P_{rad} by combining Eqs. 2.4.11, 2.4.12 and noticing that $dN_{qp}/dP_{rad} = \eta\tau_{qp}/\Delta$ from Eq. 2.4.3:

$$NEP^2_{photon} = NEP^2_{poisson} + NEP^2_{bunch} + NEP^2_{GR} \tag{2.4.5}$$

$$= 2P_{rad}h\nu(1+mO_\nu) + 4\Delta P_{rad}/\eta_{pb} \tag{2.4.6}$$

When photon noise dominates all other noise sources, the photon-limited noise equivalent power is approximately [31].

$$NEP \simeq \sqrt{2P_{rad}h\nu}\,. \tag{2.4.7}$$

These equations describe the theoretical NEP of a detector under illumination. When combined with the measured NEP, this allows the optical efficiency η_{opt} to be determined, as given by Eq. 2.4.13.

2.4.3 Excess noise: Two-level System Noise

A commonly observed, dominant noise source in superconducting resonators are fluctuating two-level systems (TLS) [32]. TLSs reside in the dielectric layers such as the substrate, where they act as electric dipoles

affecting the dielectric constant of the material. As such, TLS noise fundamentally affects the resonator frequency, creating phase noise. Because the noise is entirely in the phase direction, it can be easily distinguished from photon noise or quasiparticle noise, as the latter two would alter both σ_1 and σ_2, resulting in both amplitude and phase noise [33].

Gao *et al* [34] have shown that the TLS noise in superconducting resonators is dominated by surface states on the dielectric material, i.e. on the surfaces in the gaps between the metallization. They showed that TLS noise is the dominant noise in MKIDs phase noise in most circumstances.

They found that the frequency noise is related to the total width of the resonator as $W_{\mathrm{tot}}^{-1.6}$ [34], and can be modelled with the assumption that TLSs appear solely at the surface of the CPW resonator [35]. Furthermore, they quantified the TLS noise dependency on internal power and modulation frequency for several superconductor-substrate material combinations, which scales as $P_{\mathrm{int}}^{-0.5}$, $f^{-0.5}$, respectively [33].

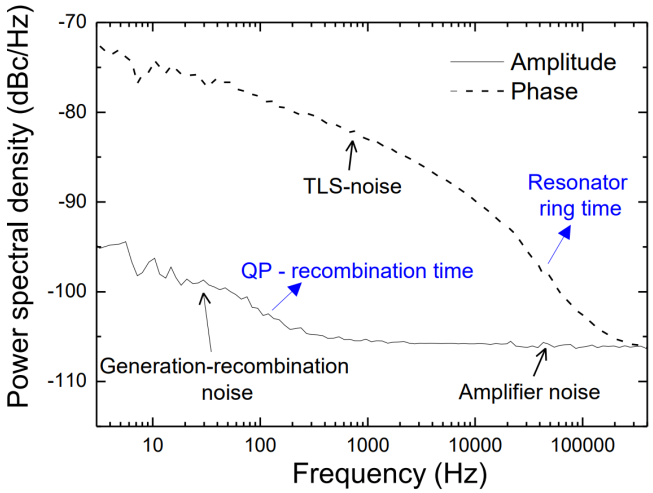

Figure 2.10 – Power spectral density of measured amplitude and phase of an aluminium coplanar waveguide resonator at $T = 120\,\mathrm{mK}$ as a function of modulation frequency. The spectrum shows the TLS noise in the phase readout, completely obscuring the roll-off due to the quasiparticle recombination time, which is indicated at the amplitude spectrum. The amplifier noise is a white noise and due to readout electronics (Sec. 2.4.4). Picture from [22]

Figure 2.10 shows the noise power spectral density in amplitude and phase readout of an aluminium resonator on a sapphire substrate [22]. The amplitude noise is significantly lower than the phase noise. Furthermore, for modulation frequencies up to the resonator ringtime, the phase noise is dominated by TLS noise and scales as $f^{-1/2}$.

To make a comparison between resonators of varying resonance frequency and quality factor, fractional frequency noise $S_{\delta \mathrm{F}_0}/F_0^2$ is used, which is given in terms of measured phase noise as [33]

$$\frac{S_{\delta \mathrm{F}_0}}{F_0^2} = \frac{S_\theta}{(4Q)^2}\,. \tag{2.4.8}$$

The internal power is expressed as the power coupled to the $(\lambda/4)$ resonator, in terms of readout power and quality factors,

$$P_{\mathrm{int}} = \frac{2}{\pi}\frac{Q^2}{Q_{\mathrm{c}}} P_{\mathrm{read}}\,. \tag{2.4.9}$$

The TLS noise as measured on various substrates with different superconducting materials was characterised [36]. Fig. 2.11 shows the material dependent TLS noise in terms of the fractional frequency noise, in dBc/Hz, as a function of the power internal to the resonator. It is immediately obvious that for all materials, the noise scales as $P^{-1/2}$. Besides, silicon substrates have around 5 dB lower noise compared to sapphire substrates. The above mentioned dependencies on material allow for a calculation of the TLS contribution in a CPW.

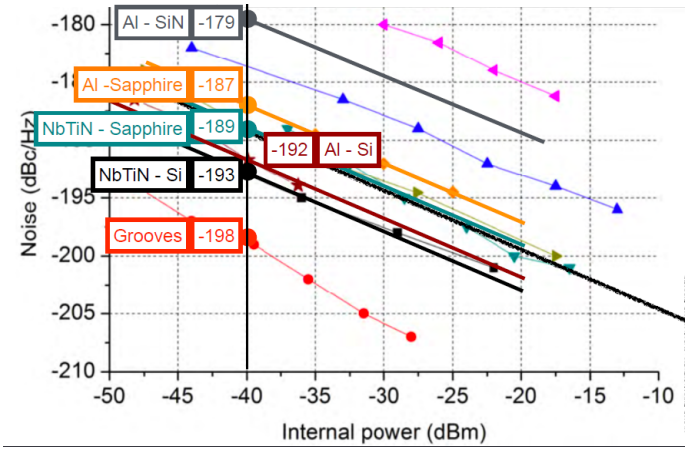

Figure 2.11 – Material dependencies of TLS noise as a function of internal power (P_{int}). The reference values are: temperature $T = 120\,\mathrm{mK}$, modulation frequency $f_{\mathrm{ref}} = 1\,\mathrm{kHz}$, internal power $P_{\mathrm{int,ref}} = -40\,\mathrm{dBm}$. Picture from [36].

One last result from Gao *et al* [35] and Mazin [16] with important implications for the hybrid MKID (see section 2.5) is a position dependent TLS contribution along the length of the resonator. Based on model which assumes a TLS surface distribution in a CPW resonator, they showed that the noise scales with the electric field as E^3 [35] which is in turn position dependent along the length of the quarterwave resonator. This implies that TLS noise mainly stems from the coupler side and minimises at the shorted antenna side, in accordance with the standing (quarter) wave pattern of the electric field in the resonator.

Important implications for the device design can be drawn from the above results. In Chapter 3, this will be the basis of minimising the TLS noise in an MKID model.

2.4.4 Excess Noise: Readout or Amplifier Noise

The electronic setup used to readout the MKID system adds a noise spectrum as well. In a good system, the noise is dominated by the cryogenic low noise amplifier (LNA) connected to the sample. The LNA adds a white noise spectrum, a constant power spectral density. The noise is incorporated in the amplified, transmitted signal S_{21} and therefore does not originate from quasiparticle fluctuations, it is an external noise source. The LNA noise can be converted to phase and amplitude noise, it depends on the amplifier noise temperature T_{N} and is given by [22, 27]

$$S_{\theta,\mathrm{A}}^{\mathrm{LNA}} = \frac{k_{\mathrm{B}} T_{\mathrm{N}}}{r^2 P_{\mathrm{read}}}\,, \tag{2.4.10}$$

with $T_{\mathrm{N}} \sim 4\,\mathrm{K}$, readout power P_{read} and radius of the resonance circle $r = \frac{1}{2}(1 - S_{21}^{\mathrm{min}})$. In Fig. 2.10, the readout noise (Amplifier noise) is apparent in the amplitude spectrum. Increasing P_{read} lowers the readout noise ($\propto 1/P_{\mathrm{read}}$) and TLS noise ($\propto \sqrt{P_{\mathrm{read}}}$). However, as argued in section 1.2.2, increasing P_{read} increases the quasiparticle density, thereby increasing NEP_{GR}. On the other hand, decreasing P_{read} increases readout noise which could dominate the photon and G-R noise contributions and can thereby limit the NEP. Hence, typically, a readout power optimum is observed that gives the best NEP [36].

Experimentally, the readout noise contribution can be easily obtained from the PSD at high modulation frequencies ($2\pi f \gg 1/\tau_{\mathrm{qp}}$), because the recombination time basically acts as a low-pass filter for the other noise sources.

2.4.5 Noise Equivalent Power

The device sensitivity is expressed as the noise-equivalent-power (NEP). It is defined as the power that gives a signal-to-noise ratio (SNR) of 1 in an integration time of 0.5 sec, at a given modulation frequency. It states the minimum detectable power per $\sqrt{\mathrm{Hz}}$. The NEP can be obtained from the responsivity and the noise.

If the PSD of the resonator phase noise S_θ (in rad^2/Hz) is known and combined with phase response to a change in radiation power $P_{\rm rad}$ [16]:

$$NEP_{\rm exp}(f) = \sqrt{S_\theta}\left(\frac{{\rm d}\theta}{{\rm d}P_{\rm rad}}\right)^{-1}\sqrt{1+(2\pi f\tau_{\rm qp})^2}\sqrt{1+(2\pi f\tau_{\rm res})^2}\,, \tag{2.4.11}$$

where f is the modulation frequency and $\tau_{\rm res} = Q/\pi f_0$ is the resonator ringtime. The expression for amplitude noise (in 1/Hz) is similar. For the MKIDs discussed in this thesis, $\tau_{\rm res} \simeq 6\,\mu$m and $\tau_{\rm qp} \gg \tau_{\rm res}$. Therefore, the resonator ringtime only becomes significant after the roll-off determined by the recombination time. The responsivity ${\rm d}\theta/{\rm d}P_{\rm rad}$ stated here can be rewritten in terms of a quasiparticle number change as,

$$\frac{{\rm d}\theta}{{\rm d}P_{\rm rad}} = \frac{{\rm d}\theta}{{\rm d}N_{\rm qp}}\frac{{\rm d}N_{\rm qp}}{{\rm d}P_{\rm rad}}\,, \tag{2.4.12}$$

were ${\rm d}N_{\rm qp}/{\rm d}P_{\rm rad}$ reflects the change in the number of quasiparticles upon a change in radiation power and is further discussed in 2.4.2. Experimentally, the NEP is retrieved from measuring the signal transmission as (amplitude or phase readout) as a function of time [31] and a subsequent calculation of the PSD. Then, the response ${\rm d}\theta/{\rm d}P_{\rm rad}$ is obtained by varying $P_{\rm rad}$ around its reference point and a subsequent fit to the measured phase response. A theoretical NEP can be formulated as well, comprising several terms resulting from different noise sources as discussed in section 2.4.2, and given by Eq. 2.4.5.
As an example, results of Yates *et al* [31] are shown in Fig. 2.12 in which the experimental NEP of a hybrid MKID is determined. For several radiation powers (optical loading), they calculated the PSD from a measurement of the amplitude signal as a function of time. The responsivity is determined by varying $P_{\rm rad}$ around its reference value and a subsequent linear fit to the amplitude response. Combined, this results in an 'optical spectral density', $\sqrt{S_{\rm A}}({\rm d}A/{\rm d}P)^{-1}$ as shown in Fig. 2.12a, which differs from the NEP by the factor $\sqrt{(1+(2\pi f\tau_{\rm qp})^2)}\sqrt{(1+(2\pi f\tau_{\rm res})^2)}$ (see Eq. 2.4.11). At low powers, the noise is dominated by $S^{\rm LNA}$, indicated by the red diamonds in both graphs. At high powers, a power dependent roll-off is visible, indicating a photon-noise limited regime.

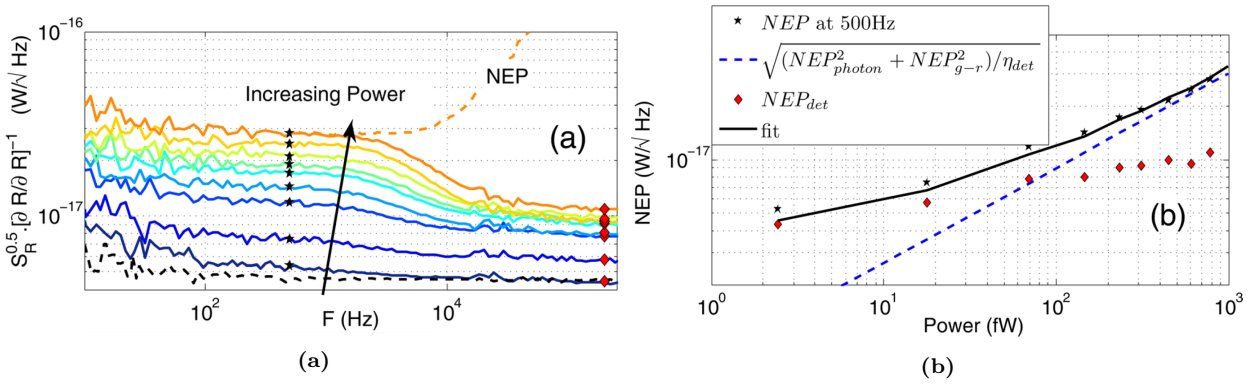

Figure 2.12 – Results of photon noise limited radiation detection with an MKID detector by Yates *et al*[31]. **(a)**The optical spectral density, $\sqrt{S_{\rm A}}\frac{{\rm d}A}{{\rm d}P_{\rm read}}$, equals the NEP up to a factor $\sqrt{(1+(2\pi f\tau_{\rm qp})^2)}$ and is plotted for increasing radiation powers alongside the experimental NEP at 500 Hz indicated by the black stars, and $NEP_{\rm det}$ due to the LNA noise is determined at $f \gg 1/2\pi\tau_{\rm qp}$. **(b)** The NEP for the same data as in (a) as function of radiation power, together with the theoreqetical photon and G-R noise contribution (dotted blue line) and a fit to the measured data by which the optical efficiency is obtained.

Fig. 2.12b shows the noise-equivalent power as a function of radiation power, including both a theoretical NEP (dotted blue line), the experimental obtained NEP at 500 Hz (black stars) and the detector contribution (red diamonds). It nicely illustrates that at high powers ($P_{\rm rad} > 100$ fW), the measured NEP becomes photon-limited and approaches the expected theoretical $\sqrt{P}$ dependency.

Lastly, the optical efficiency ($\eta_{\rm opt}$, here indicated as $\eta_{\rm det}$) is calculated by substracting $NEP_{\rm det}$ from NEP at 500 Hz and fitting the theoretical optical NEP.

Optical efficiency obtained from the theoretical and experimental NEP (Eqs. 2.4.5, 2.4.11), as described in detail by Ferrari *et al* [37], with $P_{\rm abs} = \eta_{\rm opt} P_{\rm s}$,

$$\eta_{\rm opt} = \frac{2P_{\rm s}h\nu + 4\Delta P_{\rm s}/\eta_{\rm pb}}{NEP^2_{\rm exp} - NEP^2_{\rm det} - 2P_{\rm s}h\nu F_\nu O_\nu} \,. \tag{2.4.13}$$

2.5 Hybrid MKID

This section provides a description of the hybrid MKID, which is the standard MKID detector from SRON/TU Delft. It serves as a basis for the MKID model in Chapter 3. A hybrid MKID is a resonator consisting of two sections of different material and dimensions, the advantage of which is both a noise reduction and an increased responsivity [38]. Fig. 2.13 shows an antenna-coupled hybrid structure as given by Janssen *et al* [39]. It consists of a thin Aluminium (Al) CPW connected to a wide Niobium-Titanium-Nitride (NbTiN) CPW on a Silicon substrate and a NbTiN groundplane. The main resonator body material

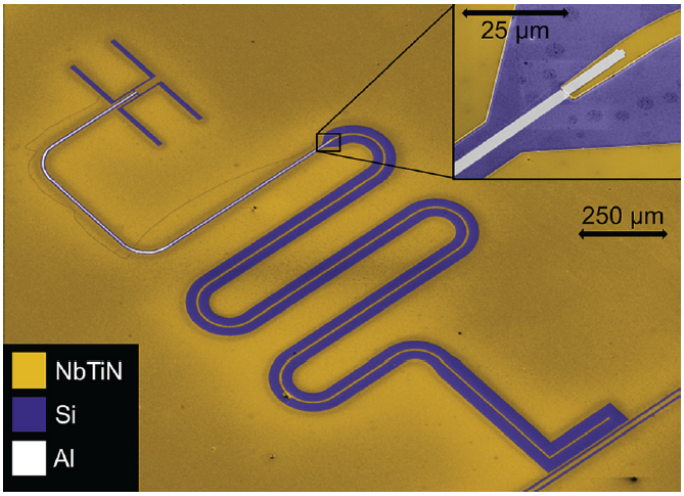

Figure 2.13 – Coloured SEM image of an antenna-coupled NbTiN-Al MKID on a Silicon substrate from Janssen *et al* [39]. The MKID is a quarterwave CPW resonator (5 mm) with a narrow Aluminium section (1 mm) shorted to the NbTiN groundplane at the antenna and a wide NbTiN section (4 mm) capacitively coupled to the feedline. Photons of energies exceeding $\Delta_{\rm Al}$ and lower than $\Delta_{\rm NbTiN}$ are absorbed in the Al line. This corresponds to frequencies $0.09 < \nu_{\rm rad} < 1.1$ THz.

is NbTiN with $T_{\rm c} = 14.5$ K which gives $2\Delta_{\rm NbTiN} = 1.1$ THz. It is dissipationless for microwave frequencies and has lower TLS noise in comparison to Al (Fig. 2.11). Moreover, the wide CPW further reduces TLS noise (see Chapter 3 for details). The planar antenna can be independently optimised for the desired radiation frequency; in this case $\nu_{\rm rad} = 350$ GHz.

Radiation is absorbed by pair-breaking in the narrow Al line which therefore forms the responsive part of the MKID. Once created, the quasiparticles are trapped in the Al section since $\Delta_{\rm Al} \simeq 0.2$ meV $< \Delta_{\rm NbTiN} \simeq 2.2$ meV.

Importantly, the hybrid MKID allows for a significant decrease of the active volume. Thereby, $NEP_{\rm GR} \propto \sqrt{V}$ is reduced. At the same time, the absorption of a single photon by creating quasiparticles causes a higher density change when the volume is smaller. Hence, the responsivity is increased (Eqs. 2.3.19, 2.3.20).

Another major advantage of the hybrid structure is its low TLS noise. Although TLS noise can dominate the phase noise of an MKID (such as shown in Fig. 1.7) a significant reduction can be realised by combining a wide CPW (NbTiN section) with a narrow hybrid line (Al section). Therefore, a model is discussed which describes the TLS noise behaviour and its dependencies for a hybrid MKID.

2.5.1 TLS noise model

The TLS noise model is based on the results of Gao *et al* [33–35] on TLS noise in superconducting coplanar waveguides, as discussed in section 2.4.3.

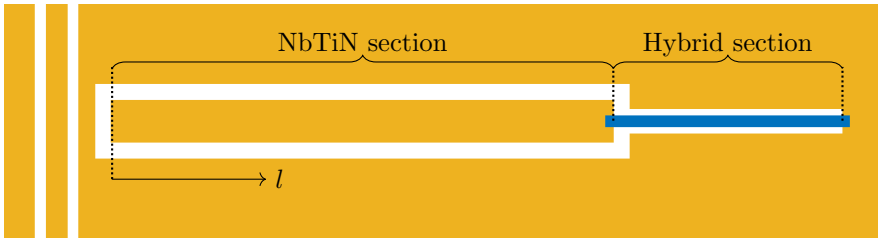

Figure 2.14 – Illustration of the hybrid MKID model. The wide NbTiN section (yellow) allows for a TLS noise reduction while the narrow hybrid section with aluminium central line (blue) allows for a volume reduction without a significant TLS noise increase.

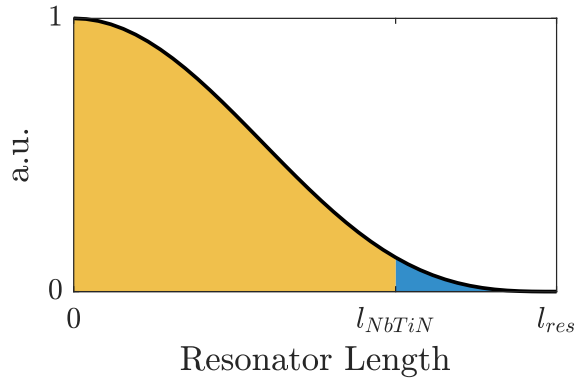

Figure 2.15 – E-field dependence in arbitrary units as function of length seen from the coupler side such as indicated in Fig. 2.14 for a $\lambda/4$ resonator. Due to the E^3 scaling of TLS noise along the resonator length, the TLS contribution of the NbTiN part (yellow) of the MKID dominates over the contribution of the relatively short hybrid Al section (blue). This allows a narrow hybrid CPW section without significantly increasing TLS noise.

TLS noise was shown to be dependent on the CPW total width as $W_\mathrm{t}^{-1.6}$, a readout power dependence due to TLS saturation of $P_\mathrm{read}^{-1/2}$ and a modulation frequency dependence of $f^{-1/2}$. These dependencies are captured in the factor γ with reference values $W_\mathrm{ref}, P_\mathrm{ref}$ and F_ref as reported by Gao *et al* and given in Table 2.1, as well as shown in Fig. 2.11.

$$\gamma = \left(\frac{f}{f_\mathrm{ref}}\right)^\mathrm{a} \left(\frac{P}{P_\mathrm{ref}}\right)^\mathrm{b} \left(\frac{W_\mathrm{t}}{W_\mathrm{t,ref}}\right)^\mathrm{c}, \tag{2.5.1}$$

where

$$a = -0.5, b = -0.5, c = -1.6\,.$$

Furthermore, the TLS noise has an E-field dependence along its length which is proportional to E^3 [35]. The $\lambda/4$ resonator is shorted at the antenna side, leading to a voltage peak at the open-ended coupler side. This implies that the TLSs at the coupler side mainly contribute to the noise. Figure 2.15 shows the E^3 scaling for a hybrid resonator such as illustrated in Fig. 2.14.

Due to the material and position dependency of TLS noise, the noise contribution for a hybrid structure is split in two parts.

$$S_{\theta,1} = \gamma_1 S_{\mathrm{ref},1} \int_0^{l_\mathrm{NbTiN}} \cos^3\left(\frac{\pi}{2}\frac{l'}{l_\mathrm{res}}\right)\mathrm{d}l' \tag{2.5.2}$$

$$S_{\theta,2} = \gamma_2 S_{\mathrm{ref},2} \int_{l_\mathrm{NbTiN}}^{l_\mathrm{res}} \cos^3\left(\frac{\pi}{2}\frac{l'}{l_\mathrm{res}}\right)\mathrm{d}l' \tag{2.5.3}$$

including γ_i (Eq. 2.5.1) and a material specific reference noise $S_\mathrm{ref,i}$ where subscript i indicates the MKID section. The total phase noise due to TLS is the sum of the two parts, taken in units 1/Hz.

$$S_{\theta,\mathrm{TLS}} = S_{\theta,1} + S_{\theta,2} \tag{2.5.4}$$

From the above equations, geometry requirements that decrease TLS noise can be inferred to minimise TLS noise in a hybrid MKID. Namely, a wide NbTiN section at the coupler side where the electric field and thus the TLS noise contribution is high, combined with a narrow Al section at the shorted end. Fig. 2.16 shows

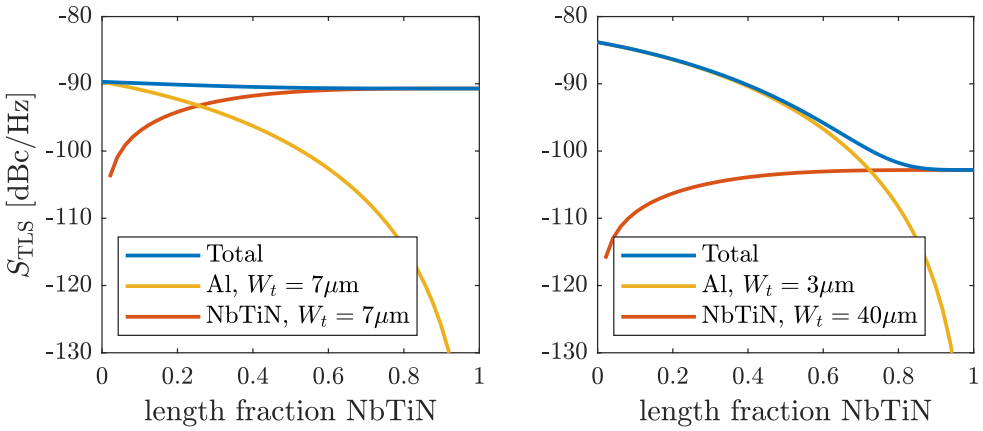

Figure 2.16 – TLS noise contributions of the NbTiN and Al sections and their sum, as a function of fractional length of the NbTiN section over the total resonator length, calculated using Eqs. 2.5.2-2.5.4 and reference values as stated in Table 2.1. The two panels show the influence of CPW width on TLS noise in the resonator. **(left)** reference values, the total TLS noise varies only due to the slight difference in material dependent reference noise of NbTiN and Al. **(right)** Narrow Al line and a wide NbTiN section. The increased coupler width reduces noise NbTiN. Although a narrower Al line increases its TLS noise contribution as indicated by the yellow line, the fractional NbTiN length of a hybrid resonator is generally high ~ 0.9 such that the total TLS noise is indeed reduced.

the TLS noise of the total hybrid MKID and its respective sections, as a function of the fractional length of the NbTiN section. Because the fractional length of NbTiN is generally high ~ 0.9, the short Al section barely contributes to the TLS noise even if the width of the Al section is small (see Fig. 2.16, right panel).

Table 2.1 – Overview of reference values as reported by Gao *et al*, used in the TLS model equations (Eqs. 2.5.1 - 2.5.4). The reference noise values are the metal on silicon substrate values as given by Daalman (Fig. 2.11). Note that S'_{ref} is given in fractional frequency noise but is converted to phase noise (which is also given in dBc/Hz) via $S_{\mathrm{ref}} = S'_{\mathrm{ref}} + 10\log(4Q^2)$

S'_{ref} (NbTiN-Si) (dBc/Hz)	S'_{ref} (Al-Si) (dBc/Hz)	W_{ref} (µm)	P_{ref} (dBm)	f_{ref} (kHz)
−193	−192	7	−40	1

2.5.2 Kinetic Inductance Fraction

A disadvantage of the hybrid structure is that the kinetic inductance fraction (α_{k}) is reduced. The Al line, the responsive part of the resonator, is now just a fraction of the total resonator length and α_{k} is the fraction of kinetic inductance in the central Al line over the total inductance of the resonator.

$$\alpha_{\mathrm{k}} = \frac{L^{\mathrm{Al}}_{\mathrm{k,c}}}{L^{\mathrm{NbTiN}} + L^{\mathrm{Al}}} \tag{2.5.5}$$

where L^{NbTiN} and L^{Al} include both geometric and kinetic inductances per unit length as described in section 2.3 and the lengths of the respective sections.

2.6 MKID improvements

This section discusses MKID sensitivity improvements as previously mentioned in section 1.3 in more detail. The goal of this project is to improve the sensitivity of the detector. This implies a reduction of the G-R limited NEP: $NEP_{\mathrm{GR}} \propto \sqrt{N_{\mathrm{qp}}/\tau_{\mathrm{qp}}}$. This can be achieved by reducing the active volume (Al line) of the resonator, and/or by reducing the readout power. The latter reduces the quasiparticle density and therefore the N_{qp} for a given aluminium volume. Both volume and readout power reduction are considered in this section, along with possible fabrication related issues that should be taken into account in an optimised device design.

The temperature is set at 120 mK, to compromise temperature dependent TLS noise and a low number of thermally generated quasiparticles [40].

2.6.1 Readout Power Reduction

The readout power creates excess quasiparticles due to a process of multiple photon absorption [9, 10]. Hence, τ_{qp} and n_{qp} are limited by P_{read} and saturate the NEP. Reducing P_{read} seems a logical solution. However, reducing P_{read} increases the white noise floor due to the readout, and increases the TLS noise. As a result, the G-R noise is no longer visible.

Experimentally, the readout power can be reduced up to the point were the roll-off due to quasiparticle recombination is still visible, which is determined from observing the power spectral density obtained from the time domain response in resonator observables. Hence, the readout power cannot be easily reduced to decrease the NEP_{GR}. A mitigation of this problem would be to *increase* the G-R noise level, which is possible by increasing the MKID responsivity (see Eq. 2.4.1). Alternatively, the excess noise could be reduced, by reducing the readout noise level through better amplifiers or, for phase readout, by reducing the TLS noise through a better resonator design.

2.6.2 Volume Reduction

Reducing the active volume of the MKID reduces the intrinsic sensitivity limit, NEP_{GR}. This can be seen by writing $NEP_{\mathrm{GR}} \propto \sqrt{N_{\mathrm{qp}}/\tau_{\mathrm{qp}}} \propto n_{\mathrm{qp}}\sqrt{V}$. Note that n_{qp} and τ_{qp} are assumed to be unaffected by the volume reduction. A similar volume dependency is obtained by rewriting the experimental NEP (Eq. 2.4.11),

$$NEP_{\mathrm{GR}} \propto \sqrt{V} \tag{2.6.1}$$

while the G-R noise (Eq. 2.4.1) scales as

$$S_{\theta,\mathrm{GR}} \propto \frac{1}{V}\alpha_{\mathrm{k}}^2 \sim l_{\mathrm{Hybrid}}\,. \tag{2.6.2}$$

Eq. 2.6.2 shows that care has to be taken when V is reduced by shortening the line length of the hybrid section l_{Hybrid}. The level of the phase noise (and amplitude noise as well) due to quasiparticle fluctuations decreases with decreasing l. This can be mitigated by increasing the MKID responsivity or reducing the excess noise sources as discussed in the previous section.

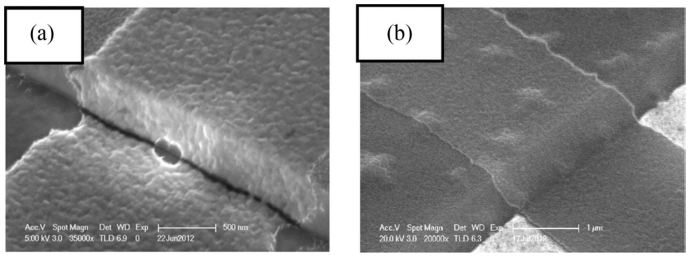

Figure 2.17 – Micrograph photos of thin-film aluminium line crossing the NbTiN-substrate interface from Ferrari *et al* [37].**(a)** On a silicon substrate, the Al layer shows a cut at the transition. **(b)** On a sapphire interface, a smooth transition is observed.

2.6.3 Absorbing all power

In reducing the hybrid volume, all radiation coupled by the antenna into the CPW should still be absorbed in the aluminium section of the MKID. Otherwise, part of the radiation power would be lost in the system without quasiparticle creation, reducing the device sensitivity. The hybrid line length required to absorb a specified fraction of the total radiation power depends on the aluminium sheet resistance ($R_{\mathrm{s,Al}}$) and the linewidth. A narrow, thin line has more absorption per unit length and can thereby also be short. Reducing the line thickness increases R_{s} and thus allows for a length reduction. Therefore, a significant volume reduction should be possible by using thin aluminium lines which provide high sheet resistance $R_{\mathrm{s,Al}}$.

2.6.4 Fabrication Issues for Different Substrates

High resistivities can be obtained by using a silicon (Si) substrate instead of the conventional sapphire substrate. This provides a slightly lower TLS noise ($\sim$ 5dB) as well.

A disadvantage of using Si substrates is fabrication related and two-fold. Firstly, thin-film aluminium deposition on Si substrates has low yield in comparison to sapphire substrates, as shown in Fig. 2.17. Secondly, in hybrid MKIDs, short lifetimes are observed (large n_{qp}) and thereby a high NEP at low temperatures and low signal power. The earlier mentioned assumption of high τ_{qp} is not generally true for MKIDs on silicon. This might be related to substrate roughening during the fabrication process. Therefore, an extra layer to protect the substrate surface can be added, which is further discussed in Chapter 3.

Chapter 3

MKID Model

This chapter describes the model I developed to be able to find the best way of reducing the NEP. This model consists of a MATLAB program that includes all the theory described in Chapter 2. Keeping the main goal of obtaining a low NEP detector in mind, how do material choice and device geometry affect the device? First, a quantitative example is provided to compare the modelled MKID noise and NEP contributions to a reference measurement. Then, specific design features are given for an MKID optimised for 1.54 THz radiation in which the hybrid volume is minimised while radiation absorption is ensured and excess noise is minimal. Thereby, the geometry and material requirements for a low NEP MKID are determined which concludes the MKID model and serves as the basis for the actual MKID design in the next chapter.

3.1 Model Comparison

In this section, the model equations for the noise spectrum and NEP contributions (Eqs. 2.3.19 - 2.4.12, 2.4.1 - 2.4.3, 2.4.9, 2.4.10, 2.5.2, 2.5.4) are compared to existing measured chip parameters to calculate the noise spectrum and NEP of the MKID.

The model is compared to one of the best devices fabricated in SRON-Delft, which is from batch LT020. This is a hybrid NbTiN-Al MKID fabricated on a C-plane sapphire substrate and measured in great detail. Since all DC parameters are known for this device, the model can be used to calculate the expected performance without any free parameters. The input parameters are listed in Table 3.1.

The power spectral density of the measured data are shown together with the model calculation in figure 3.1. The model shows the noise contributions due to TLS noise (using Eqs. 2.5.2, 2.5.4), the amplifier noise (Eq. 2.4.10) and the generation-recombination noise (Eq. 2.4.1).

To obtain these spectra I have used the input parameters as listed in Table 3.1, which are all measured independently or are literature values. From all the individual noise contributions I calculated the total noise in phase and amplitude by adding the power spectral densities. To model the excess quasiparticle density due to the readout power, I used the results given by Visser *et al* [40] using a quasiparticle creation efficiency $\eta_{\mathrm{read}} = 1.1 \times 10^{-4}$. The quasiparticle density and (low temperature) saturated quasiparticle lifetime are modelled by using a corresponding effective temperature. The result of this ab-initio calculation is given in panel a. The data as measured are given in panel b, which shows the phase and amplitude noise for an internal power of -36.8 dBm, which is also used in panel a. There is a quite good agreement between the measured phase noise and the calculated phase noise over the entire spectral range. In particular:

1. The calculated noise at frequencies > 30 kHz agrees very well with the spectrum, indicating a correctly modelled noise contribution of the readout system, which is dominated by the low noise amplifier.

2. The roll-off frequency agrees quite well, indicating that the quasiparticle number is modelled correctly.

3. The calculated phase noise level at frequencies < 100 Hz is 4-5 dB higher than the measurement data.

4. The calculated amplitude noise level at frequencies < 100 Hz is ~ 7 dB higher than the measurement data.

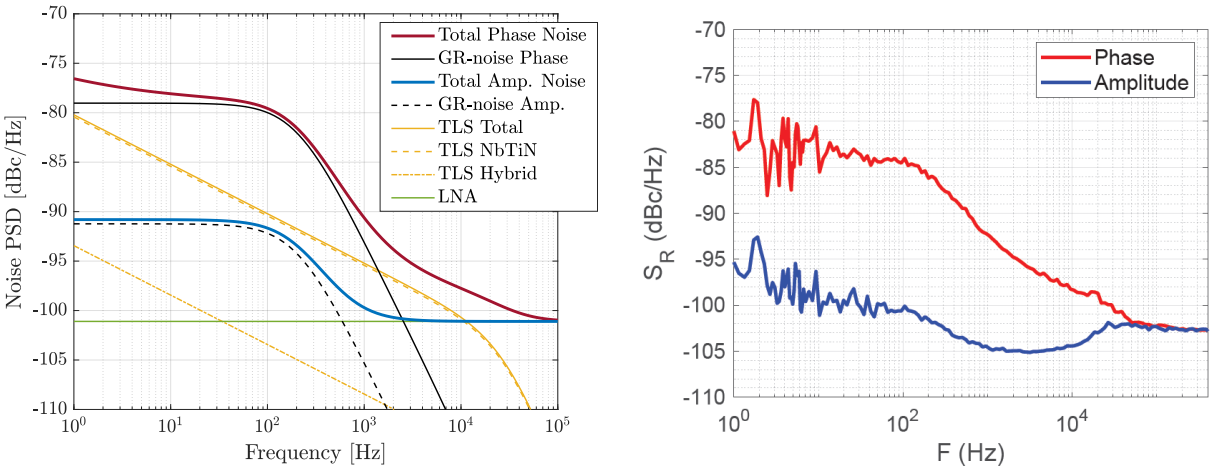

(a) Model **(b)** Measurement data

Figure 3.1 – Noise PSD of existing measured data and modelled noise contributions of different sources based on the values given in Table 1. The modelled phase GR-noise matches the measurement data better than amplitude noise, which is about 5 dB too high. The total phase noise is the sum of $S_{\theta,\mathrm{GR}}, S_{\mathrm{LNA}}$ and S_{TLS}. The total amplitude noise is the sum of $S_{\mathrm{A,GR}}$ and S_{LNA}.

Since the quasiparticle lifetime, given by the roll-off in the spectra, agrees quite well I attribute the noise level difference between measurement and calculation to a small error in the device responsivity. The latter converts the noise in quasiparticle number to a measured noise level. A possible reason for this is that the calculation assumes a thermal quasiparticle population. As argued by de Visser *et al.* [41], high readout powers at low temperatures cause not only an increase in quasiparticle number, but also a change in the electron energy distribution function. Despite this, the model gives a reasonable agreement and can therefore be used to predict the spectra for different device designs reasonably well.

Figure 3.2 shows the NEP as obtained via the modelled phase noise and responsivity, together with the G-R limit, calculated using Eq. 1.2.1, using $\tau_{\mathrm{qp}} = 0.79\,\mathrm{ms}$ and $\Delta = 0.17\,\mathrm{m\,eV}$. An expression for the responsivity is obtained by combining Eqs. 2.4.3, 2.4.12 where $\eta_{\mathrm{opt}} = 1$:

$$\frac{\mathrm{d}\theta}{\mathrm{d}P_{\mathrm{abs}}} = \frac{\eta_{\mathrm{pb}}\tau_{\mathrm{qp}}}{\Delta_{\mathrm{Al}}}\frac{\mathrm{d}\theta}{\mathrm{d}N_{\mathrm{qp}}}\,, \tag{3.1.1}$$

Experimentally, $N_{\mathrm{qp}}(T)$ can be varied by changing the bath (chip) temperature. The (dark) NEP is now straightforwardly obtained via Eq. 2.4.11.

$$NEP = \sqrt{S_\theta}\left(\frac{\mathrm{d}\theta}{\mathrm{d}P}\right)^{-1}\sqrt{1+(2\pi f\tau_{\mathrm{qp}})^2}\sqrt{1+(2\pi f\tau_{\mathrm{res}})^2} \tag{3.1.2}$$

$$= \sqrt{S_\theta}\left(\frac{\eta_{\mathrm{pb}}\tau_{\mathrm{qp}}}{\Delta_{\mathrm{Al}}}\frac{\mathrm{d}\theta}{\mathrm{d}N_{\mathrm{qp}}}\right)^{-1}\sqrt{1+(2\pi f\tau_{\mathrm{qp}})^2}\sqrt{1+(2\pi f\tau_{\mathrm{res}})^2}\,, \tag{3.1.3}$$

where S_θ is the phase noise at the lowest bath temperature. This results in $NEP(f = 10\,\mathrm{Hz}) = 4.5\times10^{-19}\,\mathrm{W}/\sqrt{\mathrm{Hz}}$, with $\tau_{\mathrm{qp}} = 0.79\,\mathrm{ms}$ for the model just described.

Table 3.1 – Overview of reference parameters from LT020, unless otherwise stated. The reference noise S_{ref} is taken 5 dB higher than the fractional frequency noise for a Sapphire substrate as shown in Fig. 2.11. The reference TLS values, based on single layer chips, is observed to be higher due to fabrication related processes affecting the material surface and thereby generally increasing TLS noise [36].

Al/ Hybrid	d (nm)	ρ_{N} (µΩ cm)	T_{c} (K)	S (µm)	W (µm)	ℓ (µm)	S_{ref} (dBc/Hz)
	55	0.77	1.125	1.6	2.2	1101	-187
	η_{pb}	N_0 (µm^{-3}eV^{-1})	τ_0 (ns)	v_{F} (m/s)			
	0.57	1.72×10^{10}	458	2.03×10^{6}			
NbTiN	d (nm)	ρ_{N} (µΩ cm)	T_{c} (K)	S (µm)	W (µm)	ℓ (µm)	S_{ref} (dBc/Hz)
	300	130	14	48	24	6163	-182
KID/ Substrate	ε_{r}	Q_{c}	P_{int} (dBm)	P_{read} (dBm)	LNA T_{N} (K)		
	10.3	7.1×10^{4}	-36.8	-83	6.5		

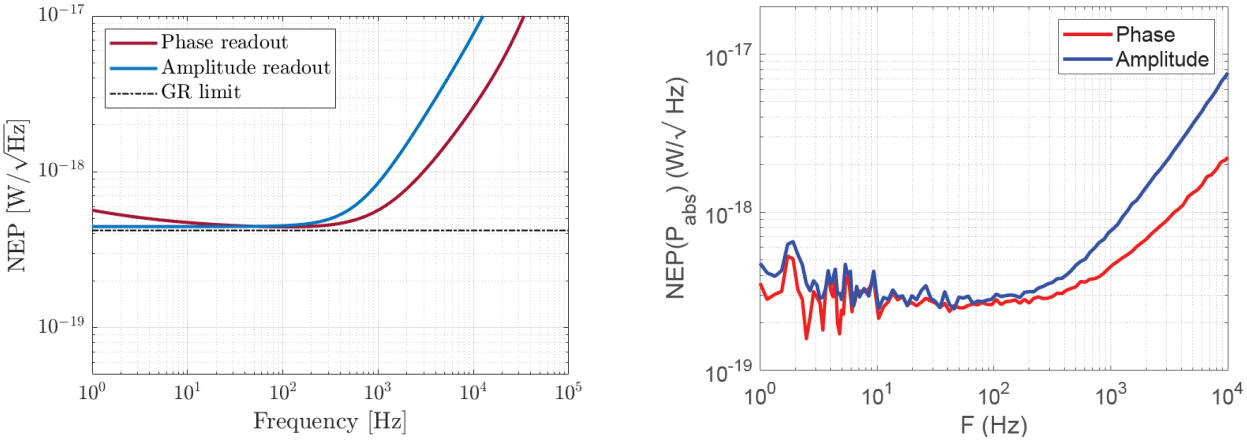

(a) Model **(b)** Measurement data

Figure 3.2 – The NEP for both amplitude and phase readout as obtained from the model using Eq. 3.1.2, based on the values given in Table 3.1, compared with measured NEP from batch LT020. G-R noise limit is graphed as well (dashed-dotted line).

3.2 Towards a low NEP device

As argued before, a straightforward way to reduce the NEP is to reduce the aluminium volume of the MKID. In this section I calculate the change in noise spectra and device NEP when changing the width, thickness and length. An important contraint is that all power coming from the antenna should be absorbed, this will create a minimum line length, depending on its geometry and aluminium sheet resistance.
The smallest possible line width depends on the fabrication process and would be $\sim 1\,\mu m$ using optical lithography and $\sim 0.4\,\mu m$ using E-beam lithography and wet etching. The minimum line thickness is set to 15 nm. First, an illustrative example is given in Fig. 3.3 of the influence of decreasing CPW dimensions on the noise level and NEP. It explicitly shows that a shorter line reduces the PSD noise level (Eq. 2.6.2) while NEP is reduced due to the volume reduction. However, it is clear that just shortening the line has a limited effect on the NEP and that a reduced line length reduces the generation-recombination noise due to quasiparticle fluctuations.

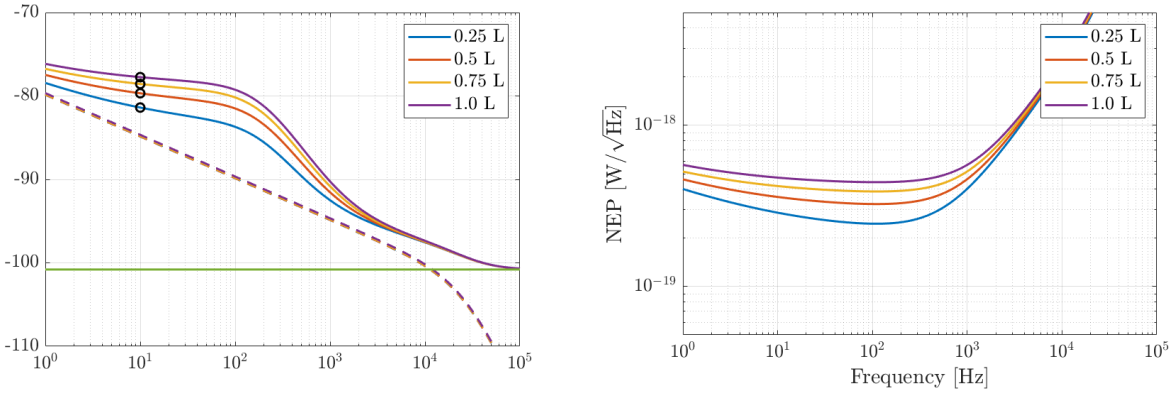

(a) PSD **(b)** NEP

Figure 3.3 – Influence of a decrease in hybrid length on the noise PSD and NEP. **(a)** The phase noise, TLS noise (dashed line) and LNA noise (green line) are shown for decreasing decreasing line lengths relative to the reference values as in Table 3.1. The black dots at a modulation frequency of 10 Hz correspond to the ones graphed in Fig. 3.4a. **(b)** The length reduction lowers the active volume and therefore the NEP.

Fig. 3.4 shows the influence of reducing not only the length of the line, but also the line thickness and width on both the PSD and NEP, plotted together as fractional change with respect to the original values such as indicated in the legend. The black dots at modulation frequency $f = 10$ Hz correspond to the ones shown in Fig. 3.3.

A significant volume reduction $\sim 1/50$ is realised if the CPW dimensions are reduced, which increases the PSD and decreases the NEP as shown in Fig. 3.4b. Furthermore, when the quasiparticle recombination time is increased to 3.5 ms, the $NEP = 2.5 \times 10^{-20}\,\mathrm{W}/\sqrt{\mathrm{Hz}}$, identical to the sensitivity requirement for a space-based 4 K cooled FIR observatory, $NEP = 2.5 \times 10^{-20}\,\mathrm{W}/\sqrt{\mathrm{Hz}}$. Under the assumption that the quasiparticle lifetime, and thereby the quasiparticle density, depends on the readout power in the resonator, as argued by Visser *et al* [9], this implies a rather low internal power should be used of -48.8 dBm, assuming $\tau_{qp} \propto P_{int}^{-0.5}$. This shows, at least qualitatively, that a significant improvement in device performance is possible. Now, a more detailed calculation is needed to check if the simple assumptions are indeed valid.

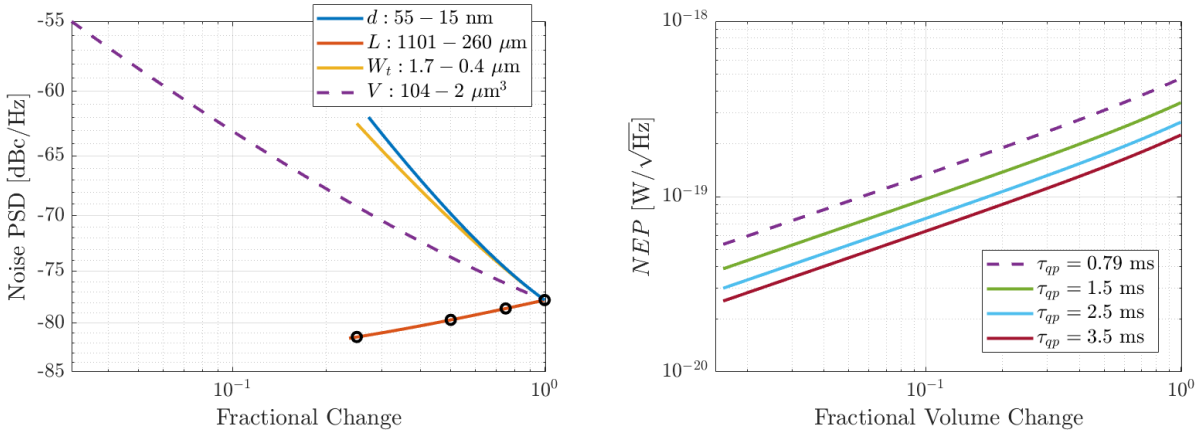

(a) PSD

(b) NEP, volume change V : 104 − 2 µm^3

Figure 3.4 – PSD and NEP at modulation frequency $f = 10$ Hz, as a function of decreasing hybrid CPW line dimensions (thickness d, length L, total width W_t), plotted as fractional change with respect to the reference values as given in Table 1. The resulting volume reduction gives a large total fractional change up to $\sim 1/50$. **(a)** The black dots correspond to the values indicated in Fig. 3.3a. **(b)** NEP as function of fractional volume change for increasing recombination time τ_{qp}. Since $NEP \propto \sqrt{V}$, the NEP at minimum volume and $\tau_{qp} = 3.5$ ms is 2.5×10^{-20} W/$\sqrt{\text{Hz}}$.

Chapter 4

MKID Design

4.1 Hybrid MKID for 1.54 THz radiation

The basis of the hybrid model in this work are the state-of-the-art hybrid MKIDs such as presented by Janssen *et al* [39] (Fig. 2.13) and Baselmans *et al* [5]. The latter reports an average sensitivity $3 \times 10^{-19}\,\mathrm{W}/\sqrt{\mathrm{Hz}}$ for a radiation frequency $\nu_{\mathrm{rad}} = 850\,\mathrm{GHz}$. However, the MKIDs presented in this work are designed for a radiation frequency of 1.54 THz, the reason of which is two fold.

1. Detection of the FIR spectrum up to frequencies of 1 THz is done by ground-based observatories such as the ALMA interferometer [3] and the DESHIMA spectrograph [42] at the frequency windows not fully blocked by the atmosphere of the Earth. However, a space-based observatory such as the future Origins Space Telescope (OST) would be able to access the $1 - 10$ THz frequency range for which the atmosphere is opaque. If cooled to temperatures of a few Kelvin, the otherwise dominant thermal emission in the FIR range is significantly reduced such that the performance is only limited by astrophysical backgrounds, as shown in Fig. 1.1. The detector sensitivity requirement to reach this universe background limited performance in the $1 - 10$ THz band depends on the spectral resolution $R = \nu/\Delta\nu$ and and ranges from $\sim 10^{-19}\,\mathrm{W}/\sqrt{\mathrm{Hz}}$ for a continuum camera up to $\sim 10^{-20}\,\mathrm{W}/\sqrt{\mathrm{Hz}}$ for a spectrometer [43], as shown in Fig.4.1. Since the MKIDs in this work are designed to reach the OST sensitivity requirements, the design should also be optimised for a radiation frequency within the $1-10$ THz band.

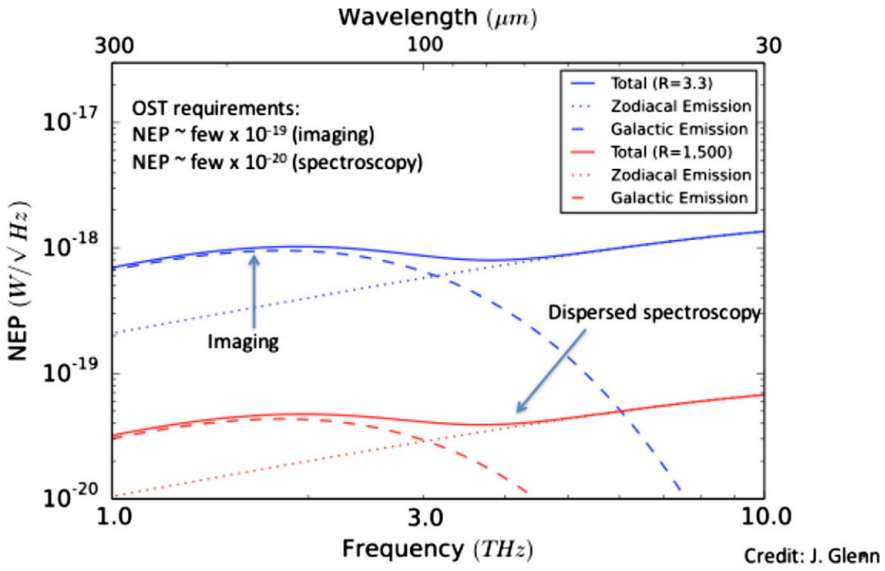

Figure 4.1 – Detector sensitivity requirement in the $1-10$ THz frequency band to reach universe background limited performance for a future 4 K cooled space-based telescope like the Origins Space Telescope (OST). For a spectrometer with a spectral resolution of $R \sim 1000$, the required sensitivity is $\sim 10^{-20}\,\mathrm{W}/\sqrt{\mathrm{Hz}}$. Individual contributions from zodiacal and galactic emission are graphed as well. Picture from [43].

2. The second reason for to design for 1.54 THz is related to the available optical filters in the experimental setup. A radiation source is needed to measure the detector response and sensitivity under illumination. This source is a blackbody of which the temperature can be varied over a range of $3-25$K. The blackbody radiation passes through a set of optical filters providing a narrow bandpass around a certain frequency. Hence, by changing the blackbody temperature, the radiation power incident on the detector can be varied over a wide range, as explained in detail in the section Experimental Setup. With a minimum blackbody temperature of around $T_{\mathrm{BB}} \simeq 3\,\mathrm{K}$, the available filterstack determines the minimum radiation power incident on the detector and thereby also the power dependent NEP due to photon noise (Eq. 2.4.5). Importantly, the range of radiation powers and thereby the NEP_{ph} should extend low enough as to be able to observe a sensitivity saturation due to G-R noise intrinsic to the device, targeted to be $\sim 10^{-20}\mathrm{W}/\sqrt{\mathrm{Hz}}$. That is, the experimental setup should allow to measure the MKID response and sensitivity under dark conditions (no radiation). With a minimum blackbody temperature of around $T_{\mathrm{BB}} \simeq 3\,\mathrm{K}$, the filterstack determines the minimum radiation power falling on the detector. This is shown in Fig. 4.2 for two available filterstacks with a narrow bandpass around 850 GHz and 1540 GHz. It is clear from the graph that at a blackbody temperature of 3 K, only the 1540 GHz filterstack allows for a NEP_{ph} low enough as to reach the OST requirements. Thus, taking the observational and experimental arguments into account, the MKID is designed for 1.54 THz radiation.

4.1.1 Aluminium groundplane

The choice for a 1.54 THz radiation source has consequences for the materials to be used. Aluminium, due to its critical temperature $T_{\mathrm{c}} \simeq 1.28\,\mathrm{K}$, is resistive at frequencies above 90 GHz while NbTiN ($T_{\mathrm{c}} \simeq 14.5\,\mathrm{K}$) is nearly dissipationless for frequencies up to its gap frequency $\nu_{\mathrm{gap}} = 2\Delta_{\mathrm{NbTiN}}/h \simeq 1.1\,\mathrm{THz}$. This is shown in Fig. 4.3, in which the frequency dependent complex conductivity of the two materials are graphed together. Given an MKID with an Al hybrid line and NbTiN groundplanes, photons of frequencies $0.09 < \nu_{\mathrm{rad}} < 1.1\,\mathrm{THz}$ are fully absorbed in the aluminium hybrid line, where the excited quasiparticles are naturally confined to the line by the high superconducting gap of NbTiN. This can be quantified by looking at the fraction of the radiation absorbed by the central line compared to the groundplane, which is expressed as

$$\mu = \frac{R_{\mathrm{s,c}} g_{\mathrm{c}}}{R_{\mathrm{s,c}} g_{\mathrm{c}} + R_{\mathrm{s,g}} g_{\mathrm{g}}}\,, \tag{4.1.1}$$

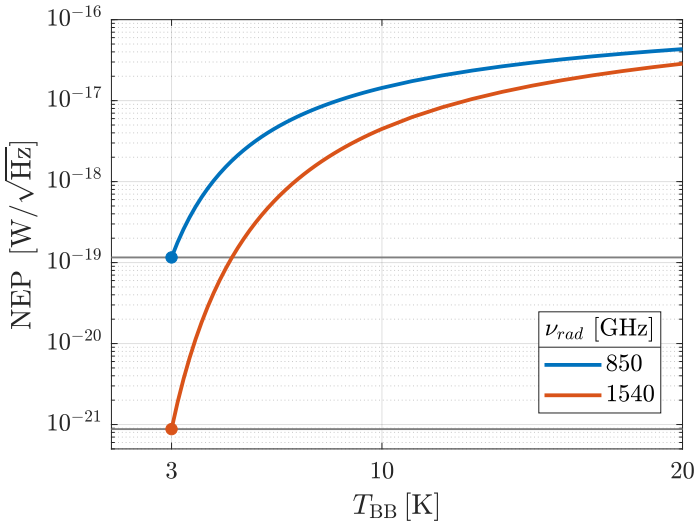

Figure 4.2 – The NEP due to photon noise including generation recombination noise (Eq. 2.4.5) as function of blackbody temperature for two frequencies. Blackbody radiation propagates through a filterstack providing a narrow bandpass around 850 or 1540 GHz. At the lowest blackbody temperature, $T_{\text{BB}} = 3\,\text{K}$, the $NEP_{\text{ph}}(850\,\text{GHz}) = 1.2 \times 10^{-19}\,\text{W}/\sqrt{\text{Hz}}$ while $NEP_{\text{ph}}(1540\,\text{GHz}) = 8.8 \times 10^{-22}\,\text{W}/\sqrt{\text{Hz}}$, low enough to reach the OST requirements.

where the geometry factors $g_{\text{c}}, g_{\text{g}}$ are calculated using Eqs. 2.3.8, 2.3.9. To give an explicit example, a CPW with a 2.2 µm gap, 1.6 µm line width and 55 nm is used and normal state resistivities ($\rho_{\text{N}} = R_{\text{s}}d$) as stated in Table 3.1. For hybrid MKIDs operating below 1.1 THz, the NbTiN sheet resistance $R_{\text{s,g,NbTiN}}$ is negligibly small compared to $R_{\text{s,c,Al}}$ and radiation is absorbed in the central line $\mu = 1$. However, at frequencies exceeding 1.1 THz, relatively large normal state resistivity of NbTiN would cause a significant reduction of the radiation absorption in the central line, causing a reduced quasiparticle density increase and thereby decreasing the responsivity. For $\nu_{\text{rad}} = 1.54\,\text{THz}$, the relative absorption in the central line reduces to $\mu = 0.14$. However, this can be increased if the groundplane material around the hybrid section is aluminium as well. For equal groundplane and strip thicknesses this yields $\mu = 0.80$, a large increase, owed to the low resistivity of aluminium compared to NbTiN.

In addition, the microwave response in the central line is increased because a larger fraction of the total inductance is contributed by kinetic inductance, $L_{\text{s,c}}g_{\text{c}}$. While the geometric inductance is unchangend (Eq. 2.3.4), the fraction of total kinetic inductance in the central line, $L_{\text{s,c}}g_{\text{c}}/(L_{\text{s,c}}g_{\text{c}} + L_{\text{s,g}}g_{\text{g}})$, is 25% larger for Al-Al hybrid section compared to the NbTiN-Al hybrid section. Thus, to absorb most of the 1.54 THz radiation in the cental hybrid line, the groundplane of the hybrid section should be made of aluminium as well.

A drawback is that, unlike the hybrid MKID as shown in Fig. 2.13, the antenna cannot be placed at the end of the resonator where the Al line is shorted to the NbTiN groundplane. To ensure radiation absorption in the Al line, the antenna is placed in the center of the hybrid section as shown in Fig. 4.4. Consequently, the total hybrid length is twice the minimum length required to absorb radiation.

4.1.2 Substrate protection

As previously mentioned, by using silicon instead of the conventional sapphire substrate, higher resistivities of aluminium line are experimentally obtained. This allows for shorter hybrid lengths and thus a decrease in active volume. However, short quasiparticle recombination times are observed for hybrid MKIDs on silicon, possibly related to substrate roughening during the fabrication process. Additionally, a low device yield is obtained due to issues with the aluminium etch, caused by an enhanced etch at the NbTiN-Si interface [37] (see Fig. 2.17). This can be prevented using an isolating substrate in stead of a semiconducting substrate. To prevent these 2 issues, the aluminium section of the MKID is fabricated on a 0.5 µm thick SiN layer,

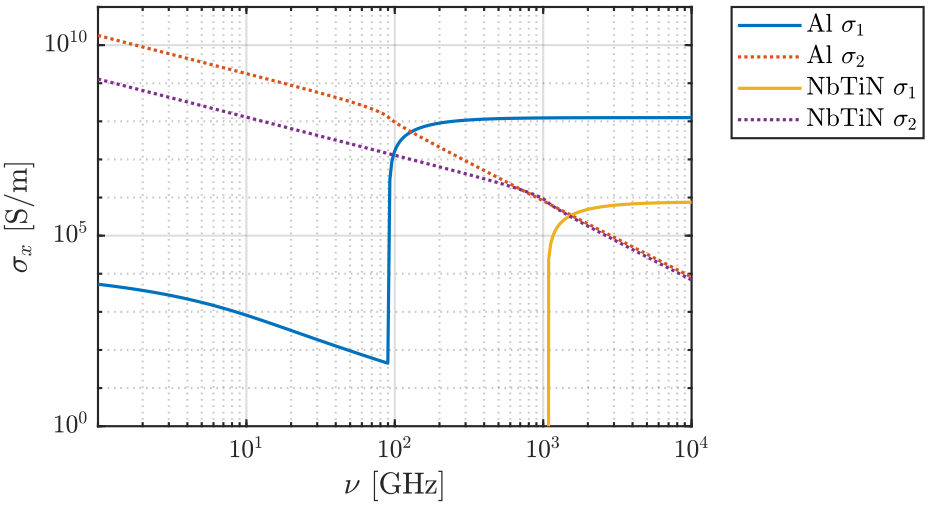

Figure 4.3 – Complex conductivity of Al and NbTiN at $T = T_c^{\mathrm{Al}}/8$, calculated using the Mattis-Bardeen integrals (Eqs. 2.2.2, 2.2.3). In between the gap frequencies $0.09 < \nu_{\mathrm{rad}} < 1.1\,\mathrm{THz}$, only aluminium acts as a resistive material. Created quasiparticles are confined to the aluminium because $\Delta_{\mathrm{Al}} < \Delta_{\mathrm{NbTiN}}$. At frequencies exceeding $\Delta_{\mathrm{NbTiN}}/h = 1.1\,\mathrm{THz}$, NbTiN is resistive as well, reducing the relative absorption in the hybrid line.

PECVD deposited on the substrate, prior to all other fabrication steps. Additionally, a resist mask is used to protect the SiN surface during the etch of the NbTiN, to prevent surface roughening. In the fabrication process, this extra layer is deposited before the NbTiN is deposited, as to protect the Si substrate at the hybrid section during the etching process.

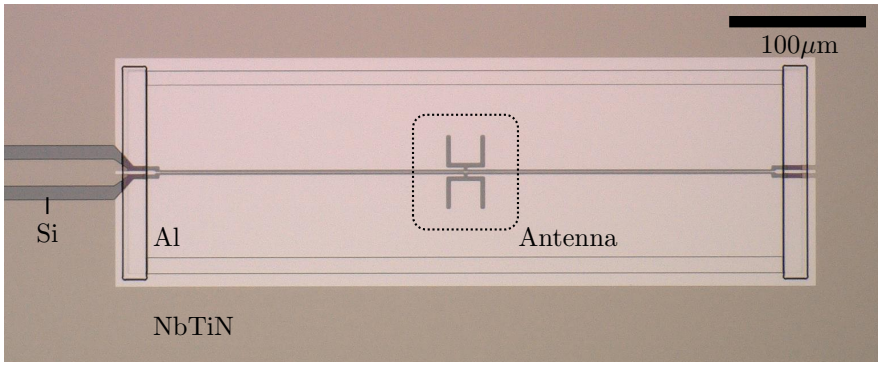

Figure 4.4 – Micrograph of the hybrid section (light area) of an MKID fabricated for this project. Both the central line and immediately surrounding groundplane are aluminium. To ensure radiation absorption in the aluminium line, the H-band antenna is located halfway while the hybrid length is twice the minimum length. The wide NbTiN CPW section of the resonator is seen on the left side.

4.2 What is the minimum hybrid line length?

In this section, the hybrid length is calculated from the requirement that a specified amount of the pair-breaking radiation should be absorbed. To do so, simulations were done of THz radiation absorption in a CPW structure using Sonnet® simulation software as to acquire the signal attenuation (dB/mm) for a specific CPW geometry. Based on these results, the minimum line length is retrieved as function of sheet resistance. Then, the aluminium sheet resistance is related to the layer thickness, by which all CPW geometry requirements are known.

4.2.1 Simulations of CPW signal transmission

The simulations of the signal transmission were done using Sonnet® simulation software, an electromagnetics analysis tool which uses surface meshing techniques to solve Maxwell's equations for planar structures, such as a hybrid MKID. To this end, a CPW structure is defined for which the signal transmission is simulated in a frequency band around 1.54 THz for various sheet resistances and various gap and line widths. The absolute transmission $|S_{21}|$ and reflection $|S_{11}|$ parameters between ports 1 and 2 are calculated from which the attenuation is retrieved. An example of a piece of CPW including the simulated current density is shown in Fig. 4.5. Because the structure is defined within a box of finite size, care has to be taken to avoid

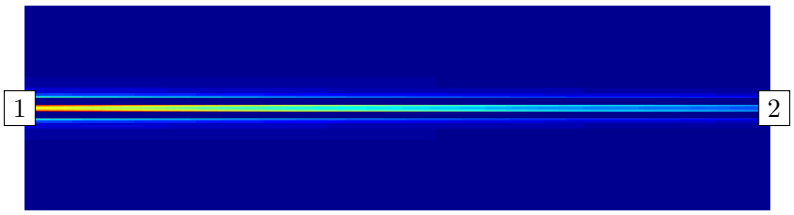

Figure 4.5 – Example of a current density as obtained from Sonnet® Simulations in calculating the transmission between port 1 and 2 of a 1-1-1 µm CPW of length 110 µm and total width 30 µm.

resonant behaviour, so-called box resonances, in the targeted frequency range. Resonances appear as sharp peaks in the S-parameters, making the simulation useless. To illustrate this, the S-parameters for the CPW structure as in Fig. 4.5 are simulated using a large frequency range, as shown in 4.6. The sharp peaks around 1200, 1800 and 2000 GHz indicate resonant behaviour outside the targeted frequency range of 1500 − 1600 GHz.

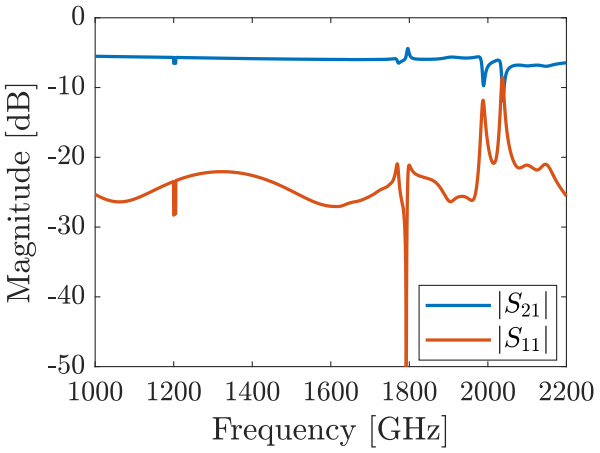

Figure 4.6 – Resonances due to the limited box size in which the CPW structure is defined. The S-parameters are shown for a large frequency range using a 1-1-1 µm CPW of length 110 µm and total width 30 µm.

The S-parameters as obtained for a 110 µm long CPW with a gap and line width of 1 µm is shown in Fig. 4.7 for various sheet resistances. The magnitude of the complex transmission $|S_{21}|$ (solid lines) is constant within the limited frequency range of 1.5 − 1.6 THz. Note the low reflection coefficients $|S_{11}|$ (dotted lines), which are below −20 dB. From this simulation, the signal attenuation (in dB/mm) is obtained as to calculate

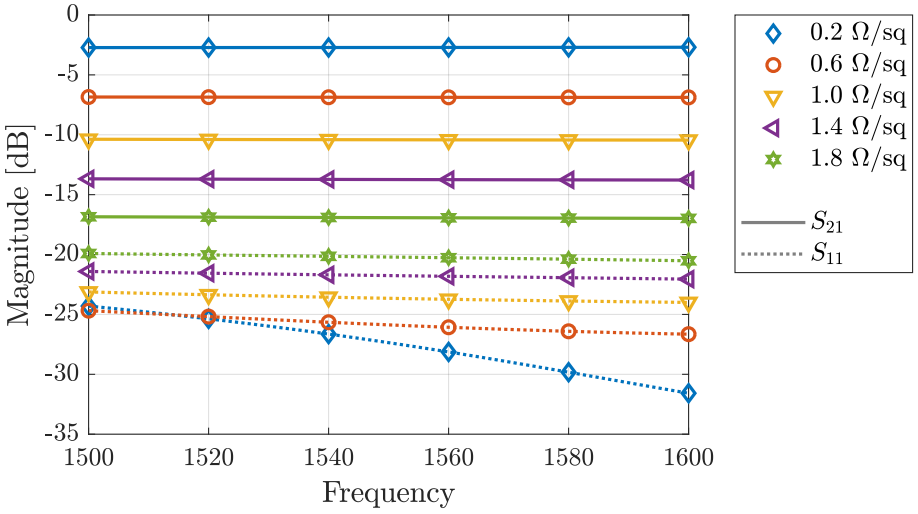

Figure 4.7 – Simulated signal transmission $|S_{21}|$ in dB of a 110 µm long 1-1-1 CPW (solid lines) for various sheet resistances as a function frequency using Sonnet simulations. The impedance is $Z_0 = 67\,\Omega$ such that the reflection coefficients $|S_{11}|$ at the input port (dotted lines) are below $-20\,\mathrm{dB}$

the actual hybrid length needed to ensure a specified amount of radiation absorption. Namely, the length corresponding to a total attenuation −15 dB, so that > 95% of the pair-breaking radiation is absorbed. This is presented in Fig. 4.8 for three CPW geometries, where the minimum line length is graphed as a function of sheet resistance. The last parameter left to fully specify the CPW dimensions is the layer thickness.

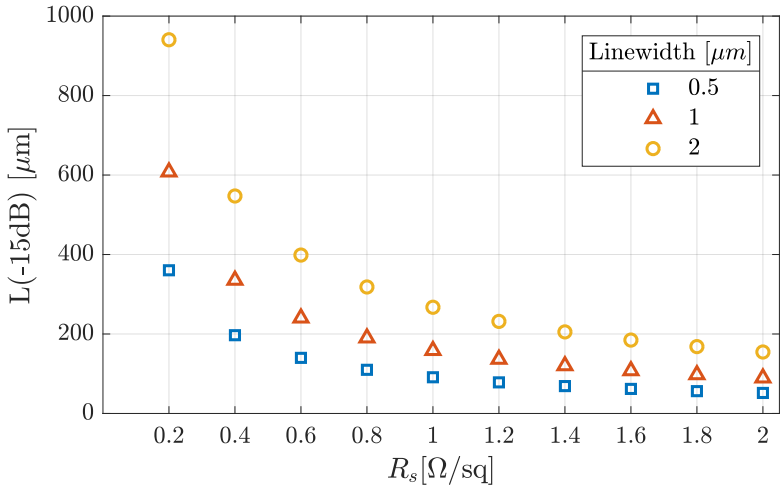

Figure 4.8 – Length at which the signal ($\nu = 1540\,\mathrm{GHz}$) is attenuated by −15dB for three different linewidths as a function of sheet resistance R_s. The gapwidth is equal to the linewidth.

The sheet resistance and thickness are related to the bulk resistivity as $\rho_N = R_s d$. However, for thin films, the resistivity is not necessarily constant with thickness. If the electron mean free path ℓ_e is greater than half the film thickness, surface scattering of electrons increases the resistivity. Based on a model that includes this surface scattering as described in [44], the thin film normal state resistivity ρ_N is calculated as follows

$$\rho_N = \frac{\rho_0}{k(1 - \ln k)} \quad \text{where} \quad k = \frac{d}{2\ell_0}\,, \tag{4.2.1}$$

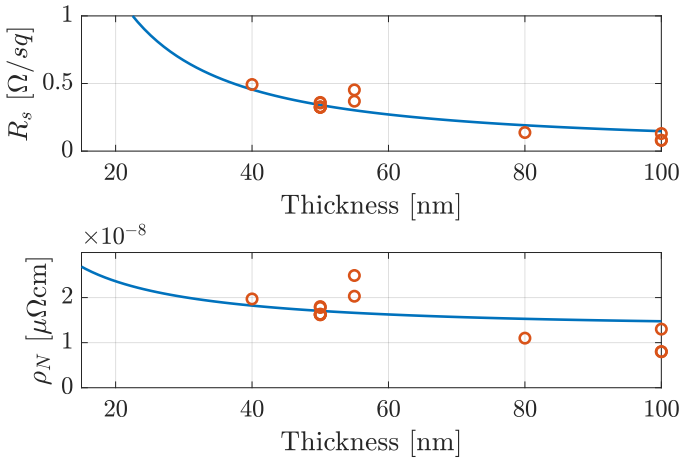

Figure 4.9 – Sheet resistance R_s (top) and normal state resistivity ρ_N (down) as function of aluminium line thickness on a silicon substrate. Given a certain R_s, the corresponding line thickness d and resistivity ρ_N can be inferred. Measurement data of previous fabrications are shown as well [36].

with ρ_0 the bulk resistivity, d the film thickness and ℓ_0 the (bulk) mean free path. Figure 4.9 shows the relation between sheet resistance, resistivity and film thickness fitted to previously done measurements for aluminium on silicon [36]. This is used to acquire ρ_N and d from the Sonnet® simulations.
Given the above results, an estimate of the generation-recombination noise limited sensitivity can be made based on realistic device dimensions.

For example, a sheet resistance $R_s = 1.0\,\Omega/\square$ and 1 µm line width gives a minimum length of 160 µm

Table 4.1 – Typical material values for Al and NbTiN. Note the variation in the Al parameters. The normal state resistivity ρ_N and film thickness d are related to the sheet resistance as $\rho_N = R_s d$. Due to its short quasiparticle recombination time, NbTiN cannot function as the active volume of the hybrid.

Material	T_c (K)	Δ (µeV)	ρ_N ($\mu\Omega$cm)	d (nm)	τ_0 (ns)	$\tau_{qp,max}$ (ms)
Al [18]	1.11	168	0.8	40	458	2.2
Al [40]	1.24	188	2.2	50	303	3.5
Al (Ch. 5)	1.31	199	1.52	40		
NbTiN	14 [39]	2100	130	300		1×10^{-6} [45]

and an aluminium thickness of 22 nm. If the recombination time is set to $\tau_{qp} = 3$ ms and $\eta_{pb} = 0.4$, the $NEP_{GR} = 3.3 \times 10^{-20}\,\mathrm{W}/\sqrt{\mathrm{Hz}}$.

4.3 Device Design

In this section I describe the design of the MKIDs with the smallest volume given by the constraints of the device fabrication that is based on optical contact lithography.

Based on the model described in the previous chapter, the MKID dimensions are set such that the hybrid volume is minimised, while making sure that the THz radiation is absorbed in the hybrid section and that the TLS noise is sufficiently low to be able to see generation-recombination noise. First, a description is given of the choices made that led to the chip design, which includes 7 hybrid MKIDs and 3 blind resonators. Then, an overview of the layout is given in which the purpose of every material layer is shortly discussed, alongside an overview of the design parameters of the MKIDs on the chip. The section concludes with the expected performance for the first fabricated batch. Based on the model described in the previous chapter, the expected power spectral density and NEP are graphed.

4.3.1 Hybrid MKID design

The chip design contains 7 hybrid MKIDs, all optimised for 1.54 THz radiation coupling, and readout with a single throughline. One such an MKID is shown in Fig. 4.10. The antenna was designed by J. Bueno, and optimised for 1.54 THz radiation coupling. The dimensions of these MKIDs are determined from the following considerations:

1. For all hybrid MKIDs, the CPW gap and line width of the aluminium section are set close to the minimum feasible width when using optical lithography, which is 1 µm.
2. The Al length is set to absorb the radiation coupled to the antenna to a level of -15 dB at 1.54 THz the required length depends on the Al sheet resistance and the fixed CPW dimensions. Hence, given a target sheet resistance, the corresponding Al length follows from the simulation results (Fig. 4.8) and the layer thickness follows from the relation between layer thickness and sheet resistance (Fig. 4.9).
3. Three different realistic R_s are chosen, compatible with different fabrication runs for varying aluminium thicknesses. One chip design is made for each R_s. This is shown in Table 4.2 for the three sheet resistances.
4. A single chip design includes 7 hybrid antenna-coupled MKIDs with varying Al lengths. To optimise both the fraction of absorbed power, and the device sensitivity, three different hybrid lengths are chosen such that $\ell_\mathrm{Hyb} = \ell_\mathrm{min}(R_\mathrm{s}) \cdot [1,\ ^2/_3,\ ^1/_2]$.
5. The antenna-coupled MKIDs are positioned such as to match the 1.6 mm lens spacing of the available lens array, which is hexagonally packed.
6. All resonators have distinct frequencies which lie within the $4-7$ GHz range, coupled to single readout line to allow frequency domain multiplexed readout. Combined with a specific aluminium length, this sets the total resonator length and thereby the wide NbTiN length, using the expression for a $\lambda/4$ resonance, Eq. 2.3.1.

MKID that are closely packed in the spatial and frequency domain have been shown to couple capacitively or inductively to surrounding resonators [46]. This unwanted coupling or cross talk results in a collective response of two or more resonators but is exponentially suppressed with MKID separation [46].

Importantly, crosstalk is suppressed by connecting the groundplanes on either side of the throughline (readout line)[46]. This is implemented using two throughline bridges near each MKID [5], made of aluminium isolated from the readout line by polyamide.

For the hexagonally packed MKIDs in this design, with a 1.6 mm pixel spacing and $\mathrm{d}F_0 > 50$ MHz, cross talk should not be a concern, given the large frequency separation and the presence of the throughline bridges. Moreover, the large frequency spacing prevents a possible overlap of resonances. Because resonance frequencies are bound to deviate from their target values due to local variations in material properties such as layer thickness and resistivity [5].

Furthermore, three blind resonators are added to be able to measure the noise properties of the NbTiN and the Al. MKID in large arrays have been shown to exhibit cross coupling, an unwanted effect resulting in

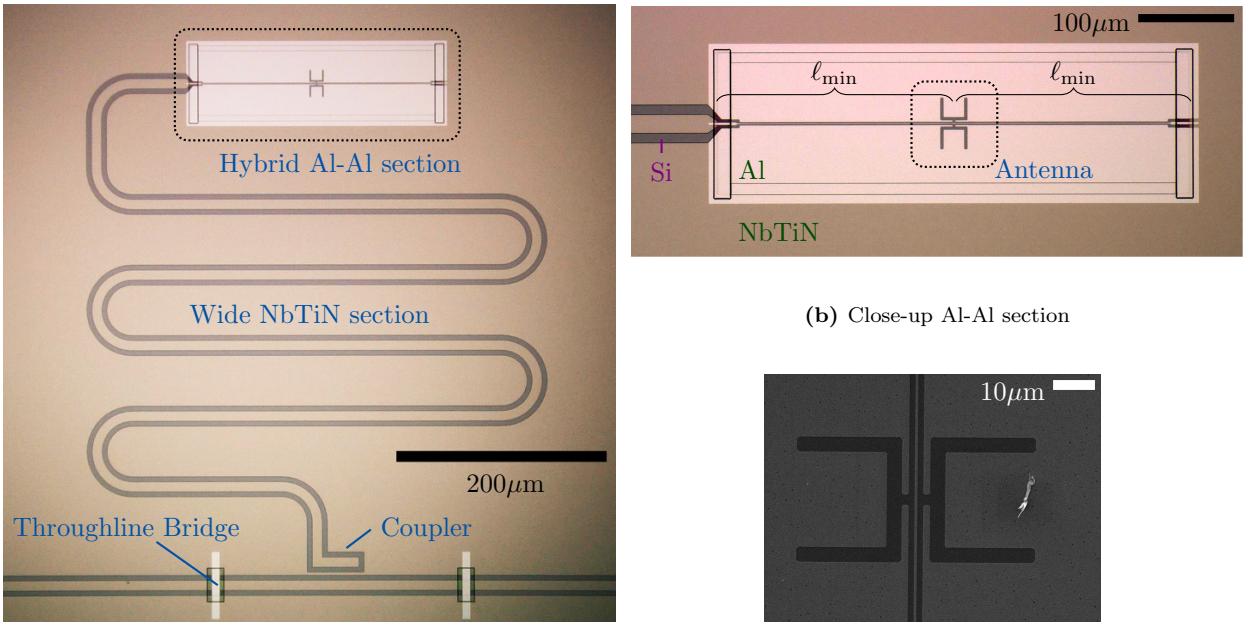

(a) Full MKID

(b) Close-up Al-Al section

(c) Close-up antenna

Figure 4.10 – **(a)** Micrograph of a single MKID capacitively coupled to the readout line, with throughline (readout line) bridges on either side. To fit the long ($\sim 5\,\mathrm{mm}$) NbTiN section in between the throughline and the Al-Al section, it has a snake-like folded shape. **(b)** Close-up of the Al-Al section, its length twice the minimum length $\ell_{\min}$. The Al line connected to the wide NbTiN section on the left and the NbTiN groundplane on the right side. **(c)** SEM image of the twin-slot antenna, located halfway the Al-Al section and optimised to couple 1.54 THz radiation into the CPW. Antenna design credit by J. Bueno.

4.3.2 Blind Resonators

To check the TLS noise properties of the groundplane and resonator materials, three blind (without antenna) resonators are added to the chip. One resonator entirely made of NbTiN and two resonators with a long Al section. The two blind Al resonators do have a NbTiN coupler, but the Al part is long enough such that the TLS noise of the Al section dominates over the wide NbTiN part. Two lengths are chosen to be able to check the position dependence of TLS contributions along the resonator, namely the semi-empirical E^3 dependence of TLS noise [35]. The lengths are set such that the Al section has a dominant TLS contribution, 0.98 of the total TLS noise, and one in between the NbTiN and Al dominated regions, at a fractional $S_{\mathrm{TLS}}^{\mathrm{Al}} = 0.5$. This is shown in Fig. 4.11 for the 1-1-1 µm Al CPW and a 10-20-10 µm NbTiN CPW.

Table 4.2 – Summary of chip design with a corresponding NEP_{GR} calculation. The target sheet resistance R_s is set, from which the minimum length ℓ_{min} and aluminium layer thickness d are obtained (see section 4.2). The NEP_{GR} calculation assumes $\tau_0 = 458$ ns, $\tau_{qp} = 3$ ms, $T_c^{Al} = 1.28$ K and linewidth $S = 0.8$ µm due to an expected aluminium overetch.

	R_s [Ω/□]	d [nm]	ℓ_{min} [µm]	$NEP(\ell_{min})$ $\times 10^{-20}$[W/$\sqrt{\text{Hz}}$]	$NEP(2/3\ell_{min})$ $\times 10^{-20}$[W/$\sqrt{\text{Hz}}$]	$NEP(1/2\ell_{min})$ $\times 10^{-20}$[W/$\sqrt{\text{Hz}}$]
Chip 1	0.35	49	400	10.9	8.9	7.7
Chip 2	0.6	33	250	7.1	5.8	5.0
Chip 3	1.0	22	160	4.7	3.8	3.3

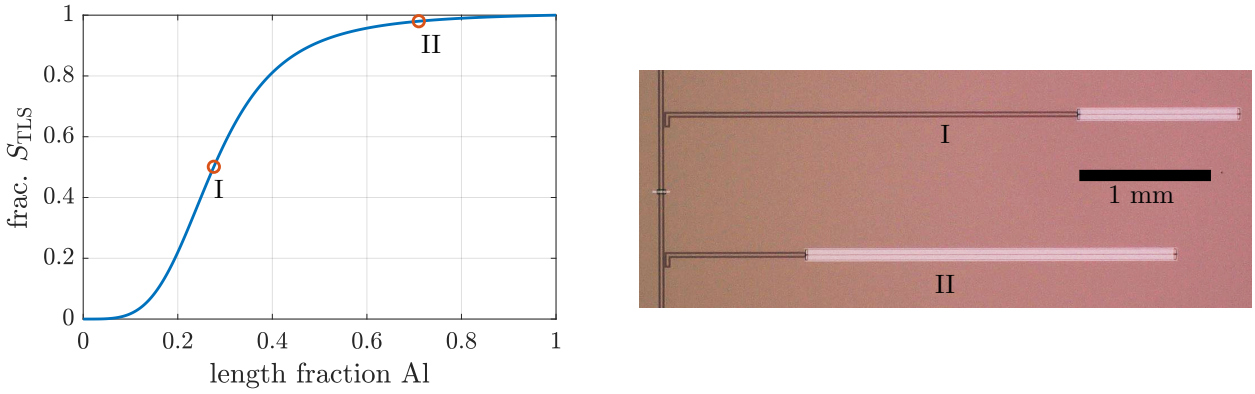

Figure 4.11 – **(left)** TLS noise contribution of the Al section with respect to the total TLS noise of the resonator as function of the fractional Al length. Sheet resistance and layer thickness for Chip 1 are used (see Table 4.2) with a 1-1-1 µm Al CPW and a 10-20-10 µm NbTiN CPW. The red dots indicate the length fraction at which the TLS contribution of the Al section is 0.5 and 0.98 times the total TLS noise. True lengths are obtained from solving Eq. 2.3.1 after setting the resonance frequency. **(right)** Micrograph of the two blind resonators. The top one has a shorter Al section and corresponds to the 0.5 fractional TLS noise, the resonator below corresponds to the 0.98 fractional TLS noise.

4.4 Layout and Design Details

4.4.1 Al-Al section

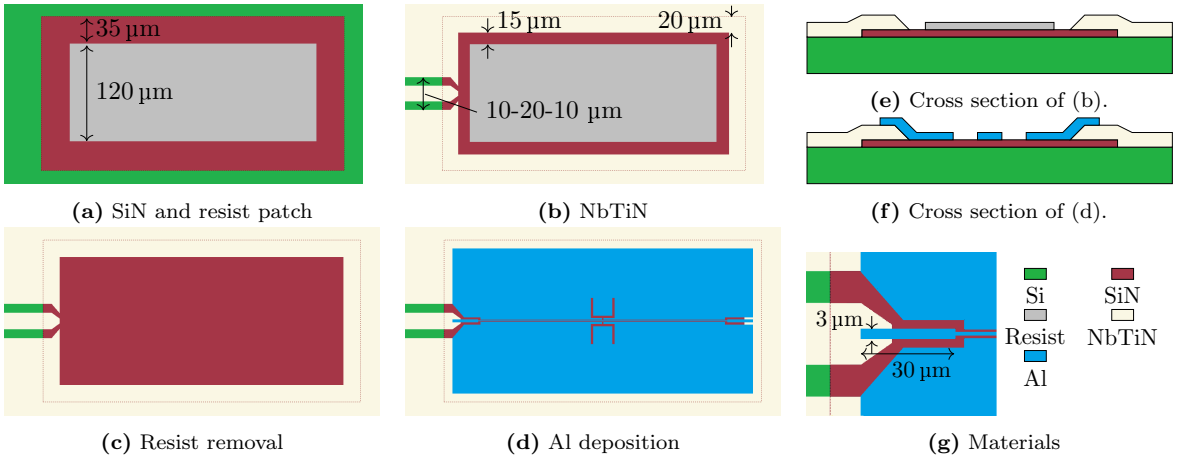

(a) SiN and resist patch **(b)** NbTiN **(e)** Cross section of (b). **(f)** Cross section of (d).

(c) Resist removal **(d)** Al deposition **(g)** Materials

Figure 4.12 – Illustration of the Al section of the MKIDs. In the design, only the Al and NbTiN length of each resonator are varied, the widths and layer order as shown here are the same for each MKID. This figure includes the order in which the layers are deposited **(a-d)**, two crossections (not to scale) to show the overlap of the different layers **(e-f)** and a close-up of the resonator transition from NbTiN to Al **(g)**. The legend in **(g)** shows the material-color combinations.

The Al-Al section consists of multiple layers, the top and side view of which are illustrated in Fig. 4.12. The dimensions and the order of deposition of these layers are explained with a focus on the design while The details of the fabrication process itself are given in the appendix.

Prior to all other fabrication steps, a SiN patch (Fig. 4.12a) is etched into a SiN layer that was deposited using plasma-enhanched chemical vapor desposition (PECVD) on the entire Si wafer. This layer prevents an enhanced aluminium etch at the NbTiN-Si interface as argued in section 2.6.4 and covers a large area as the NbTiN should overlap the SiN patch (see cross section, Fig. 4.12c). Additionally, a temporal resist patch (gray) protects the SiN from surface roughening during the NbTiN etch, shown in Fig. 4.12b and corresponding crossection Fig. 4.12c. The NbTiN layer is then added, partially overlapping the SiN, but separated from the resist patch, as it is removed in the next step (Fig. 4.12e).

Around the NbTiN-Al transition, all layers are separated by 10 µm; wide enough to allow at least 5 µm overlap or separation, taking into account possible alignment errors of ~ 2 µm.

The Al section is deposited last, (Fig. 4.12f), connected to the wide NbTiN resonator on one end and the NbTiN groundplane on the other. Shown in the crosssection (Fig. 4.12d), the Al groundplane overlaps the surrounding NbTiN. The zoom-in of the NbTiN-Al resonator transition shows a widened Al line connected to the wide NbTiN, Fig. 4.12g. This widened end of the Al section is chosen to prevent possible line discontinuities due to the large height differences at the transition from protected SiN via the etched SiN to the NbTiN (thickness NbTiN is 300 nm, thickness Al only tens of nanometers).

4.4.2 Absorbing mesh

One last optimisation originates from the fact that not all radiation incident on a single lens-antenna combination is fully coupled to a single MKID. Instead, a fraction of the radiation is reflected and scattered inside the substrate of the chip [47]. To absorb this stray radiation, a meshing layer is introduced on the reverse side of the Si chip [47], as indicated in Fig. 4.13 by the red line. To leave the *primary* radiation focused by the lenses unaffected, the absorbing layer has a circular aperture of $R = 0.6$ mm around the antenna positions [5].

Additionally, this layer can efficiently reduce effects from high energy cosmic rays impinging on the detector which causes dead time and data loss [48] (and is therefore especially relevant for space-based observatories).

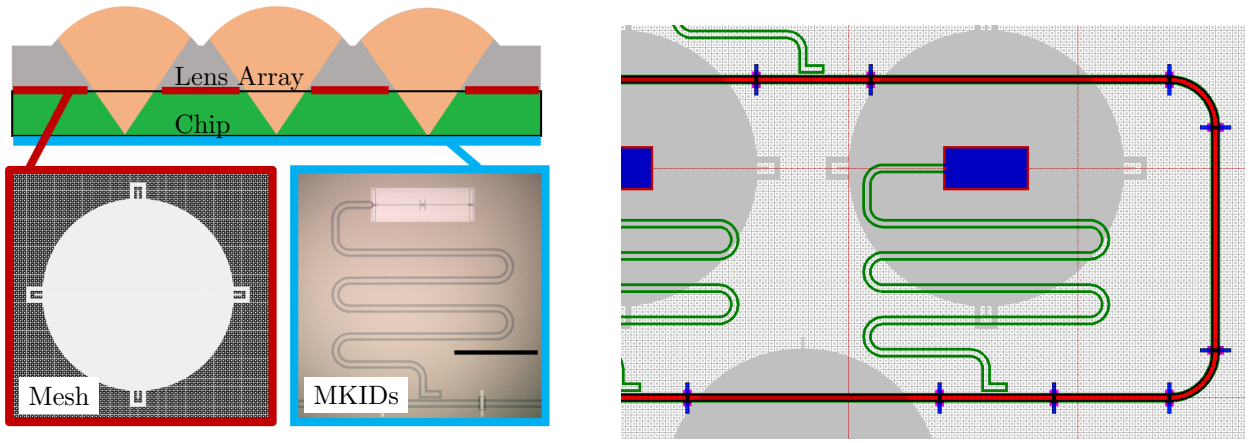

Figure 4.13 – **(left)** Illustration of the lens array and chip. The chip is facing downwards with the absorbing mesh facing the lens array. **(right)** Illustration of the hybrid MKID including the absorbing mesh layer at the reverse side (grey) of the chip and the Al-Polyamide throughline bridges.

Because high energy phonons in a superconductor are quickly downconverted to the gap energy, the absorbing layer is made of a material with critical temperature lower than the Al of the MKIDs [49, 50]. This way, cosmic ray impacts still create high energy phonons but they are quickly reduced to energies $E < 2\Delta_{\mathrm{AL}}$ and cannot break Cooper pairs in the Al.

An overview of the total chip design including all 10 resonators is shown in Fig. 4.14

4.5 Expected Performance

In this section I show the expected performance of the designed MKIDs, based on the model described in section 3.1 and the parameters of Chip 2, as shown in Table 4.3. Then, the noise spectrum and NEP is calculated for KID 1, using the measured DC parameters as given in Table 6.2. Note that the layer thickness of the fabricated chip is 40 nm, in between the target thickness of Chip 1 and 2.

Table 4.3 – Overview of MKID parameters for chip 2, designed for a sheet resistance $R_s = 0.60\,\Omega/\square$ and 33 nm layer thickness.

KID	F_0 (GHz)	ℓ_{Al} (µm)	ℓ_{NbTiN} (µm)	ℓ_{tot} (µm)	Q_c
1	4.28	250	6430	5203	1.76×10^5
2	4.47	250	6137	5400	1.62×10^5
3	4.63	333	5761	5578	1.51×10^5
4	4.85	250	5620	5840	1.37×10^5
5	5.00	333	5285	6259	1.30×10^5
6	5.19	500	4861	6552	1.20×10^5
7	5.27	500	4665	6054	1.17×10^5
8	5.33	1225	3208	4433	1.14×10^5
9	5.05	2803	1147	3949	1.27×10^5
10	6.01	-	4903	4903	3.35×10^4

KID	ℓ_c (µm)	CPW (NbTiN) (µm)
1-9	93	10-20-10
10	245	10-6-10

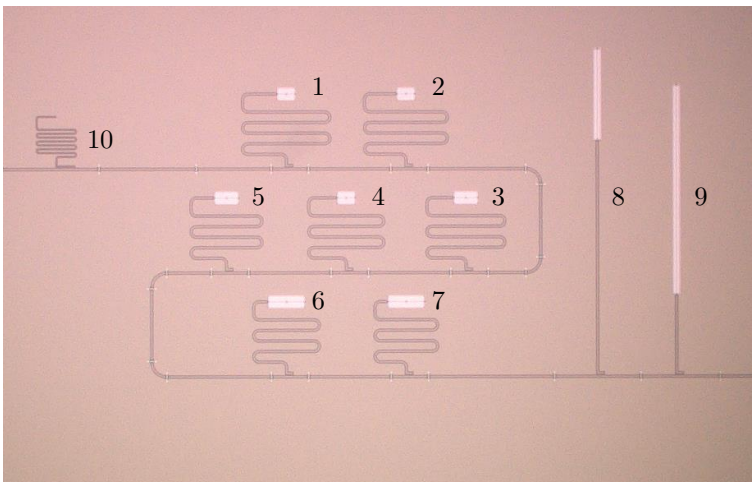

Figure 4.14 – Overview of chip 2, designed for $R_s = 0.60\,\Omega/\square$. The numbering of the resonators correspond to the one used in the parameter overview.

4.5.1 Expected TLS noise

Because TLS noise is material dependent, the use of a SiN layer at the Al-Al section introduces 10 dB higher noise compared to the Al on Si (see Fig. 2.11). However still, the main contribution of TLS noise is due to the wide NbTiN section because the Al section is very short.

The TLS noise is shown for all 7 hybrid MKIDs together with the reference noise levels of Gao *et al* (see Table 2.1 and Fig. 2.11). The slight variation in noise level results from the three different aluminium lengths, also indicated in the legend, and variation in Q_c over frequency as given Table 4.3 and discussed in Appendix A.1.

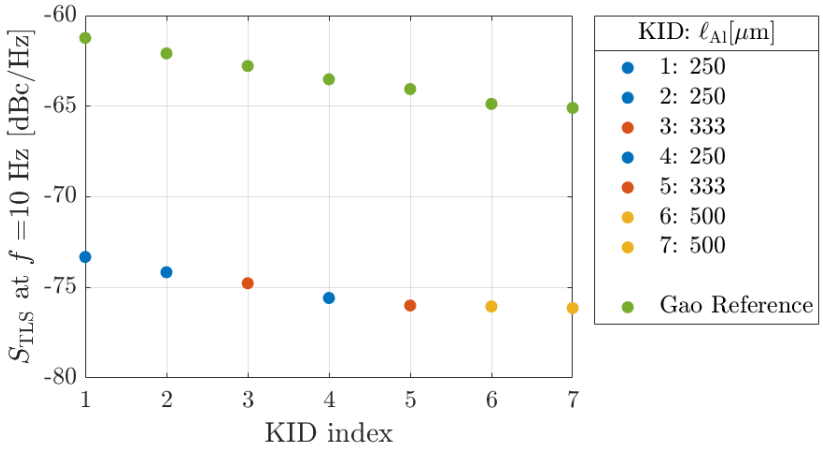

Figure 4.15 – Phase noise expected for TLS noise contributions at $f = 10$ Hz and $P_{\text{int}} = -50$ dBm for Chip 2 including the Gao reference values (green), using coupling quality factors given in Table 4.3. Apart from the Q scaling, the small variations in noise levels are due to the three different aluminium lengths, distinguished by the coloured markers.

4.5.2 Expected NEP and PSD

The expected power spectral density is calculated for KID 1, with an Al length of 250 µm, with a low internal power $P_{\text{int}} = -50$ dBm and a quasiparticle lifetime $\tau_{\text{qp}} = 3$ ms. An expected overetch of 0.1 µm of the aluminium line is taken into account such that $S = 0.8$ µm and $W = 1.2$ µm.

Although TLS noise is expected to be high due to the SiN and the narrow Al CPW, the decrease in active volume drastically increases the responsivity and hence the total phase noise, as shown in Fig. 4.16a. This model will be used to compare the calculations with the chip measurements and the experimentally obtained material parameters in the next chapter.

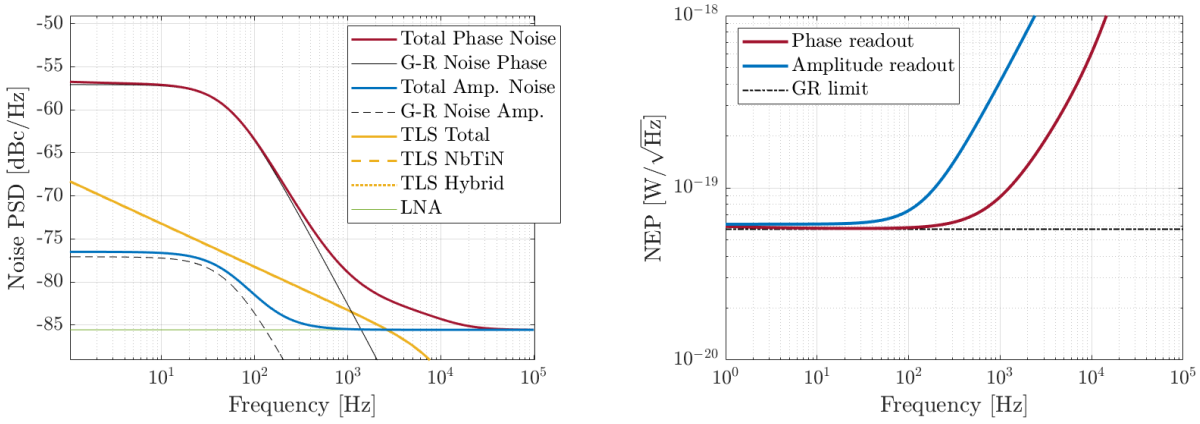

Power Spectral Density

Noise Equivalent Power

Figure 4.16 – Power Spectral Density including the modelled phase, amplitude, TLS and readout (LNA) noise contributions for KID 1 with $\ell_{\text{al}} = 250$ µm (see Table 4.3). For this calculation, $P_{\text{int}} = -50$ dBm, $\tau_{\text{qp}} = 3$ ms and the DC measurements as given in Table 6.2. The total phase noise is the sum of $S_{\theta,\text{GR}}, S_{\text{LNA}}$ and S_{TLS}. The total amplitude noise is the sum of $S_{\text{A,GR}}$ and S_{LNA}.

Chapter 5

Measurements and Setup

In this chapter, the experimental setup and measurement procedures are described. The measurements were conducted at SRON, Utrecht, using the same cryogenic setup as used by P. de Visser [22]. Hence, this section largely follows the detailed description as found in ([22], Chapter 3).

5.1 Cryogenic Setup

The cryostat is a pulse tube pre-cooled Adiabatic Demagnetisation Refrigerator (ADR). It consists of several temperature stages: the pulse tube cooler has a 50 K stage and a 3.2 K base temperature.

The next stages use the ADR, a cooling mechanism based on the randomisation of aligned spins in a magnetised paramagnet, which corresponds to a low entropy state. By thermally connecting the paramagnet to the thermally isolated cooling stage, thermal vibrations are absorbed and randomises the spins, thus increasing the entropy and reducing the temperature of the paramagnet and its surroundings (adiabatic demagnetisation).

The two paramagnetic materials in the ADR are a Gadolinium Gallium Garnet (GGG) crystal, which is used for the 500 mK stage, and a Ferric Ammonium Alum (FAA) salt pill, which is used for lowest temperature stage (down to 30 mK). For the MKID measurements, an operation temperature of around 120 mK is sufficiently low and also extends time before a recharge of the ADR.

To shield the sample from unwanted magnetic fields, an outer Cryperm shield and an inner superconducting lead-tin coated shield are used.

A box-in-a-box configuration [51] is used to shield the sample from any stray light coming from the 3 K stage, as illustrated in Fig. 5.3. Both boxes are made of gold plated copper. To absorb any stray light, the inner side of the boxes are covered with a layer of carbon loaded epoxy. The MKID is readout signal travels via two filtered coax cables that enter via the outer box and are designed to transmit in the $3-8$ GHz range but absorb stray light at frequencies exceeding the Al gap frequency $\nu_{\mathrm{gap,Al}} \simeq 90$ GHz [51].

5.2 Readout System

To perform any measurements on the MKIDs, a microwave signal should be generated, send through the sample and readout. For this purpose, a homodyne readout system is used as shown in the simplified schematic overview of Fig. 5.1. A microwave generator (Agilent E8257D) creates the desired signal after which the splitter sends one part to the IQ-mixer (Miteq IRM0218LC1Q) and the other part into the cryostat, through the sample and to the IQ-mixer with the necessary amplification. At each temperature stage, the signal is attenuated to reduce thermal noise, as described in detail by P. de Visser [22]. After the sample, the signal is amplified with a high-electron-mobility transistor (HEMT) amplifier (CITCYO4-12A Wadefalk/Weinreb). The noise contribution of this amplifier (Eq. 2.4.10) is white and dominates the noise due to all readout electronics. Then, the signal is amplified at room temperature and mixed with the original signal in the IQ-mixer, where it is readout using an Analog-to-Digital Converter (ADC) which samples at 2 MHz and subsequently converted to phase and amplitude readout.

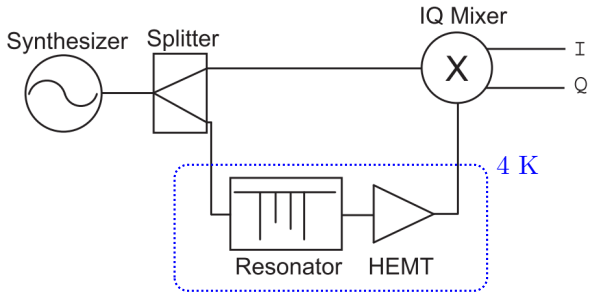

Figure 5.1 – Schematic overview of the microwave readout system. Picture from [16].

For a fast frequency sweep to locate the resonance dips, a Vector Network Analyser (VNA, Agilent PNA-L N5230A) is used instead. This device replaces then the room temperature electronics.

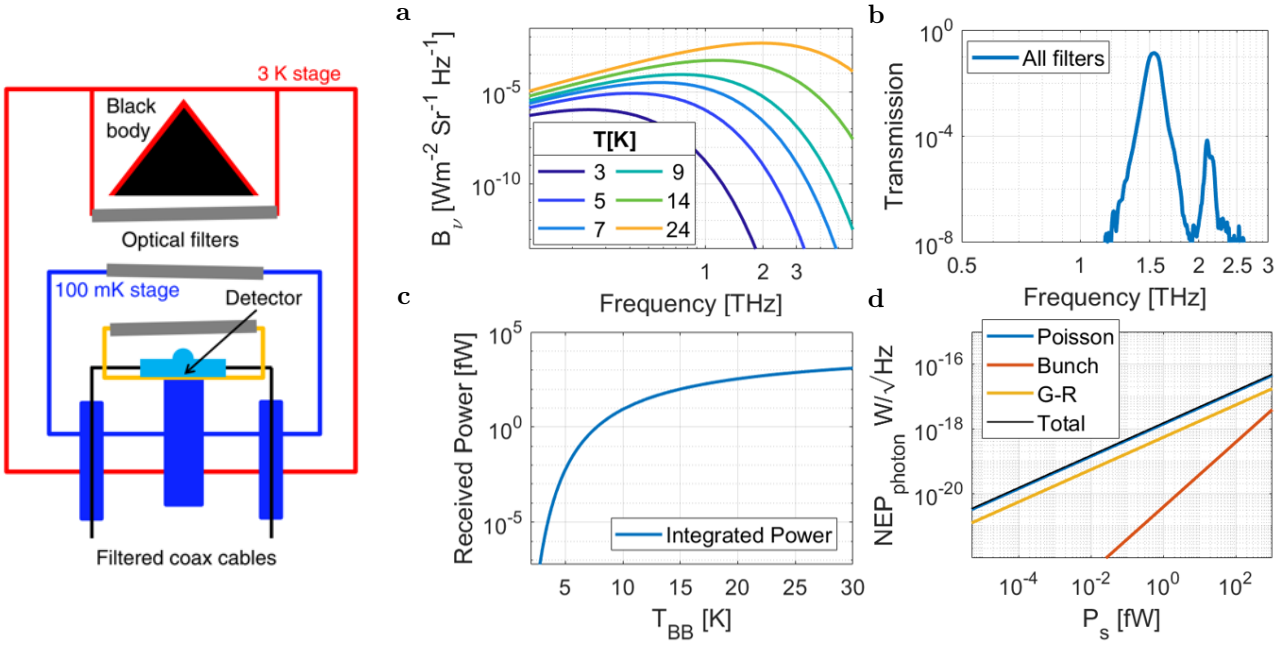

Figure 5.2 – (*left*) Illustration of the box-in-a-box configuration in the cryostat including the blackbody, optical filters, filtered coax cables and detector. Image taken from [40]. (*right*) Overview of the controlled detector irradiation by tuning the blackbody temperature. **(a)** Blackbody spectral brightness (B_ν [$\mathrm{Wm^{-2}Sr^{-1}Hz^{-1}}$]) curves within the relevant temperature range of $3-25$ K. **(b)** Transmission of the filterstack, which has a bandpass around 1.54 THz. **(c)** Radiation power arriving at the detector as function of blackbody temperature, obtained by integrating the Planck curve, filter transmission and optical throughput over frequency (Eq. 5.3.1). **(d)** NEP_{photon} as function of the power, obtained via Eq. 2.4.5 assuming the optical efficiency $\eta_{\mathrm{opt}} = 1$.

5.3 Optical System

The detector response and sensitivity to radiation are measured using a blackbody with a variable temperature as radiation source combined with several optical filters to filter out a narrow frequencyband around 1.54 THz. This setup is illustrated in Fig. 5.2. The blackbody temperature range is 3-25 K, the spectral brightness of the corresponding Planck curves are shown for several temperatures in Fig. 5.2a. The trans-

mission of the filterstack (F_ν) defines a narrow bandpass around $\nu = 1.54$ THz and is shown in the top right as a function of frequency. This allows to calculate the power arriving at the detector lens array as a function of the blackbody temperature (T_{BB}) via

$$P_{\mathrm{s}} = \frac{1}{2}\int B_\nu F_\nu \lambda^2 \mathrm{d}\nu\,, \tag{5.3.1}$$

with λ the wavelength, λ^2 the optical throughput [37] from the blackbody to the detector and the factor $1/2$ is incorporated because the antenna is single polarized. As a result, the setup allows the received power to be tuned over a large range, $10^{-6} - 10^{3}$ fW, as shown in 5.2c. Importantly, this implies $NEP_{\mathrm{photon}}(P_{\mathrm{s}})$ (Eq. 2.4.5, assuming $\eta_{\mathrm{opt}} = 1$) ranges up to sufficiently low values as to reach the OST detector sensitivity requirements, $\sim 10^{-20}$ W/$\sqrt{\mathrm{Hz}}$.

5.4 Measurement Procedure

This section explains in a general way how the experimental noise spectra, optical responsivity and NEP are obtained. The detailed measurement results are discussed in section X.
Any measurement starts by locating the resonance dips. To this end, a fast frequency sweep is performed using the VNA, measuring the complex transmission S_{21}. Then, to obtain the Power Spectral Density (PSD), a noise measurement is done by probing the resonators at their just determined resonance frequency and recording a time trace of the amplitude and phase response, as illustrated in Fig. 5.3. The PSD is calculated

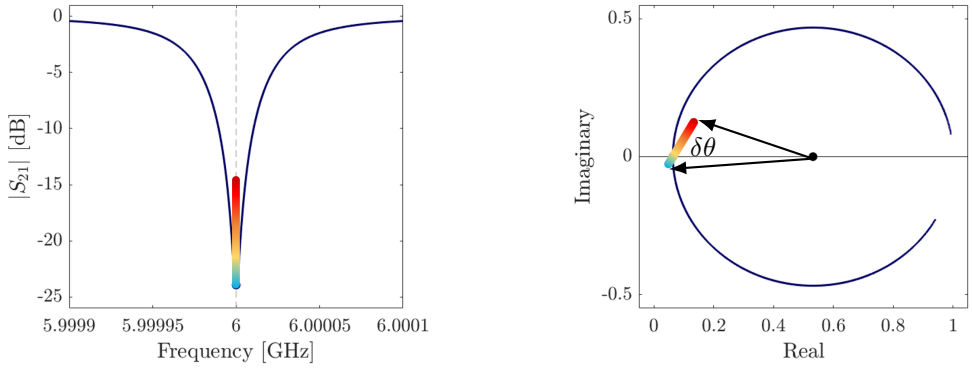

Figure 5.3 – Illustration of the response (*coloured line*) of a resonator probed at its resonance frequency. *(a)* in absolute transmission $|S_{21}|$ **(b)** The resonance circle in the IQ-diagram, the arrows indicate the phase response.

from the time domain data by taking the Fourier transform of the autocorrelation function of the response data. This is done using standard Fast Fourier Transform (FFT) algorithms.

The optical (phase) responsivity $\mathrm{d}\theta/\mathrm{d}P_{\mathrm{s}}$ is obtained by recording the response while varying the radiation power around a predefined value and fitting a linear curve to the data. For low radiation powers where the response is hardly visible, the power is swept upwards only, such as shown in Fig. 5.4b.

Now, the optical NEP can be calculated using Eq. 2.4.11, the measured noise spectra and the optical responsivity. This is shown in Fig. 5.4c for various absorbed powers, at a modulation frequency $f = 140$ Hz. The optical NEP saturates 3×10^{-19} W/$\sqrt{\mathrm{Hz}}$ up to $P_{\mathrm{abs}} \simeq 30$ aW, from where it transitions to a photon noise limited regime.

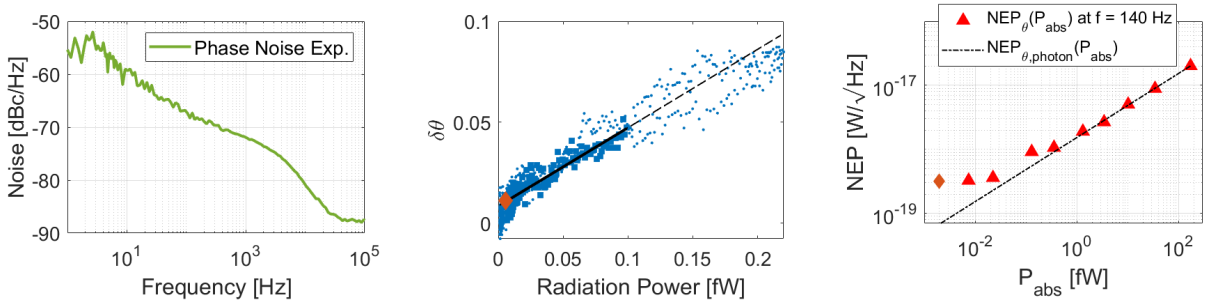

a: PSD **b:** Responsivity **c:** NEP

Figure 5.4 – Example of measurement results of KID 1 at a readout power $P_{\mathrm{read}} = -98$ dBm from which the optical NEP is calculated at various radiation powers. **(a)** The experimental PSD of the phase readout at a blackbody temperature $T_{\mathrm{BB}} = 5$ K. **(b)** The optical responsivity is determined by a linear fit to $\delta\theta$ versus P_{s}. The limited fitrange is indicated by the thick black line and datapoints. This example is at low radiation power, where the response is hardly visible. Therefore, the power is swept over higher values only. **(c)** The optical $NEP(P_{\mathrm{abs}})$ at a modulation frequency $f = 140$ Hz, including $NEP_{\mathrm{photon}}(P_{\mathrm{abs}})$ as obtained from the noise and responsivity measurement as shown in (a, b). The absorbed radiation power $P_{\mathrm{abs}} = \eta_{\mathrm{opt}} P_{\mathrm{s}}$. Note that the NEP saturates at around $3 \times 10^{-19}\,\mathrm{W}/\sqrt{\mathrm{Hz}}$ up to $P_{\mathrm{abs}} \simeq 30$ aW, from where it transitions to a photon noise limited regime.

Chapter 6

Experiments and Results

In this chapter, the measurements are presented together with the calculated noise spectra and NEP. After an initial model and measurement comparison, three individual measurements are presented considering TLS noise, temperature dependent quasiparticle lifetimes and a responsivity measurement. Again, the noise spectra are compared to a modified model after which the optical NEP is analysed.

6.1 Chip Inspection

Prior to the noise measurements, a first inspection of the chip is done by performing a frequency sweep using the VNA. This gives the location of the resonance frequencies and quality factors are readily obtained by fitting the resonance curves using Eqs 2.3.15, 2.3.16.

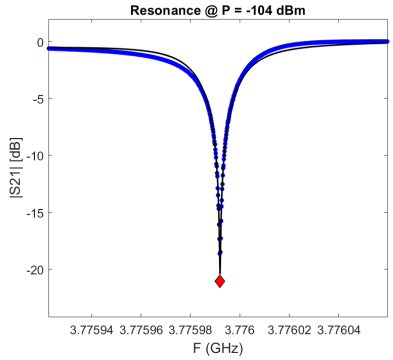

Figure 6.1 – Absolute transmission as function of frequency showing the resonance dip of KID 1. The measured $F_0 = 3.776$ GHz, $Q_c = 1.2 \times 10^5, Q_i = 1.2 \times 10^7$. This is lower than the expected coupling Q ($Q_c = 1.76 \times 10^5$), however, the resonator structure was not fully simulated.

The expected quality factors lie within a factor 2 of the experimental values. The coupling quality factor is lower, which could be due to the fact that the resonator was not fully simulated in Sonnet.

The measured Quality factors and resonance frequency are used as model input, because prior to the noise measurements, the resonance dips are already located by a frequency sweep. This automatically gives the experimental resonance frequency as well as the quality factors of each MKID, as shown in Fig. 6.1.

6.2 Ab Initio Model Comparison

In this section, the measured noise spectra are compared to an ab initio model calculation for both low ($T = 120$ mK) and high ($T = 270$ mK) temperatures.

6.2.1 Model Input

As input parameters for the calculated spectra I use the geometric dimensions of the MKIDs based on a SEM inspection. The input material parameters of Al and NbTiN (T_c, R_s) are obtained from the DC

Table 6.1 – Overview of the measured resonance frequencies and quality factors as obtained from the resonance dips after the first chip inspection.

KID	F_0 [GHz]	Q_c	Q_i	Q_l	P_{read} [dBm]
1	3.78	1.20×10^5	1.25×10^7	1.19×10^5	-104
2	3.94	2.16×10^5	4.49×10^7	2.15×10^5	-103
3	4.04	1.62×10^5	1.41×10^7	4.60×10^5	-95
4	4.26	1.21×10^5	1.13×10^7	1.20×10^5	-99
5	4.36	9.20×10^4	6.73×10^5	8.10×10^4	-95
6	4.40	7.64×10^4	9.11×10^5	7.05×10^4	-99
7	4.55	5.24×10^4	1.93×10^5	4.16×10^4	-101
8	4.60	9.03×10^4	1.57×10^6	8.54×10^4	-101
9	4.92	4.47×10^4	4.30×10^5	4.05×10^4	-102
10	5.03	1.55×10^4	1.72×10^6	1.54×10^4	-67

measurements and summarized in Table 6.2 and the quality factors and frequency are obtained from the first chip inspection.

Table 6.2 – Overview of material properties as obtained by the DC measurement (see Appendix A.3). Note that NbTiN resistance is obtained by a throughline measurement and T_c^{NbTiN} is unfortunately not measured and set to an earlier mentioned value found in [39].

Material	T_c [K]	R_s [$\Omega/\square$]	d [nm]	ρ_N [$\mu\Omega$cm]
Al	1.318	0.378	40	1.51
NbTiN	14	12.9	100	129

Noise Spectra Comparison

First, the noise spectrum is calculated at both 120 mK and 270 mK and compared to the measured data, the result of which is shown in Fig. 6.2. In the figure, the modelled individual noise contributions are shown as well: the G-R noise (Eqs. 2.4.1), LNA noise (Eq. 2.4.10) and TLS noise (Eqs. 2.5.2, 2.5.4).

In the measured phase noise at $T = 270$ mK, a flat spectrum with a roll-off is observed, indicative for a G-R noise dominated system, as expected by the model. By comparing the data with the model, it is clear that the agreement is qualitatively good: both model and calculation show a flat noise level with a single roll-off. The flat noise level (for $f < 10^3$ Hz) of the calculated spectrum is a few dB higher than the measured one. Furthermore, the roll-off in the noise spectrum is observed at a higher frequency than calculated, indicating that the experimental quasiparticle lifetime is shorter than calculated. A fit to the measured spectrum (*dashed red line*) gives $\tau_{qp}^{fit} = 0.05$ ms, whereas $\tau_{qp}^{calc} = 0.12$ ms. An analysis of the two effects, low experimental noise level and short quasiparticle lifetimes, is given in section 6.6.1 and section 6.4, respectively.

The low temperature $T = 120$ mK data and model do not match. The measured noise spectrum is characterised by a $\sim 1/\sqrt{f}$ slope, which is indicative of a TLS noise dominated noise spectrum. No G-R noise signature is observed in the measured spectrum. Interestingly, the calculated TLS noise spectrum (*black dash-dotted line*) is much lower than the measured spectrum.

To summarise, at $T = 270$ mK the observations are

- A slightly lower noise level compared to the model, indicative of a low response.
- A shorter lifetime than expected from the model calculations.

At $T = 120$ mK, the observations are

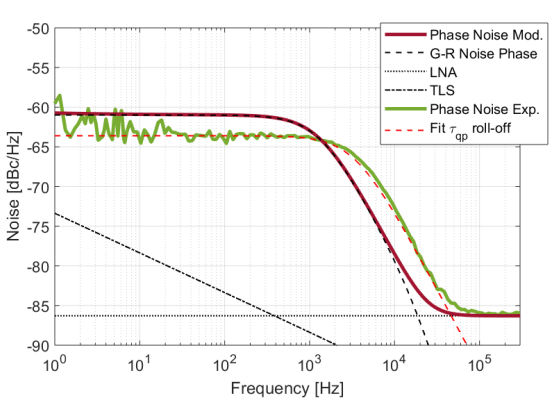

PSD at $T = 270$ mK, $P_{\text{read}} = -98$ dBm

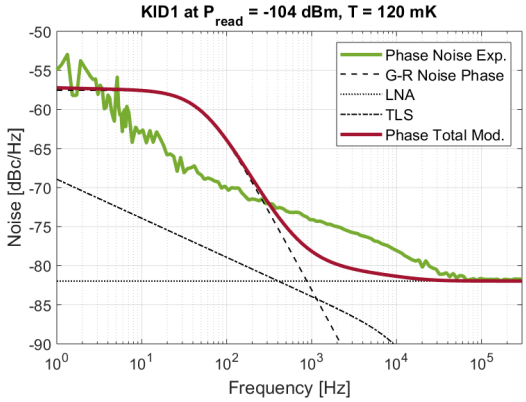

PSD at $T = 120$ mK, $P_{\text{read}} = -104$ dBm

Figure 6.2 – Measured (*green*) and modelled (*dark red*) phase noise spectra for KID 1 at high and low temperature. **(a)** The measured phase noise shows shows a flat noise level with spectrum roll-off around $f = 10^3$, with $\tau_{\text{qp}}^{\text{fit}} = 0.05$ ms (*red dashed line*). **(b)** A low temperature, no roll-off is visible in what seems a TLS dominated noise spectrum. The model assumes $\tau_{\text{qp}} = 3$ ms and clearly overestimates the low frequency noise level, while the TLS noise contributions seems to be significantly underestimated.

- An absence of any G-R noise signature in the spectrum
- A TLS noise level much higher than predicted.

The next three sections will individually assess the measured and calculated TLS noise contributions, temperature dependent quasiparticle lifetime and the phase responsivity. Afterwards, the data and model are again compared.

Table 6.3 – Overview of input parameters for the model calculation. Note the last two rows, where the measured quality factors and the applied readout power are different for different chip temperatures.

Al/ Hybrid	d (nm)	ρ_N (µΩ cm)	T_c (K)	S (µm)	W (µm)	ℓ (µm)	S_ref (dBc/Hz)
	40	1.51	1.318	0.64	1.36	250	-179
	η_pb	N_0 ($\mu\mathrm{m}^{-3}\mathrm{eV}^{-1}$)	τ_0 (ns)	v_F (m/s)			
	0.40	1.72×10^{10}	458	2.03×10^6			
NbTiN	d (nm)	ρ_N (µΩ cm)	T_c (K)	S (µm)	W (µm)	ℓ (µm)	S_ref (dBc/Hz)
	100	129	14	20	10	6430	-193
KID/ Substrate	P_read (GHz)	F_0 (dBm)	Q_c	Q_i	τ_qp (ms)	LNA T_N (K)	ε_r
$T = 120$ mK	-104	3.78	1.20×10^5	1.25×10^7	3	4.5	11.49
$T = 270$ mK	-98	3.78	1.25×10^5	2.51×10^5	0.12	4.5	11.49

6.3 TLS noise

The noise properties of the NbTiN and NbTiN-Al blind resonators on the chip are compared to the TLS model calculations (Eqs. 2.5.1 - 2.5.4) to extract TLS reference levels for the pure NbTiN CPW and the NbTiN-Al CPW. The expected values $S_{\mathrm{ref,metal-substrate}}$ as used in the KID design can be found in Table 6.3. After analysing the noise properties of the blind resonators, the new reference values are verified to the seven hybrid MKID spectra. This verification is possible because the spectra show a $\sim 1/\sqrt{f}$ noise dependence at low temperatures ($T = 120$ mK), indicating a TLS noise dominated system, even for the resonators with an aluminium section.

6.3.1 Blind NbTiN resonator

To experimentally quantify $S_{\mathrm{r,NbTiN-Si}}$, the noise spectra of the blind NbTiN resonator are compared to the TLS model. The left panel of Fig. 6.3 shows the measured noise spectra for varying readout powers. At modulation frequencies $f > 10^3$ Hz, the spectra hit a readout power dependent noise floor. This amplifier noise contribution becomes increasingly dominant for lower readout powers. Therefore, the spectra are corrected for this white noise contribution after which a power law fit is carried out within a limited frequency range around $f_{\mathrm{ref}} = 10^3$ Hz, as shown in the middle panel. This results in a $f^{-0.67(1)}$ dependence, slightly higher than the Gao dependence, $a = -0.5$ as used in the TLS model.

To obtain $S_{\mathrm{r,NbTiN-Si}}$, the corrected noise level at f_{ref} as a function of readout power is compared to the expected noise level (right panel). The data is first interpolated to $P_{\mathrm{ref}} = -40$ dBm, again using a power law fit which gives $P_{\mathrm{int}}^{-0.52(1)}$ closely resembling the literature value $b = -0.5$. Now, $S_{\mathrm{ref,NbTiN-Si}}$, the only unknown in the TLS model equation, is matched to the noise level at $f_{\mathrm{ref}}, P_{\mathrm{ref}}$ and compensated for the CPW width scaling $S_{\mathrm{TLS}} \propto W_{\mathrm{t}}^{-1.6}$. This results in $S_{\mathrm{ref}} = -186(1)$ dBc/Hz, around 7 dB higher than expected.

In this rescaling, it is assumed that the CPW width dependence of TLS noise is the same as Gao *et al* [34] found, although they used resonators with a gap-line-gap 2-3-2, while this blind resonator has a 3-2-3 gap and line width ratio.

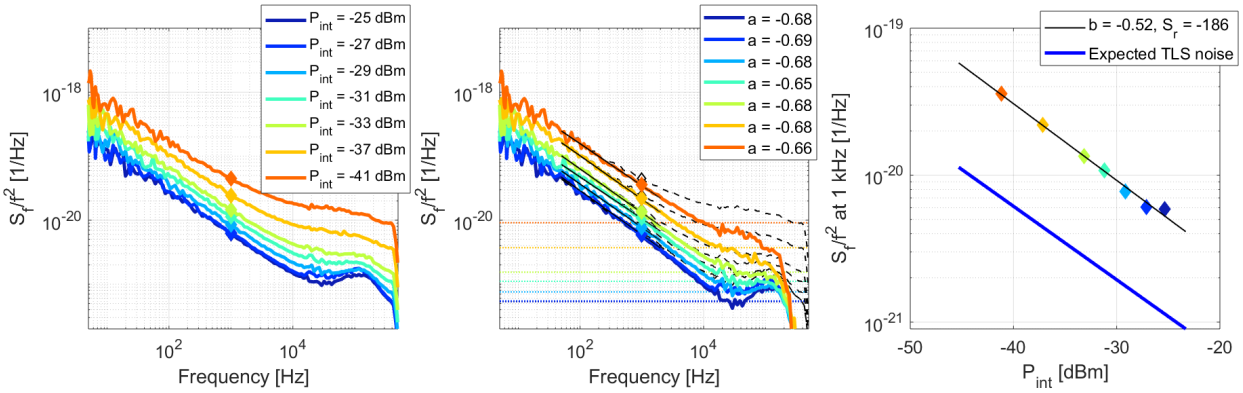

Figure 6.3 – (left) Measured fractional frequency noise spectra (S_{f}/f^2) of the blind NbTiN resonator for a range of readout powers, shown here as internal powers. (middle) Setupnoise corrected spectra including a power law fit for $f = 50 - 2000$ Hz, the result of each fit is indicated in the legend. (right) Fractional frequency noise at $f = 10^3$ Hz as function of internal power, from which the TLS reference noise level for this device is extracted.

6.3.2 Blind Al resonators

By a similar procedure as before, the Al-SiN TLS noise properties are obtained from the noise spectra of the two blind Al resonators. The difference in this case is that the blind Al resonators do have a NbTiN coupler, which is accounted for by using the new reference value $S_{\mathrm{ref}}^{\mathrm{NbTiN-Si}} = -186(1)$ dBc/Hz. Fig. 6.4 shows the noise spectra of KID 10, the long Al resonator, for several internal powers. The number of internal powers per KID depends on whether or not the resonator is overdriven at high powers which are excluded in this model comparison. Due to the long and narrow Al line, the fractional frequency noise is much higher in

comparison the blind NbTiN resonator and setupnoise correction has no influence on the noise level around $f_{\mathrm{ref}} = 1$ kHz.

The fitrange in the left panel of Fig. 6.4 is set to avoid a $1/f$ noise contribution due to *warm* electronics for low frequencies ($f \sim 10$ Hz)and a roll-off due the resonator ringtime at high frequencies ($f \sim 10^4$ Hz).

To obtain $S_{\mathrm{ref}}^{\mathrm{Al-SiN}}$, the data as presented in the right panel is first interpolated to $P_{\mathrm{int}} = -60$ dBm, as this lies within the range of the few datapoints available. Subsequently, $S_{\mathrm{ref}}^{\mathrm{Al-SiN}}$ is extracted by comparing the data with the modelled TLS noise level, calculated at $f_{\mathrm{ref}} = 10^3$ Hz, $P_{\mathrm{int}} = -60$ dBm. The TLS model (Eqs. 2.5.1 - 2.5.4) includes the power law dependencies $a = -0.5, b = -0.5, c = -1.6$ and relevant spatial dimensions (Table 4.3). This results in $S_{\mathrm{ref}}^{\mathrm{Al-SiN}} = -162 \pm 4$ dBc/Hz, very significantly higher than the expected value of -179 dBc/Hz.

The same procedure is repeated for the second blind Al KID (see appendix), which has a shorter Al section, and gives $S_{\mathrm{ref}}^{\mathrm{Al-SiN}} = -156 \pm 1$ dBc/Hz. On average, the new TLS reference value is therefore $S_{\mathrm{ref}}^{\mathrm{Al-SiN}} = -159 \pm 4$ dBc/Hz. Both the material combinations, NbTiN-Si and Al-SiN, give significantly higher TLS contributions than the expected. This could be due to the exact cleaning steps in fabrication process, which is a known issue, but not the focus of this project.

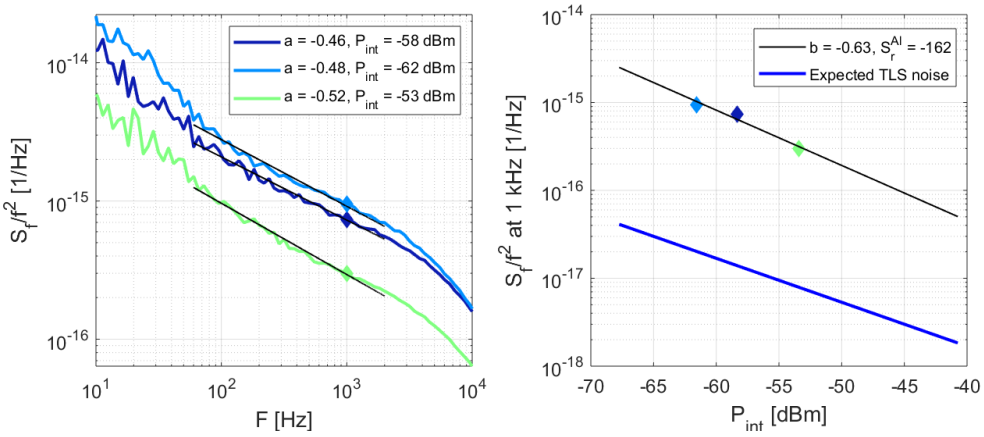

Figure 6.4 – Noise spectra of blind Al resonator, KID 10.

6.3.3 Hybrid MKIDs

As a verification, given the material specific TLS contributions, the measured spectra of the seven hybrid MKIDs can now be compared to the model calculations. This comparison is only possible because at low temperature ($T = 120$ mK), no indication of G-R noise is visible (i.e. flat noise level, roll-off around $f = 10^1 - 10^3$ Hz), solely a $1/\sqrt{f}$ dependence as expected for a TLS dominated system. Analogues to the procedure as described in the previous two sections, the $f_{\mathrm{ref}} = 1$ kHz noise level is determined for each hybrid MKID. Fig. 6.5 shows the data from the hybrid MKIDs at $T = 120$ mK, $f = f_{\mathrm{ref}}$, interpolated to $P_{\mathrm{int}} = -60$ dBm (*green*), together with a model calculation using the new TLS reference values as input, all as a function of the fractional aluminium length of the resonator. The calculated curve matches the data very well, if $S_{\mathrm{ref}}^{\mathrm{NbTiN-Si}}$ is set 1 dB higher than the value found in the previous section (a change that is within its error). Additionally, due to the extremely high value of $S_{\mathrm{ref}}^{\mathrm{Al-SiN}}$, the noise is dominated by the narrow aluminium section in most cases, except for the shortest aluminium section.

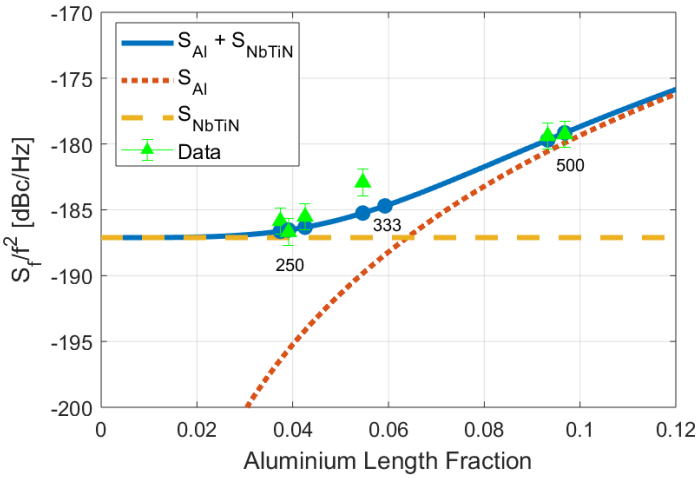

Figure 6.5 – Fractional frequency noise as function of aluminium length fraction of the resonator. The individual TLS noise contributions as determined from the blind resonators are graphed separately for both Al-SiN and NbTiN-Si (dotted red and dashed yellow, respectively), alongside the noise data for the 7 hybrid MKIDs at low temperature. The 3 different aluminium lengths (in µm)are indicated in the graph. Good agreement to the hybrid data is found if the $S_{\mathrm{ref}}^{\mathrm{NbTiN-Si}}$ is set 1 dB higher to −185 dBc/Hz, which falls within the uncertainty.

6.4 Recombination time

In this section, the temperature dependent quasiparticle lifetime is analysed. First, τ_{qp} is retrieved from the spectrum roll-off. This strategy is only applicable if G-R noise is visible, which is the case for temperatures $T > 200$ mK. Fig. 6.6 shows the phase noise of KID 1 for several temperatures, including the fits by which the lifetimes are determined. The $T = 120$ mK spectrum shows no G-R noise but added for illustration purposes, the lifetime is determined by pulse analysis as discussed in the next section.

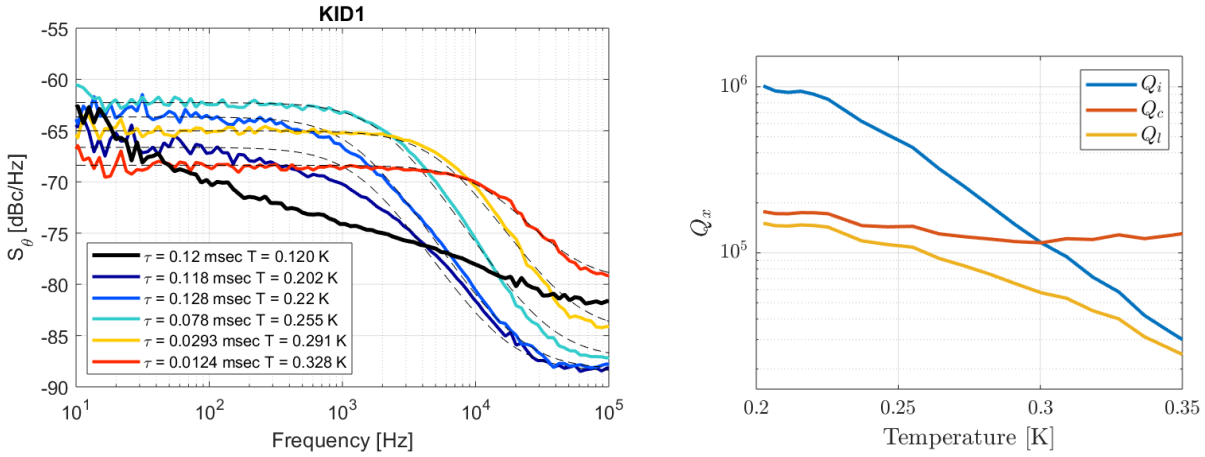

Figure 6.6 – **(a)** Temperature dependent quasiparticle lifetimes obtained from a fit to the spectrum roll-off. The lifetime at the lowest temperature is determined via a pulse decay fit. **(b)** Measured temperature dependent Quality factors. The loaded quality factor diverges from the constant Q_{c} around $T = 250$ mK as Q_{i} strongly decreases with increasing temperatures. At high temperatures, the decreasing Q_{l} causes the decrease of the constant noise level around as seen in the left panel.

The quasiparticle lifetime is shown as a function of temperature in Fig. 6.7. For $T > 250$ mK, the lifetime follows an exponential decay with temperature as expected from the expression for τ_{qp} at thermal equilibrium (Eq. 2.1.3). The only unknown left in $\tau_{\mathrm{qp}}(T)$ is the electron-phonon interaction time τ_0, which is retrieved by a fit to the data. This gives the experimental value $\tau_0^{\mathrm{exp}} = 176 \pm 4$ ns. To compare this result to the theoretical value of Kaplan *et al* ($\tau_0 = 438$ ns) [17], τ_0^{exp} is multiplied by a factor of two, originating from the fact that the cited theoretical result of Kaplan *et al* considers the quasiparticle lifetime of a single quasiparticle, while a single recombination event involves two quasiparticles [17]. Hence, the corrected experimental value of 352 ± 8 ns is in reasonable agreement. The density of quasiparticles at $T = 120$ mK and $\tau_{\mathrm{qp}} = 0.12$ ms is $n_{\mathrm{qp}} = 446$ µm^3.

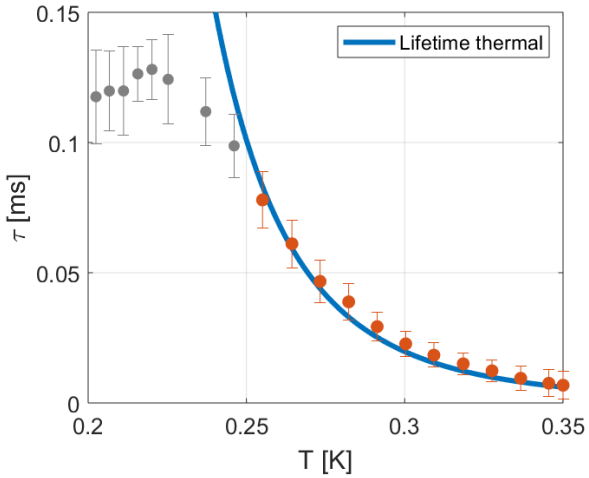

Figure 6.7 – Quasiparticle lifetimes as function of temperature as obtained from the spectrum roll-off shown in Fig. 6.6. The expected thermal $\tau_{qp}(T)$ behaviour is fitted to the data for $T > 0.25$ K as to retrieve the electron-phonon interaction time, $\tau_0 = 176 \pm 4$ ns. The lifetime saturates to 0.12 ms for $T < 0.24$ K.

6.4.1 Pulse Method

As an alternative to a roll-off frequency fit, the quasiparticle lifetime can be obtained from pulse decays caused by high energy hits. However, this method is less reliable, because these pulses are high, and at the pulse peak the quasiparticle density is higher than its equilibrium. Measuring close to equilibrium is prohibited by the noise.

Nevertheless, the pulse method offers a solution when no spectrum roll-off is visible such as in the $T = 120$ mK noise spectrum shown in Fig. 6.6 . Hence, in this case, τ_{qp} is retrieved by searching the time domain trace for high energy hits and fitting the pulse decay.

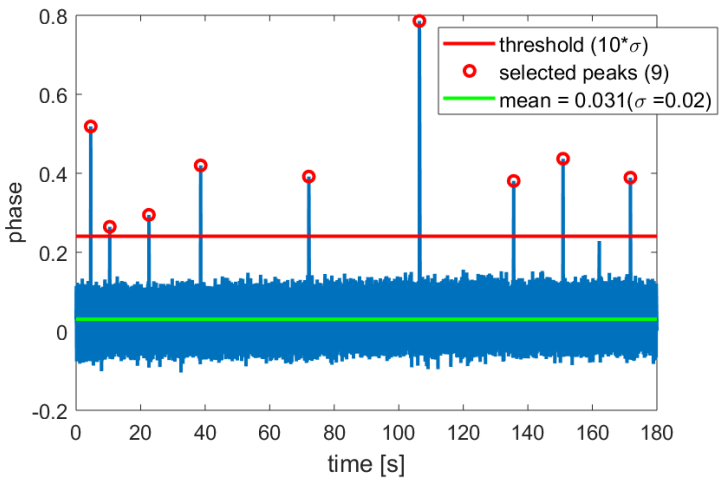

Figure 6.8 – Time domain trace of normalized phase response for 180 s, for KID 1 at $P_{read} = -108$ dBm. Peaks are selected by a 10σ threshold level above the mean. Because the chip is designed to reduce high energy impacts and the small area, a large time trace only gives few peaks.

Figure 6.9 shows a pulse fit and multiple lifetimes for KID 1 at $P_{read} = -108$ dBm. There is a large scatter in lifetimes, even after a manual selection of the fits as roughly 20% of the selected peaks give a wrong pulse fit. In part, this is due to the sampling speed (50 k/s) combined with the fast decay (short observed lifetimes of around 0.12 ms). Nevertheless, the results from the pulse fits are consistent with the oberved lifetime saturation from the specrum roll-offs in the previous section.

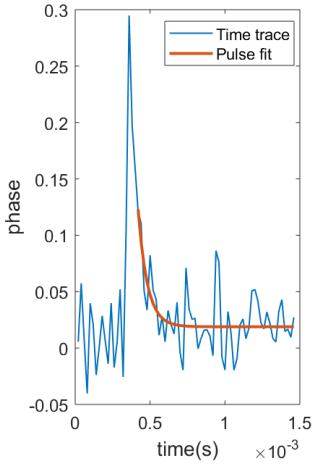

Time trace

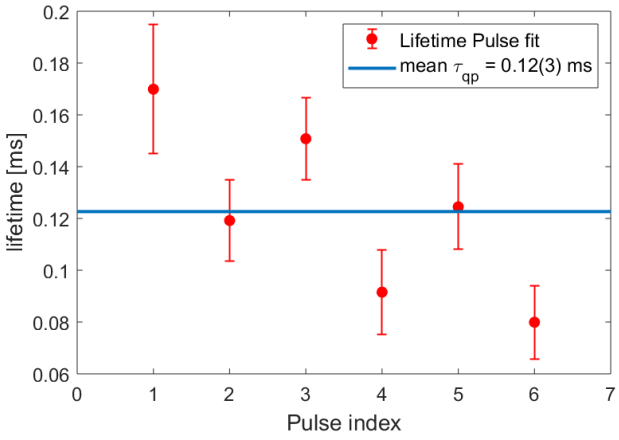

Lifetimes from pulse decay

Figure 6.9 – The lifetime is obtained from the tail of the exponential peak decay, as high energy impacts could initially saturate the device. **(a)**An example of such a pulse fit. **(b)** The lifetimes from pulse method for KID 1 at $P_{\mathrm{read}} = -108$ dBm. The lifetimes vary over a factor of 2 for a single KID. The mean $\tau_{\mathrm{qp}} = 0.12(3)$ ms.

6.5 Responsivity Measurement

The phase responsivity, $\mathrm{d}\theta/\mathrm{d}N_{\mathrm{qp}}(T)$ is experimentally obtained by measuring the shifting resonance frequency as function of temperature, as described in detail by Baselmans *et al* [52]. For this measurement, the phase responsivity is written as

$$\frac{\mathrm{d}\theta}{\mathrm{d}N_{\mathrm{qp}}} = \frac{\mathrm{d}\theta}{\mathrm{d}F}\frac{\mathrm{d}F}{\mathrm{d}N_{\mathrm{qp}}} = \frac{-4Q}{F_0}\frac{\mathrm{d}F}{\mathrm{d}N_{\mathrm{qp}}} \tag{6.5.1}$$

where the quality factor and resonance frequency are obtained by measuring the complex transmission S_{21} during a frequency sweep. The temperature is converted to number of quasiparticles using Eq. 2.1.2 and the Al volume. The measured transmission of a series of frequency sweeps for increasing temperatures are shown for KID 1 in Fig. 6.10a, in which the black dots at the peak minima are the corresponding resonance frequencies. In Fig. 6.10b, this data is presented as frequency shift $\mathrm{d}x = \delta F / F_0$ as function of quasiparticle number. As expected, the resonance frequency goes down with increasing temperatures. Moreover, the slope $\mathrm{d}F/\mathrm{d}N_{\mathrm{qp}}$ is constant as expected from BCS theory [16, 22] and thereby the responsivity is known.

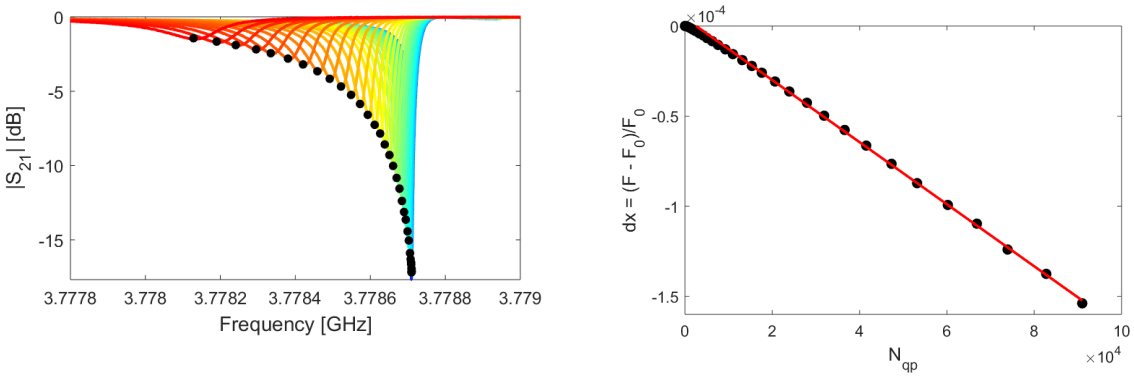

Figure 6.10 – Responsivity measurement. **(a)** For each temperature a frequency sweep is graphed by which $Q, F(T)$ are determined. The black dots correspond to the resonance frequency and shifts downward for increasing temperatures.**(b)** The frequency change as function of the number of quasiparticles is linear, from which the phase responsivity is determined (see Eq. 6.5.1).

6.5.1 Comparison with modelled responsivity

Now, the modelled and measured responsivity are compared to each other as summarized in Table 6.4. The modelled responsivity is slightly lower than the experimental value.

Table 6.4 – nice overview of everything

	F_0 [GHz]	$\frac{\mathrm{d}\theta}{\mathrm{d}N_{\mathrm{qp}}}$	α_{k}
Experiment	3.78	$(7.5 \pm 0.1) \times 10^{-4}$	$(5.1 \pm 0.1) \times 10^{-2}$
Model	3.95	6.5×10^{-4}	3.8×10^{-2}

The experimental kinetic inductance fraction is retrieved by referring back to the expression for the theoretical phase responsivity (Eq. 2.3.20) and solving for α_{k} using the measured Q, $\mathrm{d}\theta/\mathrm{d}N_{\mathrm{qp}}$ and the complex conductivity relations (Eq. 2.2.6). The model underestimates α_{k} by 25%.

Three possible reasons for this deviation could be differences in the exact geometry of the device, a difference in the Al critical temperature and sheet resistance or a difference in the NbTiN sheet resistance.

However, because these parameters are determined within 10% uncertainty and α_k is roughly linearly dependent on all, it is not likely that any of these could be the cause of deviation in.

An additional reason could be that the electron energy distribution is not a thermal one, but modified due to the microwave readout signal [41]. This nonequilibrium distribution affects the complex conductivity and could therefore be the cause of mismatch in α_k. The effect could be checked in another experiment by probing the MKIDs with lower readout powers.

Also, the resonance frequency is overestimated.
By using the experimentally obtained α_k, the resonance frequency is lowered and can be estimated using that $F_0 \propto \sqrt{1-\alpha_k}$ (see Eq. 2.3.12). This gives 3.92 GHz. Two possible explanations for the mismatch in F_0 are considered:

1. The lower relative permittivity of the SiN patch ($\epsilon_r^{SiN} \simeq 7$ while $\epsilon_r^{Si} = 11.49$) was not accounted for in the model. However, this would only increase F_0. Furthermore, including this layer in the CPW transmission simulation, $Z/Z' = \sqrt{\epsilon'_{eff}/\epsilon_{eff}}$ the frequency shift is less than 1%.

2. The antenna structure in the aluminium section interrupts the CPW groundplanes and effectively lengthens the resonator and thereby lowers F_0.

6.6 Noise Model Validation

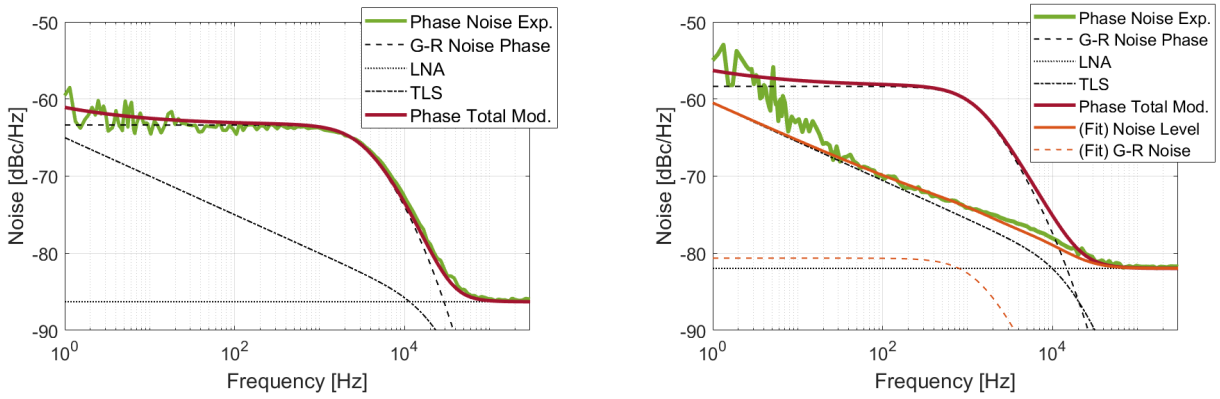

PSD at $T = 270$ mK, $P_{\text{read}} = -98$ dBm

PSD at $T = 120$ mK, $P_{\text{read}} = -104$ dBm

Figure 6.11 – Measured (*green*) and modelled (*dark red*) phase noise spectra for KID 1 at high and low temperature. The model input for the phase noise is based on separate measurements of the responsivity and TLS noise levels and a measured τ_{qp}. **(a)** At $T = 270$ mK, the model seems consistent with the data. **(b)** At $T = 120$ mK, the modelled noise level is too high. The fit of the G-R noise level (*orange lines*) to the data results in a responsivity of around 7% of the expected responsivity as measured in the previous section.

In this section, the modelled phase noise is again compared to the data, using new input that is based on the independent experimental results of the previous section. Namely, the TLS reference noise levels are determined via blind resonators and verified on all the hybrid MKIDs, the quasiparticle lifetimes are determined via either the spectrum roll-off frequency or a pulse decay fit and τ_0 is then extracted from the temperature dependent quasiparticle lifetime $\tau_{\text{qp}}(T)$. The quality factors and resonance frequencies are extracted from a measurement of the transmission during a frequency sweep. The responsivity is determined by varying the chip temperature and measuring the frequency shift. An overview of the experimentally obtained values for these parameters is given in Table 6.5, which also serves as the new input for the modelled phase noise shown in Fig. 6.11

For $T = 270$ mK, the model is quantitatively consistent with the data.

At low temperature ($T = 120$ mK), the measured noise level is in agreement with the theoretical TLS noise prediction: The noise has a $1/\sqrt{f}$ dependence and has a roll-off consistent with the resonator Quality factor. The predicted TLS noise is higher than $T = 270$ mK case because its lower readoutpower and higher quality factor, both increasing TLS noise. However, we would expect the G-R noise to be clearly visible, dominating the spectrum, as shown by the black dotted line in Fig. 6.11b, but no evidence of G-R noise is visible. When the G-R noise level is fitted to the 120 mK data (*orange lines*), this results in a responsivity of 7% of the model input.

Table 6.5 – Overview of initial input parameters and their experimentally obtained values such as described in the previous sections on TLS noise, recombination time and responsivity. The measured values are used for the phase noise model comparisons as presented in Fig. 6.11.

Parameter			Initial Input	Measured
$S_{\text{ref}}^{\text{NbTiN-Si}}$	[dBc/Hz]		-193	-185 ± 1
$S_{\text{ref}}^{\text{Al-SiN}}$	[dBc/Hz]		-179	-159 ± 4
τ_0	[ns]		458	176 ± 4
τ_{qp}	[ms]	($T = 270\,\text{mK}$)	0.12	0.05 ± 1
τ_{qp}	[ms]	($T = 120\,\text{mK}$)	3	0.12 ± 3
$\frac{\text{d}\theta}{\text{d}N_{\text{qp}}}$	[*rad/qp*]		6.5×10^{-4}	$(7.5 \pm 0.1) \times 10^{-4}$

6.6.1 Temperature dependent noise level

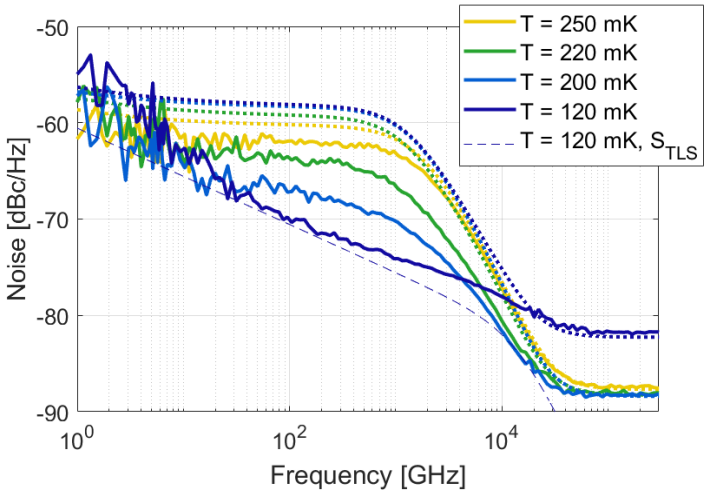

Figure 6.12 – Measured (*lines*) and modelled (*dashed lines*) phase noise spectra for KID 1 for decreasing temperatures. The readoutpower used to probe the KID is $P_{\text{read}} = -98$ dBm, except for the spectrum at the lowest temperature for which $P_{\text{read}} = -104$ dBm is shown due to the resonator being overdriven at higher readout powers. Where the modelled phase noise level stays around $S_\theta = -57$ dBc/Hz, the measured spectra drop as the temperature decreases.

This section continues the observations of the high and low noise spectra in Fig. 6.11 which suggest a vanishing response as the temperature decreases. Therefore, Fig. 6.13 combines the modelled and measured noise spectra for varying temperatures. Indeed, the response appears to vanish gradually as the temperature decreases. This behaviour is not expected. The roll-off is observed to be more or less constant and in agreement with the previously reported lifetime of 0.12 ms.

The modelled noise level is constant and around $S_\theta = -57$ dBc/Hz, but lowers for $T > 250$ mK due to decreasing Q-factors. The figure shows a transition from thermal behaviour at high T towards a regime where the G-R noise gradually vanishes. This coincides with the observed quasiparticle lifetime saturation and is attributed to the readoutpower.

6.6.2 NEP analysis

In this section the experimental NEP is compared to an initial calculation and the model, the input of which is given in section 6.2 and 6.6, respectively. The experimental NEP is obtained via the measured noise spectrum at $T = 120$ mK and a measurement of the optical responsivity, because at low temperatures, the electrical responsivity deviates from its linear $F(N_{\text{qp}}(T))$ behaviour (see section 6.5).

Fig. 6.13 shows the measured and modelled NEP, including an initial calculation based on an assumed quasiparticle lifetime of 3 ms and the input as given in Table 6.5. The experimental NEP lies in between the ab initio calculation and the modelled NEP. This was expected since at low temperatures, the model overestimates the phase noise level (Fig. 6.13) while the modelled NEP is obtained using the same experimental optical responsivity. The ab initio calculation assumes a long quasiparticle lifetime, $\tau_{\text{qp}} = 3$ ms, hence, the NEP is low.

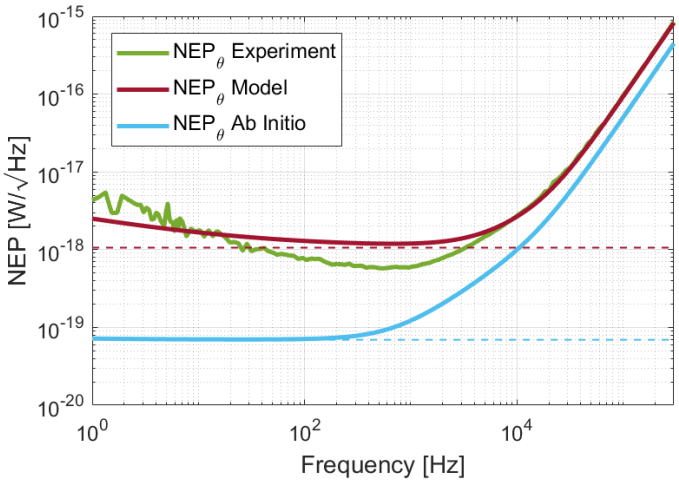

Figure 6.13 – Measured and modelled NEP using optical responsivity, for KID 1 with the input as given in Table 6.5. Note that the experiment and model are not corrected for optical efficiency, $\eta_{\mathrm{opt}} = 0.35$. The ab initio NEP is lower due to its long assumed quasiparticle lifetime.

6.7 Optical NEP

In this section, the optical NEP measurement is shown and discussed for KID 1. First, the noise spectra are obtained for a range of radiation powers by varying the black body temperature such as described in Chapter 5. This is shown in Fig. 6.14 for both amplitude (*dashed lines*) and phase (*solid lines*) noise.

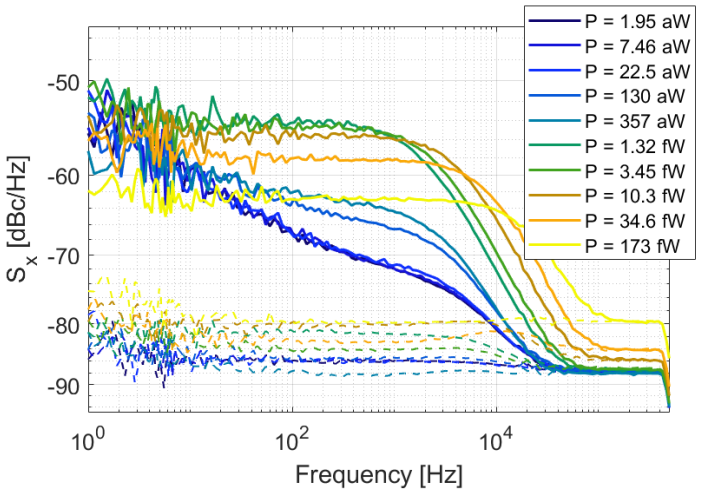

Figure 6.14 – Noise spectra of KID 1 for a range of radiation powers. Both amplitude *(dashed lines)* and phase *(solid lines)* noise are shown.

At low radiation powers $P < 22.5$ aW, the phase noise spectra seem TLS dominated due to the observed $1/\sqrt{f}$ slope and as the visible roll-off is associated with the resonator ringtime. The amplitude noise is much lower and nearly setupnoise limited, around $S_{\mathrm{A}} = -80$ dBc/Hz.

To obtain the optical NEP as shown in Fig. 6.15, the optical responsivity, noise spectra and measured lifetimes are combined using Eq. 2.4.11. The NEP_θ at low powers saturates and $f = 140$ Hz saturates at $(3.4 \pm 0.2) \times 10^{-19}$ W/$\sqrt{\mathrm{Hz}}$, an order of magnitude lower than NEP_{A} due to the difference in responsivity. As can be seen in Fig. 6.15, the low P_{abs} spectra continue to decrease up to a frequency of 1 kHz. This is due to the short observed lifetimes in combination with the TLS dominated spectrum. Hence, $NEP_\theta(f = 1000\,\mathrm{Hz})$ saturates to a slightly lower value of $(2.4 \pm 0.2) \times 10^{-19}$ W/$\sqrt{\mathrm{Hz}}$ as can be seen in Fig. 6.15.

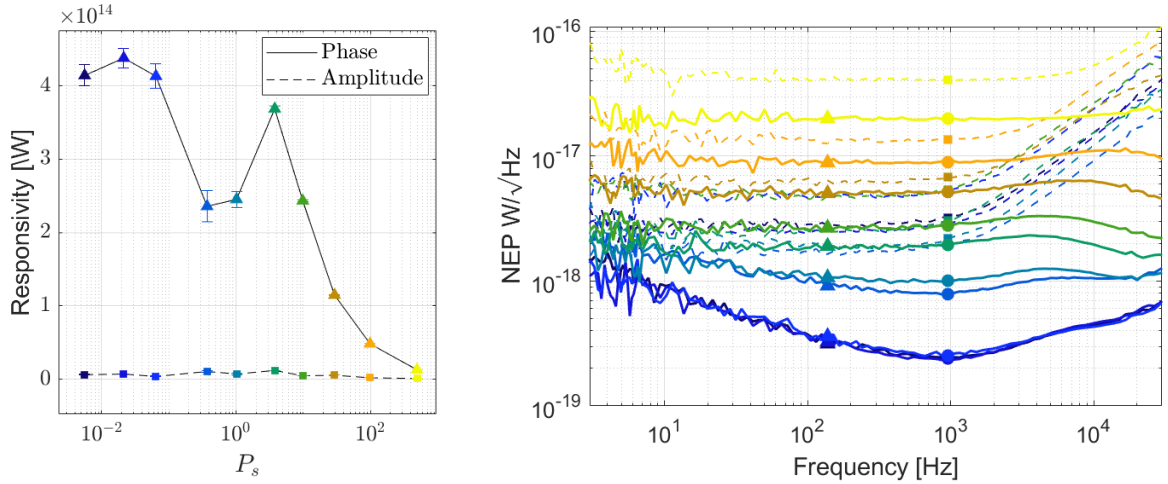

Figure 6.15 – **(a)** Optical responsivity for KID 1 as function of radiation power. **(b)**Optical NEP for KID 1, corrected for the optical efficiency $\eta_{\text{opt}} = 0.35 \pm 0.03$, the markers at $f = 140$ Hz and $f = 1000$ Hz correspond to the points graphed in Fig. 6.16.

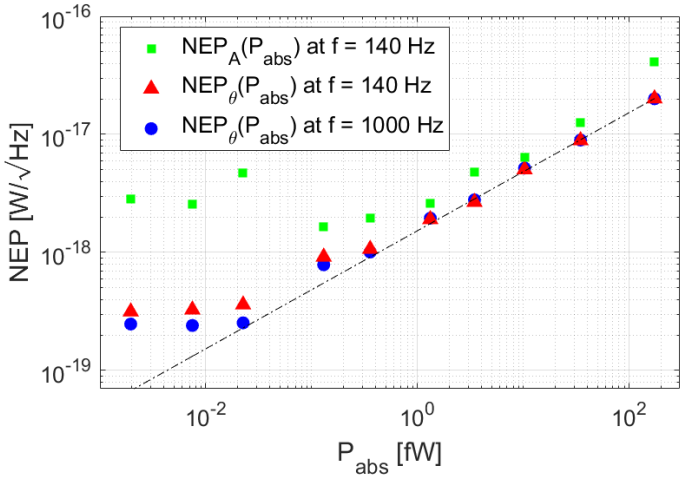

Figure 6.16 – Optical NEP versus absorbed radiation power ($P_{\text{abs}} = \eta_{\text{opt}} P_{\text{s}}$) for phase and amplitude readout at $f = 140$ Hz and $f = 1000$ Hz, corresponding to the points in Fig. 6.15

Chapter 7

Discussion and Conclusions

The goal of this project was to design and test an MKID detector optimized for a low Noise Equivalent Power as to reach the sensitivity requirements for a future space-based 4 K cooled observatory. Based on a state-of-the-art hybrid MKID design which minimizes TLS noise and maximizes the response to quasiparticles, I developed a realistic low NEP device by minimizing the active volume of the resonator while ensuring all radiation from a $\nu_{\mathrm{rad}} = 1.54$ THz source is absorbed.

The in-house fabricated device was measured at SRON, Utrecht. An initial experiment and theory comparison of the noise spectra indicated that (*i*) the model underestimates TLS noise contributions, (*ii*) the model overestimates the response and (*iii*) quasiparticle lifetimes are observed to be shorter than expected. Subsequently, these three factors were individually analysed using independent measurements. (*i*) The material specific TLS noise contributions, analysed using the blind resonators, results in significantly higher reference values. (*ii*) The temperature dependent quasiparticle lifetime determined from the PSD frequency roll-off and pulse decay behaves as expected from theory up to a saturation around ~ 0.12 ms for temperatures $T < 240$ mK, significantly lower than the previously measured lifetime saturation of 3 ms. (*iii*) The phase responsivity as obtained from the temperature dependent shift in resonance frequency is higher than expected, indicating the model underestimates the kinetic inductance fraction by 25%.
These results served as new model input to make a more accurate comparison to the measurement data. For high temperatures $T > 270$ mK, good overall agreement is found between the measured spectra and model. However, as the temperature decreases, the observed noise level drops dramatically and a TLS dominated spectrum remains. This is unexpected: the model predicts a temperature independent noise level, because the responsivity and product of quasiparticle number and lifetime are constant.
Also, the observed temperature dependence of the quasiparticle lifetime is in good agreement with the theory of Kaplan at high temperatures. Below $T = 240$ mK the lifetime saturates at a very short value of 0.12 ms. Furthermore, it is observed that the experimental kinetic inductance fraction that is slighty lower than calculated.

A possible underlying reason for all these effects could be a very strong readout power effect: The readout power modifies the electron energy distribution function and creates excess quasiparticles due to a multiple photon absorption process. These effects are known from the work by De Visser *et al*, but generally have lead to lifetimes down to ~ 1 ms. The effect is now much stronger, creating a strongly non-thermal electron energy distribution in the aluminium strip of the MKID. This nonequilibrium distribution in turn affects the Mattis-Bardeen expressions for the complex conductivity and could therefore cause the mismatch in α_{k} and the response to quasiparticles. Moreover, the phase responsivity might incorrectly assume an inverse linear relation (constant product) of quasiparticle lifetime and quasiparticle number as this assumes thermal equilibrium description as well. However, the exact microscopic details of this effect are unknown and the readout power effect is not studied in detail in this project, therefore, at this point I cannot provide a solid explanation for the observed low temperature noise level drop.
Finally, the optical NEP was determined as function of radiation power, using the optical responsivity: $NEP_\theta(f = 140\,\mathrm{Hz}) = (3.4 \pm 0.2) \times 10^{-19}$ W/$\sqrt{\mathrm{Hz}}$. This is a similar sensitivity as current state-of-the-art MKID detectors, due to the observed short quasiparticle lifetimes which limit the NEP. However, the short lifetimes do make this device faster for equal sensitivity.

Furthermore, the short quasiparticle lifetime combined with the $1/\sqrt{f}$ slope of the TLS dominated spectrum at $T = 120$ mK makes it possible to define a lower NEP at a modulation frequency as high as $f = 1$ kHz. This results in $NEP(f = 1\,\text{kHz}) = (2.4 \pm 0.2) \times 10^{-19}$ W/$\sqrt{\text{Hz}}$.

Still, there is plenty of room for improvement in the sensitivity and physical understanding of this device. To gain better understanding of the mechanism behind the unexpected decrease in noise level, and ultimately to reach the OST sensitivity requirements, the easiest next step would be to first reduce the TLS noise. Since TLS noise is relatively well understood excess noise source and high noise levels have been observed before, attributed to the specific cleaning steps involved in the chip fabrication, it should be relatively easy to lower the dominating TLS spectrum. Additionally, within the current resonator design constrictions of the 1.6 mm lens-to-lens spacing, there is still room for a wider NbTiN CPW, reducing the total TLS noise as well. This would allow an unobstructed observation of the G-R noise and readout power effects, even for low readout powers (which increase TLS noise).

To summarise, my recommendations for any future research directions within the framework of this project would be to reduce TLS noise, try to incorporate the effect of readout power on the quasiparticle energy distribution into the MKID model and study the G-R noise at lower readout powers.

Appendix A

Additional Measurements and Design Overview

A.1 Coupling Quality Factor

The coupling quality factor, Q_c, is due to the capacitive coupling to the feedline and is dependent on the resonator frequency and the coupler length. To estimate the Q_c of the resonators in this project, Sonnet simulations were performed on a readout line and coupler structure such as shown in Fig. A.1 as to obtain the absolute transmission between port 1 and 3 ($|S_{13}|$). Then, Q_c is determined via

$$Q_c = \frac{\pi}{2|S_{13}|^2} \,. \tag{A.1.1}$$

The result is summarised in Fig. A.2 for various coupler lengths (ℓ_c) as a function of microwave frequency. Note that Q_c is lower for a longer coupler as the capacitive coupling is stronger. The coupler length of the hybrid MKIDs is 93 µm, for which Q_c is given by the black dashed line in the right panel. The corresponding resonance frequencies for the hybrid MKIDs of Chip 2 are graphed as well (*red markers*).

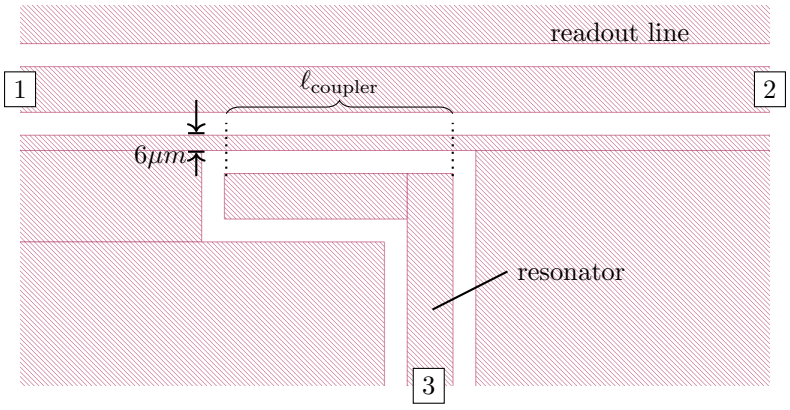

Figure A.1 – Snapshot of coupler and readout line as used in Sonnet simulations to obtain Q_c via the absolute transmission between port 1 and 3 ($|S_{13}|$). The CPW dimensions of both the readout line and resonator are 10-20-10 µm.

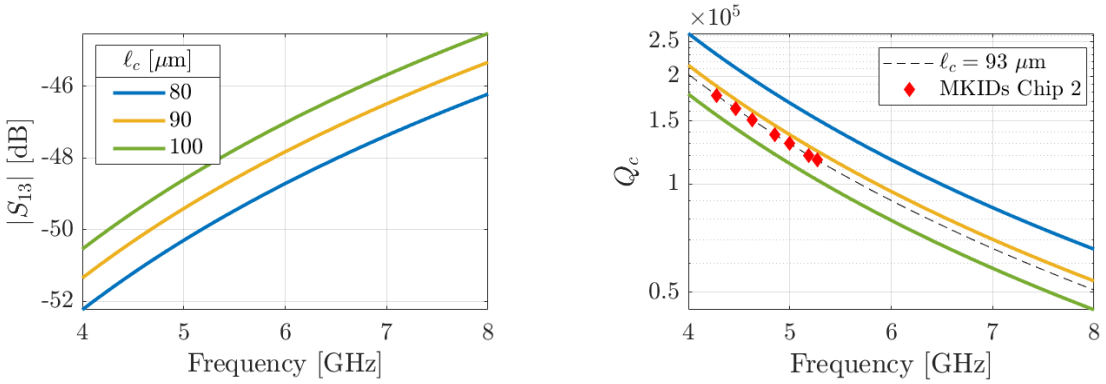

Figure A.2 – Simulated transmission and calculated coupling quality factors as function of microwave frequency for several coupler lengths, where it is used that $T_c^{\mathrm{NbTiN}} = 14$ K, $R_s = 4.0\ \Omega/\square$ and the sheet kinetic inductance $L_s = 0.4$ pH/$\square$ from Eq. 2.3.7.

A.2 Design overview

Parameter overview for chip 1 and 3.

Table A.1 – Overview of MKID parameters for chip 1, designed for a sheet resistance $R_s = 0.35\,\Omega/\square$ and 49 nm Al layer thickness.

KID	F_0 (GHz)	ℓ_{Al} (µm)	ℓ_{NbTiN} (µm)	ℓ_{tot} (µm)	Q_c
1	5.46	400	4803	5203	1.09×10^5
2	5.27	400	5000	5400	1.17×10^5
3	5.09	533	5045	5578	1.25×10^5
4	4.89	400	5440	5840	1.35×10^5
5	4.43	800	5459	6259	1.65×10^5
6	4.24	800	5752	6552	1.80×10^5
7	4.67	533	5521	6054	1.48×10^5
8	5.92	1225	3208	4433	0.92×10^5
9	5.88	2803	1147	3949	0.94×10^5
10	6.01	-	4903	4903	3.35×10^4

Table A.2 – Overview of MKID parameters for chip 3, designed for a sheet resistance $R_s = 1.0\,\Omega/\square$ and 22 nm Al layer thickness.

KID	F_0 (GHz)	ℓ_{Al} (µm)	ℓ_{NbTiN} (µm)	ℓ_{tot} (µm)	Q_c
1	4.26	162	6538	6600	1.78×10^5
2	4.44	162	6244	6406	1.64×10^5
3	4.58	216	5904	6120	1.54×10^5
4	4.82	162	5727	5889	1.39×10^5
5	4.95	216	5428	5640	1.32×10^5
6	5.02	324	5074	5398	1.28×10^5
7	5.19	324	4878	5202	1.20×10^5
8	4.91	1225	3208	4433	1.34×10^5
9	4.42	2803	1147	3949	1.66×10^5
10	6.01	-	4903	4903	3.35×10^4

A.3 DC Measurement

To obtain material parameters of the aluminium, a DC chip is mounted alongside the test chip. This to obtain the aluminium critical temperature, sheet resistance. The critical temperature is $T_c = 1.318\,\mathrm{K}$, sheet resistance $R_s = 0.378\ \Omega/\square$. Since the aluminium layer thickness is 40 nm, the resistivity is $1.51\,\mu\Omega\,\mathrm{cm}$. The NbTiN sheet resistance is obtained by measuring the resistance of the throughline at roomtemperature. This is reliable since the resistive properties of NbTiN do not change significantly for lower temperatures up to T_c i.e. the Residual Resistance Ratio $RRR \equiv R_{300\mathrm{K}}/R_{0\mathrm{K}}$ is nearly unity. The throughline resistance is $R = 29.75\,\Omega$ and the sheet resistance $R_s = 12.85\ \Omega/\square$.

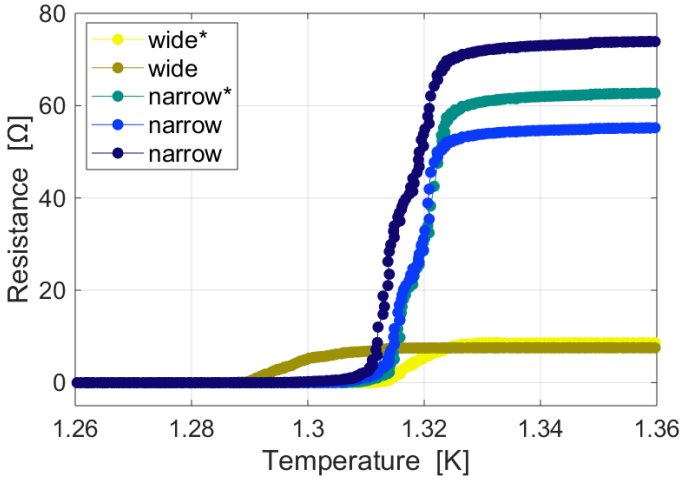

Figure A.3 – The DC measurement of aluminium gives its $T_c = 1.318$ K. The overetch of the narrow lines is not exactly known, therefore the sheet resistance is determined from the $T > T_c$ resistance of the wide lines, resulting in $R_s = 0.378\ \Omega/\square$. The stars indicate the aluminium strips with extra resist patch during the fabrication process.

A.4 TLS measurement

Noise spectra of the Al-NbTiN blind resonator, KID 8, in addition to the spectra showed in section 6.3.2.

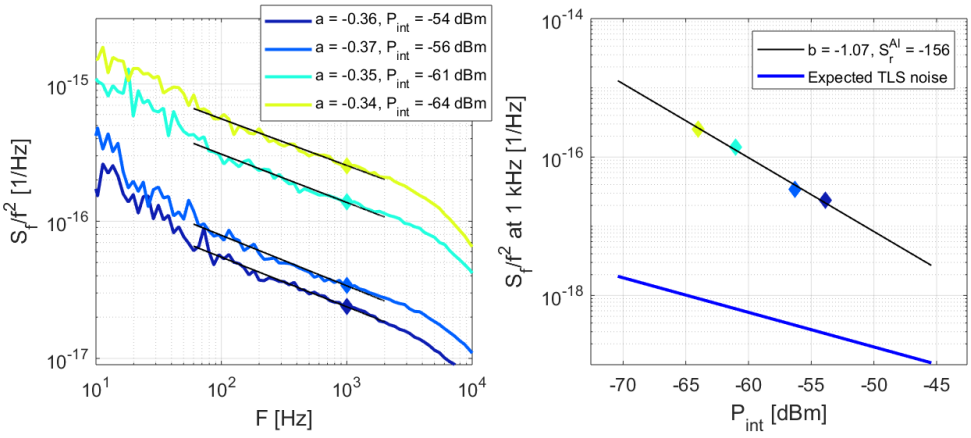

Figure A.4 – Noise spectra of blind Al-NbTiN resonator, KID 8.

A.5 Optical Efficiency

The optical efficiency is obtained from the measured noise spectra and the calculated photon noise contributions, valid for a background limited MKID. The optical efficiency is expected to be dependent on the aluminium line length. Because this is a consequency of the total signal attenuation being length dependent, but which is not accounted for in the $\eta_{\rm opt}$.

$$\eta_{\rm opt} = \frac{NEP^2_{\rm poiss} + NEP^2_{\rm G-R}}{NEP^2_{\rm exp} - NEP^2_{\rm det} - NEP^2_{\rm bunch}} \tag{A.5.1}$$

$$= \frac{2P_{\rm s}h\nu + 4\Delta P_{\rm s}/\eta_{\rm pb}}{NEP^2_{\rm exp}(f = 140{\rm Hz}) - NEP^2_{\rm det}(f = 10^5{\rm Hz}) - 2P_{\rm s}h\nu F_\nu O_\nu} \tag{A.5.2}$$

Fig. A.5 shows the optical efficiency for 6 hybrid MKIDs, graphed as function of the corresponding aluminium line length. To account for the partial radiation absorption in shorter Al sections, $\eta_{\rm opt}$ is rewritten:

$$\eta_{\rm opt}(\ell) = \eta'_{\rm opt}[1 - 10^{0.5a\ell/10}]\,, \tag{A.5.3}$$

with ℓ the Al line length, a the attenuation in dB/mm, the factor $\frac{1}{2}$ because the antenna is positioned halfway the Al CPW and $\eta'_{\rm opt}$ the optical efficiency excluding the radiation absorption by the line. The attenuation of the Al CPW with $S = 0.64$ µm and $W = 1.36$ µm is determined to be $a = -49$ dB/mm, using Sonnet simulation of the signal transmission, as described in 4.2.1. This could as well be readily estimated from Fig. 4.8 and the reported sheet resistance $R_{\rm s} = 0.378\ \Omega/\square$. To illustrate the length dependence further, Fig. **??** shows the absorption efficiency as function of line length, which is given by

$$\eta_{\rm abs} = [1 - 10^{0.5a\ell/10}]\,. \tag{A.5.4}$$

The fitted value for $\eta'_{\rm opt} = 0.46 \pm 0.01$. As expected, this value is slightly higher than the measured $\eta_{\rm opt}$ for the resonators with the shortest Al length.

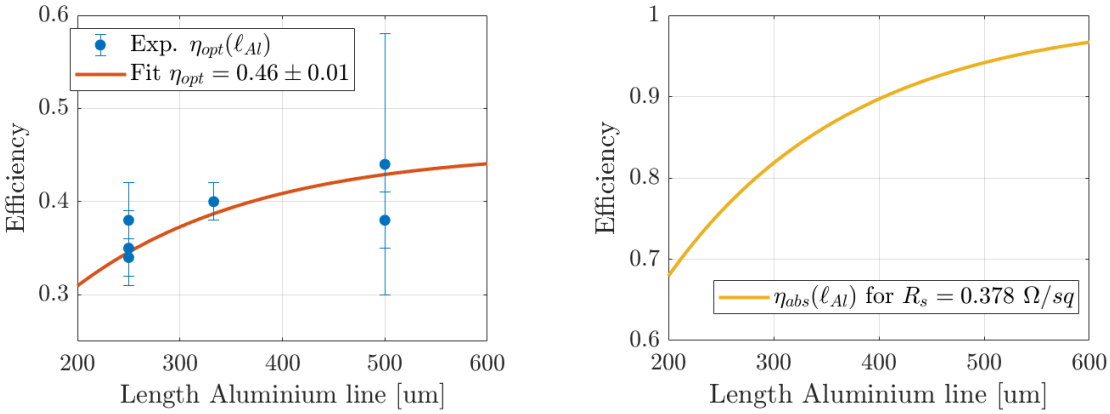

Figure A.5 – Optical efficiency $\eta_{\rm opt}$ and absorption efficiency $\eta_{\rm abs}$ as function of the aluminium line length ℓ. Based on the measurements of KID 1 with $R_{\rm s} = 0.378\ \Omega/\square$, CPW line and gap width $S = 0.64$ µm and $W = 1.36$ µm and 49 dB/mm attenuation. A fit to the data gives $\eta'_{\rm opt} = 0.46 \pm 0.01$.

Bibliography

[1]D. Farrah, K. E. Smith, D. Ardila, C. M. Bradford, M. Dipirro, C. Ferkinhoff, J. Glenn, P. Goldsmith, D. Leisawitz, T. Nikola, N. Rangwala, S. A. Rinehart, J. Staguhn, M. Zemcov, J. Zmuidzinas, J. Bartlett, S. Carey, W. J. Fischer, J. Kamenetzky, J. Kartaltepe, M. Lacy, D. C. Lis, E. Lopez-Rodriguez, M. MacGregor, S. H. Moseley, E. J. Murphy, A. Rhodes, M. Richter, D. Rigopoulou, D. Sanders, R. Sankrit, G. Savini, J.-D. Smith, and S. Stierwalt, "Review: Far-Infrared Instrumentation and Technology Development for the Next Decade", (2017).

[2]D. Scott, P. Barmby, P. Bastien, J. Cami, E. Chapin, J. Di Francesco, M. Fich, M. Halpern, M. Houde, G. Joncas, et al., "The submillimetre universe", arXiv preprint arXiv:1008.4159 (2010).

[3]*ALMA*, `www.almaobservatory.org`, [Online] Accessed: 2019-05-07.

[4]M. Griffin, J. Baselmans, A. Baryshev, S. Doyle, M. Grim, P. Hargrave, T. Klapwijk, J. Martin-Pintado, A. Monfardini, A. Neto, H. Steenbeek, I. Walker, K. Wood, A. D'Addabbo, P. Barry, A. Bideaud, B. Blázquez, J. Bueno, M. Calvo, J.-L. Costa-Kramer, L. Ferrari, A. Gómez-Gutiérrez, J. Goupy, N. Llombart, and S. Yates, "SPACEKIDS: kinetic inductance detectors for space applications", **44**, 991407 (2016).

[5]J. J. A. Baselmans, J. Bueno, S. J. C. Yates, O. Yurduseven, N. Llombart, K. Karatsu, A. M. Baryshev, L. Ferrari, A. Endo, D. J. Thoen, P. J. de Visser, R. M. J. Janssen, V. Murugesan, E. F. C. Driessen, G. Coiffard, J. Martin-Pintado, P. Hargrave, and M. Griffin, "A kilo-pixel imaging system for future space based far-infrared observatories using microwave kinetic inductance detectors", **89**, 1–16 (2016).

[6]P. K. Day, H. G. LeDuc, B. A. Mazin, A. Vayonakis, and J. Zmuidzinas, "A broadband superconducting detector suitable for use in large arrays", Nature **425**, 817 (2003).

[7]J. Baselmans, "Kinetic inductance detectors", Journal of Low Temperature Physics **167**, 292–304 (2012).

[8]P. J. De Visser, J. J. Baselmans, P. Diener, S. J. Yates, A. Endo, and T. M. Klapwijk, "Number fluctuations of sparse quasiparticles in a superconductor", Phys. Rev. Lett. **106**, 1–4 (2011).

[9]P. De Visser, J. Baselmans, S. Yates, P. Diener, A. Endo, and T. Klapwijk, "Microwave-induced excess quasiparticles in superconducting resonators measured through correlated conductivity fluctuations", Applied Physics Letters **100**, 162601 (2012).

[10]D. J. Goldie and S. Withington, "Non-equilibrium superconductivity in quantum-sensing superconducting resonators", Supercond. Sci. Technol. **26** (2012).

[11]J. R. Hook and H. E. Hall, *Solid state physics (the manchester physics series)*, 1991.

[12]J. Bardeen, L. N. Cooper, and J. R. Schrieffer, "Theory of superconductivity", Phys. Rev. **108**, 1175–1204 (1957).

[13]Y. V. Nazarov and J. Danon, *Advanced quantum mechanics: a practical guide* (Cambridge University Press, 2013).

[14]L. N. Cooper, "Bound electron pairs in a degenerate fermi gas", Physical Review **104**, 1189 (1956).

[15]J. Turneaure, J. Halbritter, and H. Schwettman, "The surface impedance of superconductors and normal conductors: the mattis-bardeen theory", Journal of Superconductivity **4**, 341–355 (1991).

[16]B. Mazin, "Microwave kinetic inductance detectors", PhD thesis (California Institute of Technology, Aug. 2004).

[17]F. Jaworski, W. H. Parker, and S. B. Kaplan, "Quasiparticle and phonon lifetimes in superconducting Pb films", Phys. Rev. B **14**, 4209–4212 (1976).

[18]P. J. De Visser, J. J. Baselmans, P. Diener, S. J. Yates, A. Endo, and T. M. Klapwijk, "Number fluctuations of sparse quasiparticles in a superconductor", Phys. Rev. Lett. **106**, 1–4 (2011).

[19]V. M. Angular, "Letters To Nature", October **425**, 12–14 (2003).

[20]E. N. Economou, *The physics of solids: essentials and beyond* (Springer Science & Business Media, 2010).

[21]A. B. Pippard and W. L. Bragg, "An experimental and theoretical study of the relation between magnetic field and current in a superconductor", Proc. R. Soc. Lond. A **216**, 547–568 (1953).

[22]P. D. Visser, *Quasiparticle Dynamics in aluminium superconducting microwave resonators* (2014).

[23]J. Pearl, "Current distribution in superconducting films carrying quantized fluxoids", Applied Physics Letters **5**, 65–66 (1964).

[24]D. M. Pozar, *Microwave engineering* (John Wiley & Sons, 2009).

[25]R. E. Collin, "Foundations for microwave engineering", in, 2nd ed. (John Wiley & Sons, 2001) Chap. Transmission Lines and Waveguides.

[26]H. G. Leduc, B. Bumble, P. K. Day, B. H. Eom, J. Gao, S. Golwala, B. A. Mazin, S. McHugh, A. Merrill, D. C. Moore, O. Noroozian, A. D. Turner, and J. Zmuidzinas, "Titanium nitride films for ultrasensitive microresonator detectors", Appl. Phys. Lett. **97**, 102507–102510 (2010).

[27]R. Barends, *Photon-detecting superconducting resonators* (2009).

[28]T. Guruswamy, D. Goldie, and S. Withington, "Quasiparticle generation efficiency in superconducting thin films", Superconductor Science and Technology **27**, 055012 (2014).

[29]T. Guruswamy, D. J. Goldie, and S. Withington, "Nonequilibrium superconducting thin films with sub-gap and pair-breaking photon illumination", Superconductor Science and Technology **28**, 054002 (2015).

[30]R. W. Boyd, "Photon bunching and the photon-noise-limited performance of infrared detectors", Infrared Phys. **22**, 157–162 (1982).

[31]S. J. Yates, J. J. Baselmans, A. Endo, R. M. Janssen, L. Ferrari, P. Diener, and A. M. Baryshev, "Photon noise limited radiation detection with lens-antenna coupled microwave kinetic inductance detectors", Appl. Phys. Lett. **99** (2011).

[32]J. Gao, "The Physics of Superconducting Microwave Resonators", Thesis **2008**, 197 (2008).

[33]J. Gao, J. Zmuidzinas, B. A. Mazin, H. G. LeDuc, and P. K. Day, "Noise properties of superconducting coplanar waveguide microwave resonators", Applied Physics Letters **90**, 102507 (2007).

[34]J. Gao, M. Daal, A. Vayonakis, S. Kumar, J. Zmuidzinas, B. Sadoulet, B. A. Mazin, P. K. Day, and H. G. Leduc, "Experimental evidence for a surface distribution of two-level systems in superconducting lithographed microwave resonators", Appl. Phys. Lett. **92** (2008).

[35]J. Gao, M. Daal, J. M. Martinis, A. Vayonakis, J. Zmuidzinas, B. Sadoulet, B. A. Mazin, P. K. Day, and H. G. Leduc, "A semiempirical model for two-level system noise in superconducting microresonators", Appl. Phys. Lett. **92**, 1–4 (2008).

[36]J. Baselmans, Private Communication, 2019.

[37]L. Ferrari, O. Yurduseven, N. Llombart, S. J. C. Yates, J. Bueno, D. J. Thoen, A. M. Baryshev, and J. J. A. Baselmans, "Antenna coupled KID performance verification for large format astrophysics arrays", IEEE trans Terahertz Sci. Technol. **8**, 127–139 (2018).

[38]R. M. Janssen, A. Endo, P. J. De Visser, T. M. Klapwijk, and J. J. Baselmans, "Equivalence of optical and electrical noise equivalent power of hybrid NbTiN-Al microwave kinetic inductance detectors", Appl. Phys. Lett. **105** (2014).

[39]R. M. Janssen, J. J. Baselmans, A. Endo, L. Ferrari, S. J. Yates, A. M. Baryshev, and T. M. Klapwijk, "High optical efficiency and photon noise limited sensitivity of microwave kinetic inductance detectors using phase readout", Appl. Phys. Lett. **103** (2013).

[40]P. J. De Visser, J. J. Baselmans, J. Bueno, N. Llombart, and T. M. Klapwijk, "Fluctuations in the electron system of a superconductor exposed to a photon flux", Nat. Commun. **5** (2014).

[41]P. De Visser, D. Goldie, P. Diener, S. Withington, J. Baselmans, and T. Klapwijk, "Evidence of a nonequilibrium distribution of quasiparticles in the microwave response of a superconducting aluminum resonator", Physical review letters **112**, 047004 (2014).

[42]A. Endo, J. J. A. Baselmans, P. P. van der Werf, B. Knoors, S. M. H. Javadzadeh, S. J. C. Yates, D. J. Thoen, L. Ferrari, A. M. Baryshev, Y. J. Y. Lankwarden, P. J. de Visser, R. M. J. Janssen, and T. M. Klapwijk, "Development of DESHIMA: a redshift machine based on a superconducting on-chip filterbank", 84520X (2012).

[43]J. G. Staguhn, "Fir detector sensitivity, dynamic range, and multiplexing requirements for the origins space telescope (ost)", Journal of Low Temperature Physics, 1–8 (2018).

[44]F. Lacy, "Developing a theoretical relationship between electrical resistivity, temperature, and film thickness for conductors", Nanoscale research letters **6**, 636 (2011).

[45]R. Lobo, J. LaVeigne, D. Reitze, D. Tanner, Z. Barber, E. Jacques, P. Bosland, M. Burns, and G. Carr, "Photoinduced time-resolved electrodynamics of superconducting metals and alloys", Physical Review B **72**, 024510 (2005).

[46]S. Yates, J. Baselmans, A. Baryshev, S. Doyle, A. Endo, L. Ferrari, S. Hochgürtel, and B. Klein, "Clean beam patterns with low crosstalk using 850 ghz microwave kinetic inductance detectors", Journal of Low Temperature Physics **176**, 761–766 (2014).

[47]S. J. Yates, A. M. Baryshev, O. Yurduseven, J. Bueno, K. K. Davis, L. Ferrari, W. Jellema, N. Llombart, V. Murugesan, D. J. Thoen, et al., "Surface wave control for large arrays of microwave kinetic inductance detectors", IEEE Transactions on Terahertz Science and Technology **7**, 789–799 (2017).

[48]J. Bueno, V. Murugesan, K. Karatsu, D. Thoen, and J. A. Baselmans, "Ultrasensitive kilo-pixel imaging array of photon noise-limited kinetic inductance detectors over an octave of bandwidth for thz astronomy", Journal of Low Temperature Physics **193**, 96–102 (2018).

[49]K. Karatsu, A. Endo, J. Bueno, P. de Visser, R. Barends, D. Thoen, V. Murugesan, N. Tomita, and J. Baselmans, "Mitigation of cosmic ray effect on microwave kinetic inductance detector arrays", Applied Physics Letters **114**, 032601 (2019).

[50]A. Monfardini, J. Baselmans, A. Benoit, A. Bideaud, O. Bourrion, A. Catalano, M. Calvo, A. D'Addabbo, S. Doyle, J. Goupy, et al., "Lumped element kinetic inductance detectors for space applications", in Millimeter, submillimeter, and far-infrared detectors and instrumentation for astronomy viii, Vol. 9914 (International Society for Optics and Photonics, 2016), 99140N.

[51]J. Baselmans, S. Yates, P. Diener, and P. de Visser, "Ultra low background cryogenic test facility for far-infrared radiation detectors", Journal of Low Temperature Physics **167**, 360–366 (2012).

[52]J. Baselmans, S. J. Yates, R. Barends, Y. J. Lankwarden, J. R. Gao, H. Hoevers, and T. M. Klapwijk, "Noise and sensitivity of aluminum kinetic inductance detectors for sub-mm astronomy", J. Low Temp. Phys. **151**, 524–529 (2008).

Acknowledgements

First of all, I would like to thank Jochem Baselmans for giving me the opportunity to do my master thesis in the Experimental Astronomy group in Delft. Thank you for all the guidance and support, and for your patience during the whole course of this project. You were very encouraging and I learned a great deal from our discussions, your positive feedback and input. Your science enthusiasm and professionalism were a great source of inspiration to me.

Secondly, I would like to thank Juan Bueno for his guidance and helping hand at many points in this project for the realisation, experiments and data analysis of the MKIDs.

Thirdly, I would like to thank Sebastian Hähnle for his support at the beginning of this project. You were always available for questions and patiently provided explanations.

Furthermore, I would like to the rest of the Experimental Astronomy group, I learned a lot in a pleasant and very interesting environment.

The same holds for the Terahertz Sensing Group as a whole, I enjoyed the group dynamics, friendly atmosphere, the numerous presentations and lunch talks, and the best coffee to be found within the faculty.

Finally, I would like to thank my parents for their constant support and advice. Without them, I would not have been be able to study at the TU Delft. Thank you.

Stefan Verheul
Delft, July 2019